INFORMATION TO USERS

This manuscript has been reproduced from the microfilm master. UMI films the text directly from the original or copy submitted. Thus, some thesis and dissertation copies are in typewriter face, while others may be from any type of computer printer.

The quality of this reproduction is dependent upon the quality of the copy submitted. Broken or indistinct print, colored or poor quality illustrations and photographs, print bleedthrough, substandard margins, and improper alignment can adversely affect reproduction.

In the unlikely event that the author did not send UMI a complete manuscript and there are missing pages, these will be noted. Also, if unauthorized copyright material had to be removed, a note will indicate the deletion.

Oversize materials (e.g., maps, drawings, charts) are reproduced by sectioning the original, beginning at the upper left-hand corner and continuing from left to right in equal sections with small overlaps. Each original is also photographed in one exposure and is included in reduced form at the back of the book.

Photographs included in the original manuscript have been reproduced xerographically in this copy. Higher quality 6" x 9" black and white photographic prints are available for any photographs or illustrations appearing in this copy for an additional charge. Contact UMI directly to order.

UMI

A Bell & Howell Information Company
300 North Zeeb Road, Ann Arbor MI 48106-1346 USA
313/761-4700 800/521-0600

Optical Spectroscopy, Crystal Field Analysis, Upconversion and Energy Transfer Studies of Er^{3+} Doped Yttrium Vanadate Single Crystals.

Pierre Kabro

A Thesis
in
The Department
of
Chemistry and Biochemistry

Presented in Partial Fulfillment of the Requirements
for the Degree of Doctor of Philosophy at
Concordia University
Montréal, Québec, Canada

January 1997

0-612-25909-9

ABSTRACT

Optical Spectroscopy, Crystal Field Analysis, Upconversion and Energy Transfer Studies of Er^{3+} Doped Yttrium Vanadate Single Crystals.

Pierre Kabro, Ph.D.
Concordia University, 1997

This thesis presents an extensive spectroscopic investigation of Er^{3+} doped in YVO_4 single crystals. The polarized visible and near infrared absorption and emission spectra are presented. The spectra were analyzed to determine the energy levels of Er^{3+} in YVO_4 and a complete energy level scheme for the $4f^{11}$ ground configuration of Er^{3+} was determined. A total of 59 crystal field levels were observed of the 70 predicted to split out in D_{2d} symmetry. The experimental Stark level energies were used as input data in a parameterized Hamiltonian to calculate the crystal field parameters.

Judd-Ofelt theory was applied to the polarization-averaged room temperature optical-absorption spectra to predict the crystal intensity parameters; Ω_2, Ω_4, and Ω_6, the radiative decay rates and branching ratios for the Er^{3+} transitions from the various excited states to the lower level J-manifolds. Thermalization of the $^2H_{11/2}$ level from the lower lying $^4S_{3/2}$ was studied.

The upconversion of red (652.7 nm) and near infrared (799.1 and 979 nm) radiation into green (due to the $^4S_{3/2} \rightarrow {}^4I_{15/2}$ and the thermally populated $^2H_{11/2} \rightarrow {}^4I_{15/2}$ transitions) and red (due to the $^4F_{9/2} \rightarrow {}^4I_{15/2}$ transition) emission has been studied for Er^{3+} ions in YVO_4 single crystals over a wide temperature range and several dopant concentrations. The upconversion pathways and dynamics for all three excitations were studied. Sequential absorption of photons, energy transfer , and cross-relaxation energy transfer upconversion processes were found to be active and could be identified on the basis of the upconversion transients. An analysis of the upconversion transients shows that energy migration dominates at higher concentrations of Er^{3+} (10%).

An extensive investigation of the fluorescence dynamics of the $^4S_{3/2}$, $^4F_{9/2}$, $^4I_{9/2}$, $^4I_{11/2}$, and $^4I_{13/2}$ states was carried. The decay profiles of the luminescence of the $^4S_{3/2}$ level of Er^{3+} (1.0%) obey the Inokuti-Hirayama model for energy transfer for an electric dipole-electric dipole interaction, in the absence of diffusion among the donors. The dipole-dipole coupling parameter was estimated to be 2.9×10^{-51} m^6s^{-1} and compared well to other well known systems.

ACKNOWLEDGMENTS

This work is the end result of a five year apprenticeship under the guidance of my thesis supervisor, Dr. John. A. Capobianco, and would not have been completed without his insight, patience and advice. I have benefited greatly from his intuition and vast knowledge of the field of solid state lasers, and wish to express my deep appreciation for his support throughout my tenure at Concordia University.

I would like to extend my gratitude to the members of my research committee, Drs. Peter H. Bird and Marcus Lawrence for their contributions to this thesis, and for serving on my thesis committee.

Dr. Marco Bettinelli was extremely kind and generous during my visit at the Università di Verona (Italy). The valuable discussions I had with him were both very enlightening and extremely useful. I would also like to thank Dr. Richard Moncorgé and Mr. Sebastien Ermeneux for their hospitality during a summer visit to the Université de Lyon I (France) where most of the fluorescence dynamics experiments were performed.

I also thank Dr. Clyde Morrison for providing the computer programs necessary to perform the crystal field calculations. I am also greatly indebted to Dr. Enrico Cavalli for growing the single crystals used in this thesis.

I take great pleasure in expressing my appreciation to Dr. Christian Reber for his cooperation and allowing me to use his equipment to perform the absorption spectra. I also thank Dr. Pierre Mathieu for allowing me to use his equipment to perform some of the fluorescence decay measurements.

I wish to thank my colleagues and friends Drs. Pierre-Paul Proulx, Nick Raspa, Guy Cormier, and Ms. Tania Peres. Their companionship and encouragement during the long hours of research were instrumental in keeping my sanity, for which I am very thankful. Drs. Proulx and Raspa were particularly helpful with my introduction to the fascinating world of spectroscopy, while Dr. Cormiers drill questions kept me on my toes and prepared me for many challenging situations during graduate studies.

I would like to thank my parents Najib and Salwa, and my brother Paul for their unfailing support through five (sometimes) long years of graduate school. They have shown remarkable patience and encouragement, and have been a wonderful refuge from the ups and downs of graduate life. Their love, encouragement, and inspiration made it all possible.

Finally, I appreciate the financial support brought by postgraduate scholarships from the Fonds pour la Formation de chercheurs et l'aide a la Recherche (FCAR) and Concordia University.

To my parents; Najib and Salwa

"Scientific discovery is a form of problem solving, and... the processes whereby science is carried on can be explained in the terms that have been used to explain the processes of problem solving"

Simon 1966

TABLE OF CONTENTS

CHAPTER 1

CHAPTER 2

CHAPTER 3

CHAPTER 4

CHAPTER 5

LIST OF FIGURES

LIST OF TABLES

CHAPTER 1

1. INTRODUCTION

1.1 HISTORY OF RARE EARTH SPECTROSCOPY

The rare earths, or lanthanides, are the group of fifteen elements from atomic numbers 57 through 71 in the periodic table. Movement along the group corresponds to the successive filling of the 4f electronic shell from La ($4f^0$) to Lu ($4f^{14}$). The neutral atoms have a ground state electronic configuration of a Xe core ($1s^2 2s^2 2p^6 3s^2 3p^6 3d^{10} 4s^2 4p^6 4d^{10} 5s^2 5p^6$) with two or three outer electrons ($6s^2$ or $5d^1 6s^2$) and a number of 4f electrons varying from 0 to 14. Their most common oxidation state is +3, having lost their 5d and 6s electrons leaving the ions Ce^{3+} through Lu^{3+} with ground state electronic configuration of the form $[Xe]5s^2 5p^6 4f^n$.

The rare earths have found wide technological applications. From Mischmetal used in the manufacture of flints to applications in communications, lasers, solar concentrators and infrared upconverters.

Spectroscopic studies of the rare earth began soon after the introduction of spectrum analysis by Bunsen and Kirchoff in 1859. In 1907 Becquerel and co-workers while investigating the absorption spectra of the minerals, xenotime and tysonite (which contain rare earth ions as impurities) observed that narrow absorption bands at room temperature became narrower at liquid air temperature, 85K [1] . They found that when the samples were cooled to liquid hydrogen, 20K, or liquid helium, 4K, the spectra were composed of lines not bands. The lines were extremely sharp some approaching the sharpness of lines found for atomic gases. The sharpness of the lines permitted detailed investigations of the magneto-optics effects.

These original investigations were hampered due to the lack of theoretical foundation. The interpretation of rare-earth spectra was made possible by the theoretical work of Bethe [2] and Kramer [3]. Bethe developed crystal field theory and Kramer showed that in an odd electron system, every level must remain at least doubly degenerate (Kramers degeneracy). The degeneracy of these levels can be removed by an externally applied magnetic field.

Systematic investigations of rare earth crystalline spectra by Spedding, Freed [4-6] and their collaborators observed that there were groups of lines clustered closely together (hundreds of cm^{-1}) separated by larger intervals (thousands of cm^{-1}). They also observed the disappearance of groups of lines at low temperatures thus recognizing the presence of low lying levels with a significant population at higher temperatures. It was soon recognized that the closely spaced lines arise from the crystal splitting of states of the free atom. From their work, Freed and Spedding proposed energy level schemes; however, they did not identify the parent free ion term, and did not realize that the sharp line spectra were due to intra 4f-configuration transitions. They suggested that the transitions involved were 4f → 5d or 6s. Van Vleck [7] proposed mechanisms by which the intra 4f-configuration transitions can be observed, however, this explanation was not accepted until Broer et al [8] revised Van Vleck's original intensity estimates. Hellwege's [9-11] studies, from 1930 through the 1970's led to a simple method of classifying and identifying the crystal field split-energy levels.

Attempts at calculating ground state crystal field splittings were reasonably successful. Van Vleck made the assumption that the rare-earth ions are basically free ions (with a Russell-Saunders ground state term) in a static electric field produced by the surrounding lattice. He expanded the crystal field potential as a Taylor series using the rare-earth ion as the origin producing a potential expression of the form

$$V = \sum A_{nm} V_{nm} \tag{1.1.1}$$

where A_{nm} are the crystal field parameters and V_{nm} are polynomial potential expressions.

The development of paramagnetic resonance techniques and their use by Elliott and Stevens [12-13] produced more accurate data for ground state crystal splittings, which required more powerful theoretical techniques to interpret the data. The method known as the "Stevens operator equivalents method" was developed, which assumes that the perturbations due to the crystal field are small when compared to spin orbit coupling which allows the ground state to be considered as an isolated multiplet of constant J. The operator equivalent Hamiltonian is most conveniently written in its operator equivalent form as

$$\mathcal{H}_c = \sum_{n}\sum_{m} \theta_j^n \left| B^c_{nm} O^c_{nm} + B^s_{nm} O^s_{nm} \right| \tag{1.1.2}$$

where

$$B^{c,s}_{nm}\langle r\rangle = A^{c,s}_{nm}\langle r\rangle = -|e| K_n \left\langle r^n \right\rangle \gamma^{c,s}_{nm} \tag{1.1.3}$$

are the crystal field parameters; $O_{nm}^{c,s}$ are the operator equivalent expressions, θ_j^n is the operator equivalent factor α_j, β_j, or γ_j ; K_n is the normalizing factor and $\gamma_{nm}^{c,s}$ are lattice sums. The various entries in the secular determinant

$$\langle JM|\mathcal{H}_c|JM'\rangle = \mathcal{H}_{MM'} \qquad (1.1.4)$$

are easily evaluated from published tables. Judd [14] later extended the method to treat the excited states and used optical spectra for the determination of crystal field parameters.

The assumption of Stevens' operator equivalents formalism is that the crystal field interactions act only within the separate free ion J-manifolds (no J-mixing). This assumption is valid when the separations between J-levels are large when compared to the crystal field splittings. However, for the strong crystal fields, and where the free ion levels are mixed, the assumption is no longer valid and J-mixing must be included. Judd [14], Margolis [15], and Axe and Dieke [16] included J-mixing in the calculations. Dieke and his group at Johns Hopkins provided numerous experimental results of rare earth crystal spectra in the 1950's and identified many of the free ion levels in spectra. Their combined theoretical and experimental work relating to rare earth ion spectra is summarized in Figure

1.1.1. The thickness of each level represents the total crystal field splitting in $LaCl_3$. A pendant semicircle indicates that this level fluoresces in the $LaCl_3$ structure.

Hutchings and Ray [17] performed a complete lattice sum calculations of crystal field parameters including contributions from the point charge, induced dipoles and quadrupoles. However, the calculated values for the second and sixth order parameters did not agree with those determined experimentally. Newman and co-workers' superposition model [18-19], considered the inclusion of overlap and exchange interactions. This model predicted the experimental parameters to an accuracy of 10%.

The group at the Harry Diamond Laboratories published a series of reports, entitled, "Rare earth ion-host lattice interactions" where they outline a process that allows the prediction of energy levels using point charge calculations with the dipole contributions included in a self consistent manner [20-22].

In the late sixties and seventies, the prospect of technological applications in communication, television, commercial lighting, and lasers provided an impetus for research in rare earth luminescent materials. This research continues today and studies have covered most of the rare-earth ions in various host matrices (glasses,

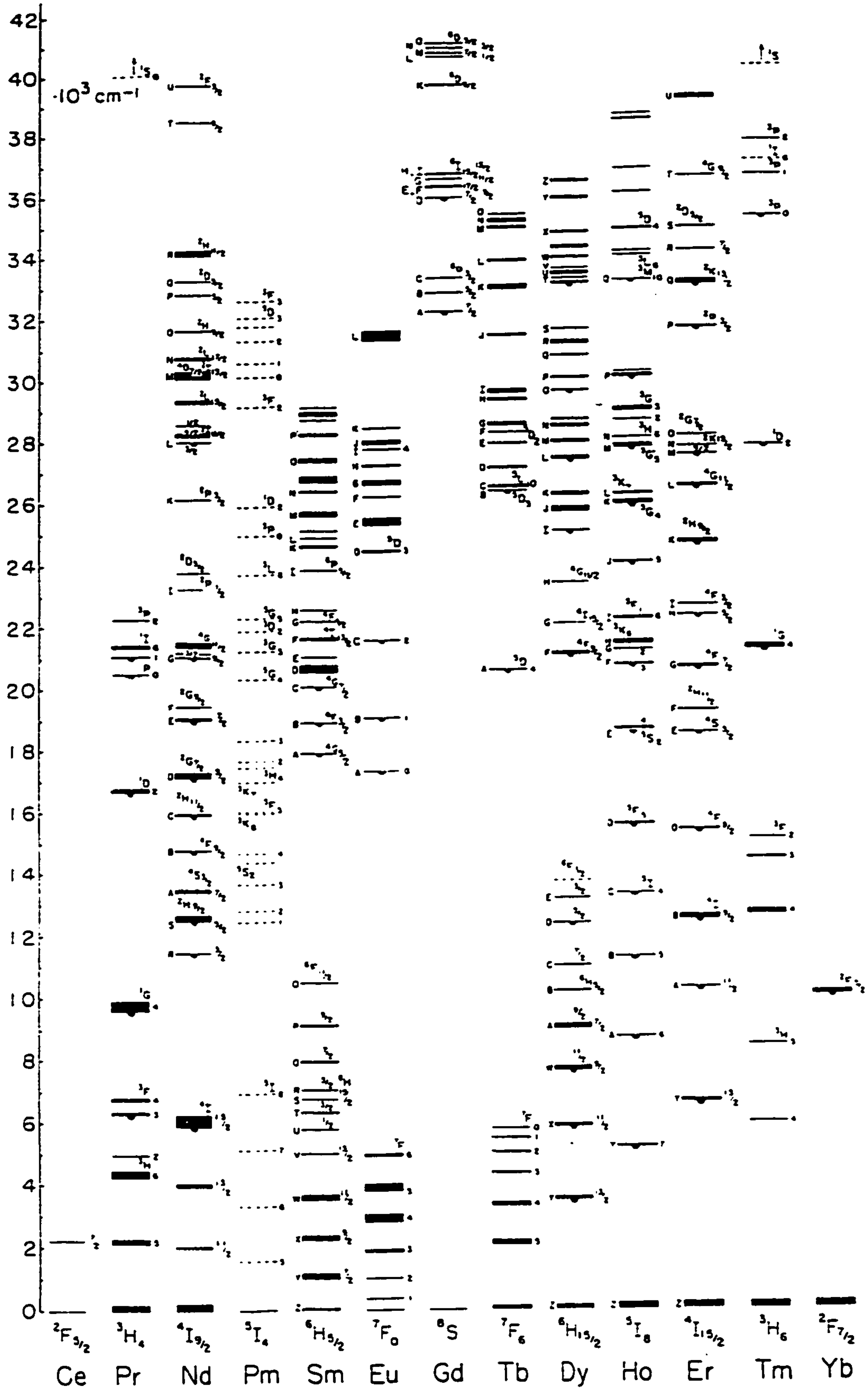

Fig 1.1.1 : Observed energy levels of the rare earth ions.

glass - ceramics, crystals, sol-gels). Comprehensive reviews on rare-earth ions in crystals have been published. Hundreds of host crystals have been studied with hundreds of ion-host combinations. For example, various rare-earth ions in $LiYF_4$, YVO_4, $Y_3Al_5O_{12}$, $Y_3Ga_5O_{15}$, $YAlO_3$, LnP_5O_{14}, $GdAlO_3$, LaF_3, $SrMoO_4$, BaF_2, $CaWO_4$, $LiNbO_3$ etc. have been studied over the years using numerous experimental techniques. Absorption and fluorescence spectroscopy are routinely applied to locate the energy levels. Polarization studies (absorption, emission) have been used to deduce the symmetries of the levels. Electronic Raman and paramagnetic spectroscopy have also been used to locate energy levels. Homogeneous linewidths of transitions have been determined using spectral hole burning, photon echoes, free induction decay and optical nutation. Energy transfer processes have been studied using time resolved spectroscopy, photoacoustic spectroscopy and degenerate four wave mixing.

1.2 ENERGY TRANSFER

Energy transfer is of fundamental importance and plays a major role in many technological applications. In this section we will highlight some of the major contributions which have been made by various groups.

Extensive studies have been made over the last fifty years on the transfer of electronic excitation between ions or molecules in solids. Inherent decay processes were examined, as well as other relaxation processes of the excited donor ions such as i) by direct energy transfer to acceptor ions or ii) the migration of the excitation among donor ions until the eventual transfer to an acceptor occurs. The first is a simple one-step process which involves a resonant energy transfer between a donor (or sensitizer) and an acceptor (or activator). The theory of this process has been developed by Forster [23] and Dexter [24] for multipolar coupling. Later Inokuti and Hirayama [25] developed the theory for the exchange coupling. Relaxation by migration was originally proposed by Botden [26] to account for concentration quenching of the luminescence, and the theory was developed by Dexter and Schulman [27]. This process involves a multistep resonant energy transfers from one donor ion to another in a random-walk manner and finally to a defect which acts as a quenching center.

The combined effects of rapid donor-donor transfers and donor-acceptor transfers have been studied quantitatively. Weber [28] has shown the effects of donor-donor transfer in a $Eu(PO_3)_3$ glass doped with Cr^{3+}. By varying the temperature of the sample, Weber showed that the donor-donor transfer rate and the relative population of the Stark components in the donor excited-state manifold could be changed. Van der Ziel et al [29] performed a similar experiment, where the dopant ion acted as the acceptor. Watts and Richter [30] varied the concentrations of both the donor (Yb^{3+}) and acceptor (Ho^{3+}) ions in YF_3. They observed that at high acceptor concentration energy transfer occurs and attributed this to the nonresonant nature of the donor-acceptor transfer. Krasutsky and Moos [31] investigated the energy-transfer mechanisms operative between the low-lying energy levels of Pr^{3+} and Nd^{3+} in $LaCl_3$. The $^3F_3$ and $^3H_6$ energy levels of the Pr^{3+} ion have several resonant matches with the energy levels of the Nd^{3+} ion facilitating energy transfer. They showed that at low temperatures these transfers are irreversible, hence their effects can be seen as a decrease in the fluorescent intensity and lifetime of the donor excited state, as well as an increase in the excited state population for the ions accepting the energy. They studied the effects of both direct energy transfer and energy migration. Sardar and Powell [32] investigated the characteristics of energy transfer in YVO_4:Nd^{3+} crystals. The authors determined the temperature- and time- dependence of the energy transfer rates for both the host-sensitized and dopant ion interaction processes. They found that the first process had characteristics consistent with the migration and trapping of localized host excitons whereas the latter process was found to be consistent with multistep energy migration via a two-phonon-assisted electric dipole-dipole interaction mechanism.

1.3 UPCONVERSION

Over the past years considerable attention has been paid to the phenomenon of upconversion. Upconversion is a process by which excitation to lower lying levels with low energy radiation (near infrared) results in higher energy emission (visible and near UV radiation) from higher lying electronic levels. This process requires the absorption of at least two photons to provide sufficient energy for the upconverted emission to occur. In Figure 1.3.1a, a sequential two-photon absorption which can lead to upconversion excitation [33] is shown. The first photon populates an intermediate state, then a second photon is used to excite the ions from the intermediate state to the excited-state. An alternative to the two photon process is energy transfer between excited ions which results in an efficient upconversion when a sufficiently large number of ions have been excited to an intermediate state. Two ions in close physical proximity are coupled by a non-radiative process in which one ion returns to the ground state while the other ion is excited to an upper level [34] (Fig 1.3.1b). Generally, these cross relaxation processes are based on electric dipole-dipole interactions. Mismatch in energy between the donor and acceptor ions is effectively bridged by phonons which participate in these energy transfer processes. A third type of efficient upconversion excitation is based on the so-called avalanche absorption (or "photon avalanche" [35]) process that involves excited-state absorption of the

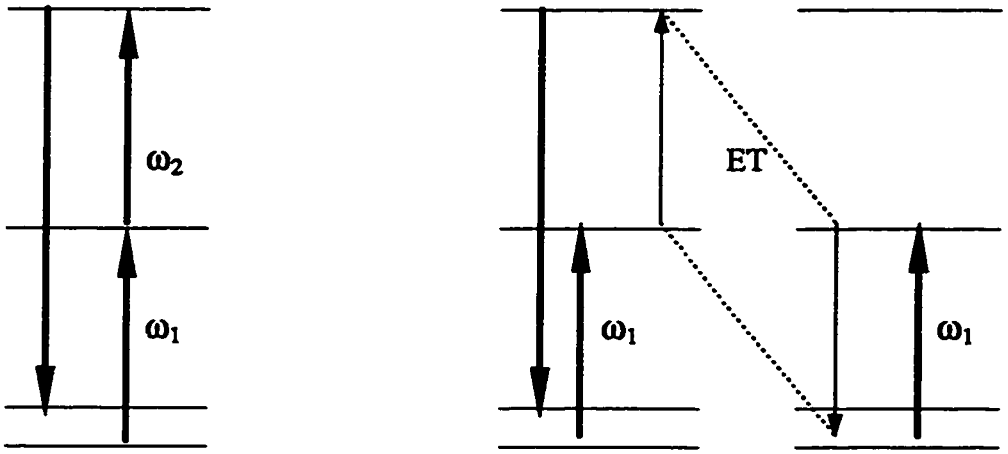

(a) 2-step absorption

(b) cross relaxation upconversion

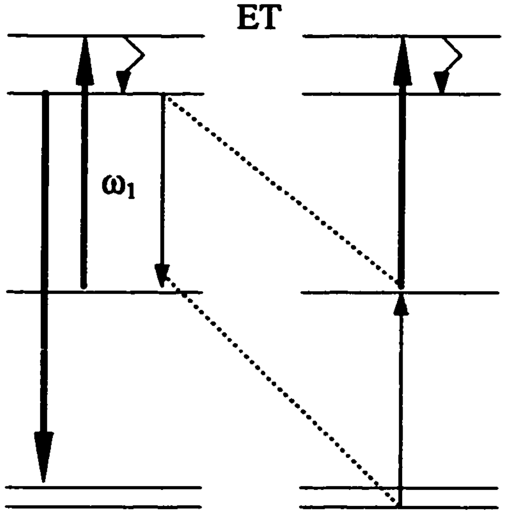

(c) avalanche absorption upconversion

Fig 1.3.1 : Schematic illustration of upconversion excitation mechanisms; a) Two-step absorption, b) Cross relaxation energy transfer, c) Avalanche absorption upconversion.

pump light as well as intrinsic cross-relaxation (Fig 1.3.1c). Initially, nonresonant absorption promotes an ion from the ground state to a metastable state. Absorption of a pump photon by an ion in the metastable state populates the upper level. The upper level can interact with neighbouring ground state ion through ion pair energy transfer to produce two ions in the metastable state. The two ions can then produce four, the four can produce eight, and eventually a substantial population in the metastable state can be established.

Bloembergen [33] pointed out that the infrared conversion process of rare-earth and transition metal ions in crystals is useful for infrared quantum counter, *i.e.* narrow band detector in the infrared region. Auzel [36] investigated the same phenomenon for Er^{3+} and Tm^{3+} ions in tungstates which are efficiently sensitized by Yb^{3+} ions, as a result of successive two or three energy transfers. Hewes and Sarver [37] studied upconversion of the same rare earth ions in LaF_3 and other fluorides. The authors observed that the green emission from the Er^{3+} ions following infrared excitation was produced by energy transfer from Yb^{3+} to the Er^{3+} ions. They also suggested that three successive energy transfer steps are responsible for the upconversion observed for Tm^{3+} ions.

Estimates of the probabilities of successive energy transfer and cooperative energy transfers have been made possible using the model developed by Miyakawa and Dexter [38] . The authors showed that the probability of successive transfers is normally greater than that of cooperative transfers. Cooperative transfers have been observed for systems co-doped with Tb^{3+} and Yb^{3+} ions [39]. In this case Yb^{3+} has an infrared absorption band at about 1μm and no other absorption in the energy region of interest, and Tb^{3+} does not absorb in this energy region; however, Tb^{3+} emits light of approximately twice the energy of the exciting photons if and only if the Yb^{3+} is present.

Stimulated emission by upconversion pumping was first reported by Johnson and Guggenheim [40] using infrared light from flashlamps to excite Yb^{3+} ions in BaY_2F_8 co-doped with Er^{3+} or Ho^{3+}. The first upconversion continuous wave laser [41] was reported in 1986. This laser used infrared dye-laser excitation to produce green laser emission at 550 nm of the $^4S_{3/2} \rightarrow {}^4I_{15/2}$ transition in $YAlO_3$:Er^{3+}. Photon avalanche mechanisms have been found to dominate the pump mechanism for the visible upconversion of the Pr^{3+}:$LaCl_3$ laser [42]. Shortly, thereafter, photon avalanche pumping was reported for Nd^{3+}:$YLiF_4$ [43] and Tm^{3+}:$YLiF_4$ [44].

1.4 STATEMENT OF THE PROBLEM

The rare earth elements, except La, form an isostructural series of compounds with the vanadate ion of the form, RVO_4, in which the rare earth ion is coordinated by eight oxygen atoms. The interest in and importance of these compounds derives from several properties, especially their interesting and useful optical properties [45-48].

The closely related orthophosphate series has been proposed as a crystalline nuclear-waste form for the storage of radioactive products from nuclearreactor processes. The cathodoluminescent behavior of Eu^{3+}-doped YVO_4 and its subsequent use as a color-television phosphor [49] has aroused considerable interest in the study of rare-earth compounds with Zircon-structure (i.e. $ZrSiO_4$ type) and the rare-earth ions doped in isostructural host lattices. YVO_4 is an important material for applications in various types of optical systems. It is useful as an infrared polarizer, and a host for rare-earth lasers. In fact, $YVO_4:Nd^{3+}$ laser crystals have been found to have some performance characteristics superior to those of standard $Y_3Al_5O_{12} : Nd^{3+}$ lasers [50-55]. Consequently, it is interesting to investigate the detailed behavior of such host lattice and host-sensitized energy transfer doped with Er^{3+} ions.

Motivation to understand and enhance upconversion processes has recently increased because of the availability of high-powered, near infrared diode lasers. A solid state blue-green laser pumped by diode lasers is desirable for applications such as underwater communication and optical-disk storage devices. One approach to this problem is to use a "two-color" sequential absorption process [56], while upconversion by energy transfer between excited neighbouring ions is an alternative approach which often uses a single near infrared pump source.

Erbium is an ideal ion as it emits in the visible, and absorbs in the near infrared around 800 and 980 nm, both excellent diode-laser wavelengths. Er^{3+} also lases at 1.55 μm between the first excited $^4I_{13/2}$ and ground $^4I_{15/2}$ states and upconverts, in suitable host lattices, to shorter wavelengths. Er^{3+} in different hosts also lases at different wavelengths in several three- and four- laser schemes. Low temperature green ($^4S_{3/2} \rightarrow {^4I_{15/2}}$) upconversion laser action was also achieved in small, monolithic Er^{3+}:$YLiF_4$ rods [57]. Less efficient laser action on other transitions in this material [58-60] and diode-pumping experiments [61] suggest the possibility of a multicolor solid state laser.

1.5 REFERENCES

1. J. Becquerel, Radium, 4, 328 (1907).
2. H.A. Bethe, Ann. Phys., 3, 133 (1929).
3. M.H.A. Kramers, Proc. Acad. Sci. Amsterdam, 32, 1176 (1929).
4. S. Freed, F.H. Spedding, Nature, 123, 525 (1929).
5. S. Freed, Phys. Rev., 38, 2122 (1931).
6. F.H. Spedding, H.F. Hamlin, J. Chem. Phys., 5, 429 (1937).
7. J.H. Van Vleck, J. Phys. Chem., 41, 67 (1937).
8. L.J.F. Broer, C. J. Gorter, J. Hoogschagen, Physica, 11, 231 (1945).
9. K.H. Hellwege, Ann. Phys., 4, 95, 127, 136, 143, 156, 357 (1948).
10. A.M. Hellwege, K.H. Hellwege, Z. Phys., 130, 549 (1951).
11. K.H. Hellwege, H.G. Kahle, Z. Phys., 129, 62, 85 (1951).
12. R.J. Elliott, K.W.H. Stevens, Proc. Roy. Soc. (London) A, 215, 437 (1952).
13. R.J. Elliott, K.W.H. Stevens, Proc. Roy. Soc. (London) A, 219, 387 (1953).
14. B.R. Judd, Mol. Phys., 2, 407 (1959).
15. J.S. Margolis, J. Chem. Phys., 35, 1367 (1961).
16. J.D. Axe, G.H. Dieke, J. Chem. Phys., 37, 2364 (1962).
17. R.T. Hutchings, D.K. Ray, Proc. Phys. Soc. (London), 81, 663 (1963).
18. M.M. Ellis, D.J. Newman, J. Chem. Phys., 47, 1986 (1967).

19. S.S. Bishtan, M. M. Ellis, D.J. Newman, J. Smith, J. Chem. Phys., 47, 4133 (1967).

20. N. Karayianis, C.A. Morrison, Harry Diamond Laboratories Report, HDL-TR-1648 NTIS AD-A776-330 (1973).

21. N. Karayianis, C.A. Morrison, Harry Diamond Laboratories Report, HDL-TR-1682 NTIS AD-A011-252 (1975).

22. R.P. Leavitt, C.A. Morrisson, D.E. Wortman, Harry Diamond Laboratories Report, HDL-TR-1673 NTIS AD-A017-849 (1975).

23. Th. Förster, Ann. Phys., 2, 55 (1948).

24. D. L. Dexter, J. Chem. Phys., 21, 836 (1953).

25. M. Inokuti, F. Hirayama, J. Chem. Phys., 43, 1978 (1965).

26. Th. P. J. Botden, Philips Res. Rep., 7, 197 (1952).

27. D. L. Dexter, J. H. Schulman, J. Chem. Phys., 22, 1063 (1954).

28. M. J. Weber, Phys. Rev. B, 4, 2932 (1971).

29. J. P. Van der Ziel, L. Kopf, L. G. Van Uitert, Phys. Rev. B, 6, 615 (1972).

30. R. K. Watts, H. J. Richter, Phys. Rev. B, 6, 1584 (1972).

31. N. Krasutsky, H. W. Moos, Phys. Rev. B, 8, 1010 (1973).

32. D. Sardar, R. C. Powell, J. Appl. Phys., 51 (5), 2829 (1980).

33. N. Bloombergen, Phys. Rev. Lett., 2, 84 (1959).

34. F. Auzel, C. R. Acad. Sci. (Paris), 262, 1016 (1966).

35. J. S. Chivian, W.E. Case, D.D. Eden, Appl. Phys. Lett., 35, 124 (1979).

36. F. Auzel, Compt. Rend., 262 B, 1016 (1966); 263B, 819 (1966).

37. R. A. Hewes, J. F. Sarver, Phys. Rev., 182, 427 (1969).

38. T. Miyakawa, D. L. Dexter, Phys. Rev. B, 1, 70 (1970).

39. T. Miyakawa, D. L. Dexter, Phys. Rev. B, 1, 2961 (1970).

40. L. F. Johnson, H. J. Guggenheim, Appl. Phys. Lett., 19, 44 (1971).

41. A. J. Silversmith, W. Lenth, R. M. Macfarlane, J. Opt. Soc. Am., A3, 128 (1986).

42. M. E. Koch, A. W. Kueny, W. E. Case, Appl. Phys. Lett., 56, 1083 (1990).

43. W. Lenth, R. M. Macfarlane, J. Lumin., 45, 346 (1990).

44. R. M. Macfarlane, R. Wannmacher, T. Hebert, W. Lenth, Tech. Dig. Conf. Lasers Electro-Opt. (CLEO '90), Anaheim, CA, p.250, Paper CWF-1 (1990).

45. P.P. Yaney, L.G. DeShazer, J. Opt. Soc. Am., 66, 1405 (1976).

46. V.R. Pekurovskii, Sov. Phys. Solid State, 29 (5), 787 (1987).

47. V. Puri, S.P. Puri, Phys. Rev. B, 9 (11), 4673 (1974).

48. J.P. Briffaut, J. Phys. (France), 29, 515 (1968).

49. A.K. Leviene, F.C. Palilla, Appl. Phys. Lett., 6, 118 (1964).

50. A.W. Tucker, M. Brinbaum, C.L. Fincher, J.W. Erler, J. Appl. Phys., 48, 4907 (1977).

51. A.W. Tucker, M. Brinbaum, C.L. Fincher, J.W. Erler, J. Appl. Phys., 52, 3067 (1981).

52. J.R. O'Connor, Appl. Phys. Lett., 9, 407 (1966).

53. R.A. Fields, M. Birnbaum, C.L. Fincher, Appl. Phys. Lett., 51, 1885 (1987).

54. T. Sasaki, T. Tojima, A. Yokotani, O. Oguri, S. Nakai, Opt. Lett., 16, 1665 (1991).

55. T. Taira, A. Mukai, Y. Nozawa, T. Kobayashi, Opt. Lett., 16, 1955 (1991).

56. D.C. Nguyen, G.E. Faulkner, M. Dulick, Appl. Opt., 28, 3553 (1989).

57. W. Lenth, A.J. Silversmith, R.M. MacFarlane, in Advances in Laser Science- III, Proceedings of the Third International Laser Science Conference, Atlantic city, NJ, November 1-4 (1987), edited by A.C. Tan, J.L. Cole, W.C. Stwalley, AIP Conf. No. 172, 8 (AIP, NY, 1988).

58. R.A. McFarlane, Appl. Phys. Lett., 54, 2301 (1989).

59. R.A. McFarlane, M. Robinson, S.A. Pollack, Proc. Soc. Photo-Opt. Instrum. Eng., 1223, 294 (1990).

60. T. Hebert, R. Wannemecher, W. Lenth, R.M. McFarlane, Appl. Phys. Lett., 57, 1727 (1990).

61. F. Tong, W.P. Risk, R.M. McFarlane, W. Lenth, Electron. Lett., 25, 1391 (1989).

CHAPTER 2

2. THEORY

This chapter is intended to provide the reader with the theoretical aspects pertinent to this thesis so that it can be read without continual reference to texts on the subject [1-3].

2.1 BACKGROUND AND CRYSTAL FIELD HYPOTHESIS

The ground-state electronic configuration of the trivalent rare-earths is $[Xe]5s^2 5p^6 4f^N$, where N may take on the values 1 to 14. The optically active 4f electrons are shielded from external fields by the outer, 5s and 5p shells whose radial extension is several times that of the 4f. Thus, the surrounding ligands will only weakly perturb the 4f electrons. Because of this and the fact that the crystal environment constitutes only a small perturbation of the atomic energy levels, the optical spectra of rare earths doped in solid state materials will be composed of a series of sharp lines closely resembling the free-ion spectra.

In an ionic crystal the electrons occupy orbitals that are highly localized about the ions. The effect of this localization is that any electron can be considered to be associated with a particular ion. However, each electron will feel the influence of the electrons belonging to the other ions and of the nuclei belonging to the other ions. This influence may be taken into account by considering that the electrons of the individual ions are subjected to the action of a crystalline field. The crystalline field approximation is valid in a magnetically dilute substance in which the magnetic ions are far apart.

The crystal field is considered to be external to the ion and possessing a definite symmetry. Therefore, by knowing the symmetry and making use of group theory it is possible to predict the splitting of the energy levels and the eigenfunctions representing the states. The evaluation of the crystal field splitting is performed by starting with the unperturbed eigenfunctions. We have at our disposal three schemes: the weak field, the medium field and the strong field. The three fields are an indication of the strength of the crystal field in comparison to the electrostatic interaction between electrons. The rare earth ions in crystals present spectra which are very similar to the free ion spectra, due to the shielding by the outer 5s and 5p shells, therefore the weak field approximation best describes the strength of the crystal field. Here the crystal field splitting is small in comparison with the spin orbit interaction. The result being that the crystal field splitting is small in comparison to the splitting between multiplets.

2.2 THE HAMILTONIAN OF THE FREE ION

The Hamiltonian of the free ion is given by :

$$\mathcal{H} = \mathcal{H}_o + \mathcal{H}_{so} \tag{2.2.1}$$

where

$$\mathcal{H}_o = \frac{-\hbar^2}{2m} \sum_{i=1}^{N} \nabla_i - \sum_{i=1}^{N} \frac{Z^* e^2}{r_i} + \sum_{i<j}^{N} \frac{e^2}{r_{ij}} \tag{2.2.2}$$

and $\mathcal{H}_{so}$ is the spin orbit interaction given by

$$\mathcal{H}_{so} = \sum_{i=1}^{N} \xi(r_i).s_i l_i \tag{2.2.3}$$

In the above equations N is the number of 4f electrons, m is the mass of the electron, $\hbar^2\nabla_i$ is the square of the momentum operator for the i^{th} electron, r_i is the distance from the nucleus to the i^{th} electron, r_{ij} the distance between the i^{th} and j^{th} electrons, s_i and l_i the spin and orbital angular momentum respectively of the i^{th} electron. Z^*e is the screened charge of the nucleus, and $\xi(r_i)$ the spin-orbit coupling function which is

$$\xi(r_i) = \frac{\hbar^2}{2\,m^2c^2r_i}.\frac{dU(r_i)}{dr_i} \tag{2.2.4}$$

where $U(r_i)$ is the potential in which the electron i is moving. The interaction was derived from relativity theory in the Bohr orbit quantum mechanics, but it is also a natural consequence of a nonrelativistic approximation to the Dirac equation.

The kinetic energy of the 4f electrons is given by the first term in the Hamiltonian (Eq. 2.2.2 and 2.2.3), the second term represents the Coulomb interaction with the nucleus. The real charge of the nucleus is replaced by a screened charge, due to the interaction with the closed shells that modifies only the magnitude of the term and not its symmetry. The degeneracies within the configuration of the 4f electrons are not removed by the spherically symmetric terms, the first two terms of equation 2.2.2, and hence are neglected in this discussion.

Consequently, we will consider only the last two terms, $\sum_{i<j}^{N} \frac{e^2}{r_{ij}}$ which represents the mutual Coulomb interaction of the 4f electrons (H_c), and $\sum_{i=1}^{N} \xi(r_i).s_i l_i$ the spin-orbit interaction ($\mathcal{H}_{so}$). These two interactions are responsible for the energy level structure of the 4f electrons.

2.2.1 Coulomb Interaction

The largest contribution to the Hamiltonian for the free ion is the electrostatic interaction of the nl^N electrons. The matrix elements of this interaction are written in terms of the Slater parameters $F^{(k)}$. The $F^{(k)}$ are radial expectation values given by

$$F^{(k)} = e^2 \int_0^\infty \int_0^\infty \frac{r_<^k}{r_>^{k+1}} \left[R_{nl}(r_i) R_{nl}(r_j) \right]^2 r_i^2 dr_i \, r_j^2 \, dr_j \qquad (2.2.1.1)$$

where

$$\int_0^\infty R_{nl}^2(r)\, r^2\, dr = 1 \qquad (2.2.1.2)$$

$$\frac{r_<}{r_>} = \frac{r_i}{r_j} \text{ if } r_i < r_j \quad \text{and} \quad \frac{r_j}{r_i} \text{ if } r_i > r_j$$

Generally for the d^N electrons the matrix elements of the Coulomb interaction are given in terms of $F^{(k)}$ while the same interaction for the f^N series is given in terms of new parameters $E^{(k)}$ the Racah parameter (Nielson and Koster) [4]. Neilson and Koster give for the matrix elements of the Coulomb interaction

$$< \alpha' L' S' \,|\mathcal{H}_c|\, \alpha L S > = \delta_{LL'} \delta_{SS'} \sum_k g_k (\alpha',\alpha, L, S) E^K \qquad (2.2.1.3)$$

and the coefficients $g_k (\alpha',\alpha, L, S)$ are given for each of the states of f^N. The relation of $E^{(K)}$ to $F^{(K)}$ is given in a number of works (for example Judd, 1963 [5]).

2.2.2 The Spin Orbit Interaction

As we have stated previously the second interaction of reasonable magnitude in the free ion is the spin orbit coupling given in equation 2.2.3. In the rare earth series the spin orbit interaction is quite strong. Consequently, it is convenient to perform the calculation in a set of basis functions in which the Coulomb and spin orbit Hamiltonian are diagonal. The set of functions that achieves this is the total angular momentum function $|JM_J>$. The total angular momentum operator is given by

$$\vec{J} = \vec{L} + \vec{S} \qquad (2.2.2.1)$$

Since both the spin orbit and the Coulomb interaction commute with the total angular momentum, the wavefunctions may be characterized by the eigenvalues of $\vec{J}^2$ and J_Z. That is, we may write Ψ_{JM} or $|JM>$ for the wavefunctions with

$$\vec{J}^2 \, |JM> = J(J+1) \, |JM> \qquad (2.2.2.2)$$

and

$$J_Z \, |JM> = M \, |JM> \qquad (2.2.2.3)$$

The values of J are restricted to

$$|L - S| \leq J \leq |L + S| \tag{2.2.2.4}$$

Therefore matrix elements may be obtained by using the following

$$< J', M', L', S' | \mathcal{H}_c + \mathcal{H}_{so} | J, M, L, S, > = \delta_{JJ'} \delta_{MM'} \tag{2.2.2.5}$$

2.2.3 Coulomb and Spin Orbit Energies

In section 2.2.1 we showed that the matrix elements for Coulomb interactions may be written in terms of the Slater parameters $F^{(k)}$ (or F_k). The relationship between $F^{(k)}$ and F_k is used in order to avoid large denominators. Racah introduced a more convenient parameter E_k [1] which may be written as

$$E = \sum_{k=0}^{3} e_k E^k \tag{2.2.3.1}$$

with E^k expressed in terms of F_k.

The matrix elements of the spin orbit interaction may also be evaluated using tensor formalism. The matrix elements of the spin orbit coupling are responsible for the mixing of the states with the same J but different L and S. The diagonal matrix elements are obtained using the following formula

$$(f^n\ldots\ldots \mid H_{so} \mid f^n\ldots\ldots) = \xi\,(\lambda/2)\,[\,J(J+1) - L(L+1) - S(S+1)] \qquad (2.2.3.2)$$

where λ is a constant for a state with given L and S.

2.3 CRYSTAL FIELD THEORY

The principal objective of crystal field theory is to determine the modifications to the energy levels and wavefunctions of the free ions due to the presence of a crystal field. The ion is treated as an isolated one placed in an electrostatic field of the proper symmetry and intensity. In the simplest model of the crystal field, the point charge model introduced by Bethe [6], the lattice is replaced by an array of point charges at the nuclei of the constituent ions. A multipole expansion is made of the point charge potential energy at the rare earth site (in this thesis).

Crystal field theory was originally applied in isolated cases by Van Vleck [7] and Abragam [8] for the calculation of magnetic properties of transition ions and fields of cubic symmetry. Later Elliott and Stevens [9,10] developed methods to study the influence of the crystal field in more general cases. They introduced the operator equivalent [9] which simplified the problem of handling the perturbation calculation.

In the following we will give a brief description of the interaction of the 4f electrons with the crystal field. The one electron crystal field energy may be written as:

$$\mathcal{H}_{CF}(r) = \frac{1}{4\pi\varepsilon_0} \sum_{l} \sum_{k=0}^{\infty} \sum_{q=-k}^{k} \frac{Z_l e^2}{a_l^{k+1}} r^k Y_k^q(\theta_l, \phi_l)\, C_q^{(k)}(\theta, \phi) \qquad (2.3.1)$$

where the summation l is over the neighbouring point charges, $C_q^{(k)}$ is given by

$$C_q^{(k)}(\theta, \phi) = \sqrt{\frac{4\pi}{2k+1}}\, Y_k^q(\theta, \phi) \qquad (2.3.2)$$

and $Y_k^q(\theta, \phi)$ is the spherical harmonic. Thus, to calculate the energy levels in the presence of the crystal field, the matrix elements of $\mathcal{H}_{CF}(r)$ between various 4f-electron wavefunctions must be evaluated. The value of $\langle r^k \rangle$, the expectation value will be a common factor therefore if we confine our attention to the angular properties of the crystal field we have :

$$\mathcal{H}_{CF}(\theta, \phi) = \frac{1}{4\pi\varepsilon_0} \sum_{l} \sum_{k,q}^{\infty} \frac{Z_l e^2}{a_l^{k+1}} Y_k^q(\theta, \phi)\, C_q^{(k)}(\theta, \phi) \qquad (2.3.3)$$

when the sum over l is made, the crystal field Hamiltonian may be written as:

$$\mathcal{H}_{CF} = \sum_{k,q} B_q^k C_q^{(k)}(\theta, \phi) \qquad (2.3.4)$$

where B^k_q is the crystal field parameter and contains all the radial information. The crystal field parameter B^k_q may also be written as B_{kq} and is equivalent to

$$B_{kq} = -e \int (-1)^q \rho(R) C_{k-q} \frac{r^k_<}{r^{k+1}_>} d\tau = A_{kq} < r^k > \tag{2.3.5}$$

where A_{kq} is the spatial integral of the charge distribution and is equal to:

$$A_{kq} = -e \int \frac{\rho(r)}{r^{k+1}} (-1)^q C_{kq} d\tau \tag{2.3.6}$$

Knowing the structure of the compound under investigation it is possible to calculate the crystal field components, A_{kq}. Using the three parameter theory of crystal fields proposed by Leavitt et al [11] the crystal field parameters B_{kq} can be related to the crystal field component by

$$B_{kq} = \rho_k A_{kq} \tag{2.3.7}$$

The ρ_k are ion dependent host independent quantities given by the expression

$$\rho_k = \langle r^k \rangle_{HF} \, (1-\sigma_k) \, \tau^k \qquad (2.3.8)$$

where the $\langle r^k \rangle_{HF}$ parameters are the Hartree-Fock radial expectation values and σ_k are linear shielding factors (Sternheimer shielding factors) [12]. The τ parameter is a scaling parameter introduced to account for the inadequacy of the bare Hartree-Fock wavefunctions and the expansion of the free ion wavefunction [13]. The values of ρ_k [13] reported for Er^{3+} are found in table 2.3.1.

Table 2.3.1 : Radial factors ρ_k with k=2,4, and 6 in $Å^k$ to convert lattice sums A_{kq} to crystal field parameters B_{kq}.

ρ_k ($Å^k$)	
ρ_2	0.1706
ρ_4	0.4053
ρ_6	0.9649

The number of B_{kq} parameters which are required is determined by the symmetry of the crystal field. In Table 2.3.2 we show the relationship which exists between the point symmetry and the non-vanishing B_{kq} parameters. Table 2.3.3 shows the term splitting for integral J and half integral J. Further, in the case of 4f-electron wavefunction we need only consider values with $k \leq 6$ and odd k values (due to the odd parity components of the crystal field) will not contribute to the matrix elements between 4f electron wavefunctions and are omitted in the crystal field Hamiltonian. The odd crystal field parameters are used to calculate the intensity of the transition.

Using the crystal field parameters, B_{kq}, it is possible to calculate the crystal field strength. The crystal field strength is a quantitative measure of the interaction between the rare earth and the surrounding lattice and it is calculated using the following equation [14]

$$S_{CF} = \frac{1}{3}\sum_{k}\frac{1}{2k+1}\left[B_{k0}^{2} + 2\sum_{q>0}\left(\mathrm{Re}\,B_{kq}^{2} + \mathrm{Im}\,B_{kq}^{2}\right)\right]^{1/2} \qquad (2.3.9)$$

where the sum over k covers the values 2,4, and 6.

Table 2.3.2 : Independent nonvanishing B_{kq} for the 32 point groups.

Point Group	Nonvanishing B_{kq}
C_1, C_i	All B_{kq} values (B_{21} real)
C_2 C_s C_{2h}	B_{20}, RB_{22}, B_{40}, B_{42}, B_{60}, B_{62}, B_{64}, B_{66}
D_2 C_{2v} D_{2h}	B_{20}, RB_{22}, B_{40}, B_{42}, RB_{44}, B_{60}, RB_{62}, RB_{64}, RB_{66}
C_4 S_4 C_{4h}	B_{20}, B_{40}, RB_{44}, B_{60}, B_{64}
D_4, C_{4v} D_{2d}, D_{4h}	B_{20}, B_{40}, RB_{44}, B_{60}, B_{64}
C_3, S_6	B_{20}, B_{40}, RB_{43}, B_{60}, B_{63}, B_{66}
D_3 C_{3v} D_{3d}	B_{20}, B_{40}, RB_{43}, B_{60}, RB_{63}, RB_{66}
C_6, C_{3h} C_{6h}, D_6 C_{6v}, D_{3h} D_{6h}	B_{20}, B_{40}, B_{60}, RB_{66}
T, T_d, T_h O, O_h	B_{40}, RB_{44}, B_{60}, RB_{64}

Table 2.3.3 : Term splitting for integral J, and half-integral J.

	J								
	0	1	2	3	4	5	6	7	8
Cubic[a]	1	1	2	3	4	4	6	6	7
Hexagonal[b]	1	2	3	5	6	7	9	10	11
Tetragonal[c]	1	2	4	5	7	8	10	11	13
Lower symmetry[d]	1	3	5	7	9	11	13	15	17

a) O_h, O, T_d, T_h, T.

b) D_{6h}, D_6, C_{6v}, C_{6h}, C_6, D_{3h}, D_{3d}, D_3, C_{3v}, S_6, C_3

c) D_{4h}, D_4, C_{4v}, C_{4h}, C_4, D_{2d}, S_4

d) D_{2h}, D_2, C_{2v}, C_{2h}, C_2, C_s, S_2, C_1

	1/2	3/2	5/2	7/2	9/2	11/2	13/2	15/2	17/2
Cubic	1	1	2	3	3	4	5	5	6
All other groups	1	2	3	4	5	6	7	8	9

2.4 SELECTION RULES

The perturbation responsible for optical transitions in a trivalent rare earth ion is the interaction between the electrons in the 4f shell and the electromagnetic field. Two radiative processes are possible when the electrons interact with the electromagnetic field, absorption and emission. The interaction Hamiltonian between the electron(s) in the system and the radiation field contains two terms one responsible for the electric dipole interaction and the other for the magnetic dipole interaction.

The electric dipole operator is given by $\sum_i er_i$. The components $\sum ex_i$, $\sum ey_i$ and $\sum ez_i$ transform like translations. Linear combinations of these components may be obtained which form an irreducible tensor operator of the first order:

$$r_1 = -\sum_i \frac{x_i + iy_i}{\sqrt{2}} \tag{2.4.1}$$

$$r_0 = \sum_i z_i \tag{2.4.2}$$

$$r_{-1} = \sum_i \frac{x_i - iy_i}{\sqrt{2}} \tag{2.4.3}$$

These new components transform like basis function for the representation D_{1u} of the three dimensional rotation group.

The transitions depend on the matrix elements $\left\langle \psi_f^{el} \middle| r_\alpha \middle| \psi_i^{el} \right\rangle$. The products $r_\alpha \, \psi_i^{el}$ transform according to

$$D_1 \times D_J = D_{J_c+1} + D_J + D_{J_i-1} \tag{2.4.4}$$

if $J_i \geq 1$. If $J = 0$ we have $D_1 \times D_0 = D_1$ and then only $J_f = 1$ is allowed eliminating the transitions $J_f = 0 \rightarrow J_i = 0$.

Since the electric dipole is an odd operator, the parity of the final state must be different from the parity of the initial state. This is Laporte's Rule. Therefore we obtain the following results

$$\Delta J = 0, \pm 1, \qquad J_i = 0 \not\rightarrow J_f = 0$$

$P_f \neq P_i$ (parity)

In the Russell-Saunders approximation, the eigenfunctions transform like the representation $D_L \times D_S$. The dipole operator components transform like D_1 (L=1, S=0) thus we have

$$\Delta L = 0 \pm 1, \qquad L_i = 0 \nrightarrow L_f = 0$$

$$\Delta S = 0$$

$$P_f \neq P_i$$

The magnetic dipole operator is given by

$$\mu = - \frac{\ell}{2mc} (L + 2S) \tag{2.4.5}$$

Irreducible tensor operator of the first order may be formed of the type

$$\mu_1 = \frac{\ell}{2mc} \frac{(L_x + 2S_x) + i(L_y + 2S_y)}{\sqrt{2}} \tag{2.4.6}$$

$$\mu_0 = - \frac{\ell}{2mc} (L_z + 2S_z) \tag{2.4.7}$$

$$\mu_{-1} = - \frac{\ell}{2mc} \frac{(L_x + 2S_x) - i(L_y + 2S_y)}{\sqrt{2}} \qquad (2.4.8)$$

The above components transform like basic function for the representation D_{1g} of the three dimensional rotation group, that is the magnetic dipole operator is an even operator. Therefore the following rules are obtained

$$\Delta J = 0 \pm 1, \qquad J_i = 0 \not\rightarrow J_f = 0$$

$$P_f = P_i$$

and in the Russell Saunders coupling we have

$$\Delta L = 0 \pm 1, \qquad \Delta L_i = 0 \not\rightarrow L_f = 0$$

$$\Delta S = 0$$

$$P_f = P_i$$

For the rare earths the valid rules are determined by the site symmetry. However, because of the weak crystal field the selection rules of the free ion have still some relevance. Electric dipole transition within an f^n configuration are allowed only due to environmental perturbation. Thus, the selection rules are determined strictly by the local field symmetry at the site of the ion.

Using group theory we ascertain whether a transition between two representations is allowed. A transition between two representations is allowed, if the product of the representation of the initial state by the representation of a component of the transition operator contains the final state. This is strictly related to the polarization of the radiation. This can be stated in the following way :

$$\Gamma \times \Gamma_i = \Gamma_f$$

2.5 INTENSITY CALCULATION

Studies on the intensities of lanthanide f → f spectra began with a seminal paper published in 1937 by Van Vleck [7]. In this paper Van Vleck discussed and calculated the intensities of the transitions on the basis of two possibilities: (i) transitions may occur within the $4f^N$ configuration or (ii) transitions may occur between different configurations, $4f^{N-1}5d$. Thus, the transitions would occur either by an allowed electric dipole mechanism or by a forced electric dipole or electric quadrupole mechanism. Based on the calculations and the "extra" lines which appeared in the spectra of most solid lanthanides Van Vleck concluded that much of the intensity was due to the vibronically induced absorption of electric dipole radiation.

In 1942 a group of researchers at the Zeeman Laboratories made the first accurate measurements of the absolute intensities of lanthanide spectra and published a very important paper [15] on the origin of the intensities. The group reached different conclusions from those of Van Vleck, and are in agreement with present day opinion.

The next major step in the theory of lanthanide intensities occurred in 1962, with the simultaneous publication of the results of two independent investigations by Judd [16] and Ofelt [17]. Judd and Ofelt derived an expression for the oscillator strength of induced electric dipole transitions within the f^N configuration. In the following section we will discuss the Judd-Ofelt theory in the framework of what is necessary in this thesis.

2.5.1 Judd-Ofelt Theory

The Judd-Ofelt theory makes ample use of the formalism of tensor operators, n-j symbols and reduced matrix elements. We propose to give a brief account of the major relationships obtained by Judd and Ofelt and refer the reader to the original papers by Racah [18], and books by Edmonds [19], Judd [5], and Wybourne [2] for an account of the above mentioned subjects.

The transition probability due to dipole radiation may be expressed as

$$A(a, a') = \frac{64\pi^4\sigma^3}{3h} \left| \left\langle a \middle| D \middle| a' \right\rangle \right|^2 \qquad (2.5.1.1)$$

where a and a' signify the initial and the final state, A is the transition probability per unit time, σ (cm^{-1}) is the energy difference between states and D is the dipole operator.

Broer et al. [20] defined the oscillator strength as

$$f = \frac{Amc}{8\pi^2\sigma^2e^2} \tag{2.5.1.2}$$

substituting for A in equation 2.5.1.2, the oscillator strength may be written as

$$f = \frac{8\pi^2\sigma\, mc}{3he^2} \left|\langle a | D | a' \rangle\right|^2 \tag{2.5.1.3}$$

Since the matrix elements of D are summed over all components of the initial state the factor 2J+1 must be added. Equation 2.5.1.3 may be written as

$$f = \frac{8\pi^2\sigma\, mc}{3he^2(2J+1)} [\chi\overline{F}^2 + nM^2] \tag{2.5.1.4}$$

where F^2 and M^2 represent the matrix elements of the electric and magnetic dipole operators respectively, $\chi = n(n^2+2)^2/9$ the Lorentz Field Correction, a correction for the refractive index , n, of the crystal.

The expression for the oscillator strength given by the Judd-Ofelt theory is the following:

$$f = \sum_{\lambda=2,4,6} T_\lambda \nu \left(\psi J \| U^{(\lambda)} \| \psi' J'\right)^2 \tag{2.5.1.5}$$

where ν is the mean frequency of the transition $\psi J \rightarrow \psi J'$, $U^{(\lambda)}$ is a unit tensor operator of rank λ, the sum is over λ = 2,4,6 and T_λ are three parameters which can be calculated from experimental data. The parameters T_λ contain the radial parts of the $4f^N$ wave functions, the wave functions of perturbing configurations such as $4f^{N-1}5d$ and the interaction between the central ion and the local environment.

Judd defined T_λ as

$$T_\lambda = \frac{8\pi^2 m}{3h(2J+1)} \left[\frac{\left(n^2+2\right)^2}{9n}\right] (2\lambda+1) \sum_t (2t+1)\, B_t I^2(t,\lambda) \tag{2.5.1.6}$$

substituting equation 2.5.1.6 into equation 2.5.1.5 gives

$$f = \frac{8\pi^2 m\nu}{3h(2J+1)} \left[\frac{\left(n^2+2\right)^2}{9n}\right] \sum_{\lambda=2,4,6} \Omega_\lambda \left(\psi J \| U^{(\lambda)} \| \psi' J'\right)^2 \tag{2.5.1.7}$$

where

$$\Omega_\lambda = (2\lambda+1)\sum_t (2t+1)\, B_t I^2(t,\lambda) \qquad (2.5.1.8)$$

and denotes the Judd-Ofelt parameters.

The matrix elements in equation 2.5.1.7 may be calculated in the SL basis using the following relation:

$$(f^N\alpha SLJ\|U^{(\lambda)}\|f^N\alpha' S' L' J') = \delta(S,S')(-1)^{S+L'+J+\lambda}[(2J+1)(2J'+1)]^{1/2}$$

$$\begin{Bmatrix} J & J' & \lambda \\ L' & L & S \end{Bmatrix}(f^N\alpha SL\|U^{(\lambda)}\|f^N\alpha' S' L') \qquad (2.5.1.9)$$

The reduced matrix elements have been tabulated by Nielson and Koster [21]. The matrix elements of $U^{(\lambda)}$ have been calculated for various transitions for the lanthanide ions and are given by Carnall et al [22]. These matrix elements are host independent.

For electric and magnetic dipole transitions the respective dipole operators are given by

$$F_e^2 = e^2 \sum_{\lambda=2,4,6} \Omega_\lambda \left(\psi J \left\| U^{(\lambda)} \right\| \psi' J' \right)^2 \tag{2.5.1.10}$$

and

$$M_M^2 = \frac{e^2}{4m^2c^2} \left(\psi J \| L + 2S \| \psi' J' \right)^2 \tag{2.5.1.11}$$

The transition probability between the individual components a and a′, $A_{aa'}^{emis}$ for the emission process is given by

$$A_{aa'}^{emis} = \frac{32\pi^3 e^2 \sigma^3}{3\eta 4\pi\varepsilon_0} \left[\left(\frac{n(n^2+2)^2}{9} \right) F^2 + n^3 M^2 \right] \tag{2.5.1.12}$$

where the symbols have their normal meaning.

The total radiative relaxation rate $A_T(\psi J)$ is given by

$$A_T(\psi J) = \sum_{\psi' J'} A(\psi J, \psi' J') \tag{2.5.1.13}$$

where the sum runs over all states lower in energy than the fluorescing state. Two other useful parameters are the radiative branching ratio β_R

$$\beta_R(\psi J, \psi' J') = \frac{A(\psi J, \psi' J')}{A_T(\psi J)} \tag{2.5.1.14}$$

and the radiative lifetime of a state is

$$\tau_T(\psi J) = \left[A_T(\psi J)\right]^{-1} \tag{2.5.1.15}$$

From the experimental absorption spectrum the oscillator strengths may be obtained using the following

$$f_{aa'}^{exp} = \left[\frac{9n}{(n^2+2)^2}\right] \frac{4mc\varepsilon_0}{Ne^2} \int \mu(\nu)d\nu \tag{2.5.1.16}$$

where N is the dopant concentration expressed in number of ions/cm^3 and $\int \mu(\nu)d\nu$ is the integrated absorption co-efficient of the transition between the J states a and a′.

2.6 ENERGY TRANSFER

The non-radiative transfer of the energy of electronic excitation from excited ions to non-excited ones plays an essential role in luminescence. Resonant transfer of electronic excitation energy from a sensitizer (donor) to an activator (acceptor) has been a subject of many investigations [23-25]. Many theories have been developed such as the one by Förster [26] which give formulae for the rate of energy transfer by electric-dipole-dipole interaction. This theory was extended by Dexter [28] to include higher order multipole interactions such as electric-dipole-quadrupole interaction and exchange interaction. The electric-dipole-dipole/quadrupole interactions are electrostatic in origin, while the exchange interaction arises from requirement of the antisymmetry of the electronic wavefunction for the system consisting of donor and acceptor molecules. The donor-acceptor distance plays an important role in the transfer mechanisms, and an overlap between the donor emission spectrum and the acceptor absorption spectrum is essential for the transfer to occur.

Luminescence measurements allows the experimental studies of resonance transfer, where the donor molecules are excited in the presence of acceptor molecules, and the resulting luminescence of donor and/or acceptor in addition to their decay times are measured as functions of concentration. Inokuti and

Hirayama [28] studied the decay time of donor luminescence as functions of the acceptor concentration, for energy transfer by exchange mechanism. Their results provide a sound quantitative basis for analyzing experimental data for this kind of energy transfer, just as Förster's theory has long been doing for dipole-dipole transfer.

2.6.1 Transfer Probabilities

Interactions between rare-earth ions are given by the following Hamiltonian

$$H = H_0 + H_{da} \tag{2.6.1.1}$$

The Hamiltonian is separarted into two parts, H_0 which describes the single ion interactions and H_{da} describing the interactions between two separated ions, that is the Coulomb Coupling between the electrons of neighboring RE^{3+} ions. The interaction Hamiltonian H_{da} between donor (d) and acceptor (a) is of the form

$$H_{da} = \frac{1}{K} \sum_{i,j} \frac{e^2}{\vec{r}_i - \vec{r}_j} \tag{2.6.1.2}$$

where κ is the dielectric constant, and the summation is over the electrons i and j of the donor and acceptor respectively. This represents the Van der Waals interaction for isolated ions in solution in a solid or liquid and the wavefunctions are composed of a properly symmetrized superposition of single ion states. The calculation of the transfer rate involves Fermi's Golden rule

$$P_{da} = \pi \left| \langle \psi_1 \, | H_{da} | \, \psi_2 \rangle \right|^2 \rho_e \qquad (2.6.1.3)$$

where ρ_e is the density of final states and the term in brackets is the matrix element of the donor-acceptor interaction Hamiltonian between ψ_1 the initial state with the donor excited, and ψ_2 the final state with the acceptor excited. Dexter [27] has shown that the density of final states in eq. 2.6.1.3 can be expressed in terms of an overlap integral between the donor emission spectrum and acceptor absorption spectrum. In the case of different sites this interaction will also mix the wavefunctions, leading to processes such as cooperative absorption and emission where two ions couple to a single photon. This is true for both absorption [29] and emission [30]; however, it is very weak and will not be considered further. In order to compute the transfer probability, the interaction Hamiltonian H_{da} is expanded in a Taylor series about the vector R (the separation of the nucleus of the donor and acceptor) giving

$$H_{da} = \frac{e^2}{\kappa R^3}\left\{\vec{r}_d\cdot\vec{r}_a - 3(\vec{r}_d\cdot\vec{R})/R^2\right\} + \frac{3e^2}{2\kappa R^4}\left\{\sum_{i=1}^{3}\left(\frac{R_i}{R}\right) r_{ai}^2 r_{di} + (-3 + 5\frac{R_i^2}{R^2})\right.$$

$$+ 10\left(\frac{XYZ}{R^2}\right)(x_a y_a z_d + x_a z_a y_d + y_a z_a x_d) + \sum^{3}\sum^{3}_{i\neq j}\left[\frac{R_i}{R} - \frac{5R_i^2 R_j}{R^3}\right]\times$$

$$\left.\left[-r_{ai}^2 r_{di} - 2r_{ai} r_{dj} r_{di}\right]\right\} + \dots\dots\dots\dots \tag{2.6.1.4}$$

The term in the first curly brackets represents the dipole-dipole interaction, and the second the dipole-quadrupole interaction; higher order interactions, including quadrupole dipole, have been omitted. In eq. 2.6.1.4, $r_d = \sum_m r_{d,m}$ refers to all the electrons on d, measured from its nucleus and similarly with $r_a = \sum_n r_{a,n}$; e is the magnitude of the electronic charge. The interactions are classified as standard multipole type interactions depending on various powers of $\langle r_d\rangle_{1,2} \equiv \langle 1|\,\vec{r}_d\,|2\rangle$ and $\langle r_a\rangle_{1,2} \equiv \langle 1|\,\vec{r}_a\,|2\rangle$ and the ion separation R. The interaction distance is short, which can make the ratio between the dipole-dipole and dipole-quadrupole terms $[\langle r\rangle_{1,2}/R]^2$ much larger than the comparable expansion parameter for radiative transitions $[\langle a\rangle_{1,2}/\lambda]^2$ [31].

The matrix elements $<r_d>_{1,2}$ and $<r_a>_{1,2}$ can be expressed in terms of the oscillator strengths, f [32]:

$$<r_d>_{1,2} = \frac{3e^2h}{2m\omega} f_d \qquad (2.6.1.5)$$

which in turn can be related to a measurable quantity such as the radiative lifetime τ :

$$\tau^{-1} = \frac{2e^2\omega^2}{mc^3} f_d \qquad (2.6.1.6)$$

or absorption cross-section σ

$$\int \sigma(\omega) d\omega = \frac{2\pi^2 e^2}{mc} f \qquad (2.6.1.7)$$

Hence the interaction parameter can be directly calculated from measurable quantities. Dexter [27] carried out the above substitutions keeping track of the various linewidths and overlaps, and obtained the following expression for dipole-dipole coupling :

$$P_{(dd)} = \frac{3h^4c^4}{4\pi n^4} \frac{Q_a}{\tau_d} \frac{1}{R^6} \int f_{abs}(\omega)\, f_{emit}(\omega)\, \frac{d\omega}{\omega^4} = \frac{C}{R^6} \qquad (2.6.1.8)$$

where

$$C = \frac{3h^4c^4}{4\pi n^4} \frac{Q_a}{\tau_d} \int f_{abs}(\omega)\, f_{emit}(\omega) \frac{d\omega}{\omega^4} \qquad (2.6.1.9)$$

$f_{abs}(\omega)$ and $f_{emit}(\omega)$ are the absorption and emission line shapes, $Q_a = \rho_\sigma(\omega)\, d\omega$, is defined as the area under the absorption band, τ_d is the radiative lifetime of the donor ions, and C represents the interaction parameter that characterizes the strength of the interaction.

The overlap between the donor emission and the acceptor absorption shows the resonant nature of the process, and reflects conservation of energy. Using spectroscopic measurements, the line shapes, lifetime, and cross-section can be easily obtained and can be used to calculate the strength of the energy transfer interaction.

In general the dipole-quadrupole transfer rate is not the same as the quadrupole-dipole transfer rate. The total transfer rate is equal to the sum of the transfer probabilities for each of these multipoles, which is often written with observations for the interaction strengths as

$$P_{da}(\text{total}) = \frac{C^{d-d}}{R^6} + \frac{C^{d-q}}{R^8} + \frac{C^{q-q}}{R^{10}} \qquad (2.6.1.10)$$

Higher order multipole interactions (dipole-quadrupole, quadrupole-quadrupole) can be calculated in the same way as for dipole-dipole. However, this is not done due to the difficulty in measuring experimentally the quadrupole moment of an ion, especially in the presence of a strong electric dipole moment. Contribution to the total transfer rate of order higher than quadrupole-quadrupole are usually negligible even for nearest neighbors.

Other types of interactions, where the Coulomb integrals may vanish due to selection rules, are made possible due to exchange. Exchange will allow transfer to and excitation of an acceptor by all types of allowed and forbidden transitions, including, for example L = 0 to L = 0 transitions. The transfer probability as a result of the exchange mechanism may be written as:

$$P_{da}(ex) = 2\pi Z^2 \int f_{abs}(\omega)\, f_{emit}(\omega)\, d\omega \qquad (2.6.1.11)$$

where Z is the wavefunction overlap given by

$$Z^2 = \frac{e^2}{g_d g_a \kappa^2} \int Q(\vec{r}_1)\left(\frac{1}{r_{12}}\right)Q(\vec{r}_2)d\vec{r}_1 d\vec{r}_2 \qquad (2.6.1.12)$$

where $Q(\vec{r}_1) = \psi'_d(\vec{r}_1)\psi_a(\vec{r}_1)$, is the charge density of the excited donor wavefunction and the ground state acceptor wavefunction. $Q(\vec{r}_2) = \psi'_a(\vec{r}_2)\psi_d(\vec{r}_2)$, is the charge density of the excited acceptor wavefunction and the ground state donor wavefunction. The values of Q are normalized over space (and are not an energy scale) such that Z^2 has the dimensions of energy squared. The separation and concentration dependencies are contained in Z^2, which varies approximately as $Y(e^4/\kappa^2\ R_0^2)\exp(-2R/L)$, where L is an effective Bohr radius for the excited and unexcited states of the donor and acceptor ions, and Y is a dimensionless quantity <<1. This is rarely used to calculate the interaction parameter directly, rather it is used to illustrate the short range nature of the interaction. In the case of the rare-earth ions, the overlap of the wavefunctions between neighbouring ions is very small, due to the shielding of the 4f electrons. A mechanism has been proposed which allows for the interactions through common ligands.

2.6.2 Time Dependence of the Donor Fluorescence

The energy transfer probability is strongly dependent on the distance R between the ions involved (see eq. 2.5.10). This implies that the distance-averaged transfer rate, which can be measured by the decay rate of the donor fluorescence, will not be constant in time (non-exponential decay). For an arbitrary distance-dependent donor-acceptor transfer probability P(R) excited donors will be quenched according to the following equation

$$<N(t)> = \exp \left\{- 4\pi n_a \int_0^\infty R^2 \, dR \, (1-e^{P(R)t}) \right\} \tag{2.6.2.1}$$

The above expression has been treated statistically, for energy transfers with randomly-distributed donor-acceptor distances for the pertinent forms of P(R) [33]. Inokuti and Hirayama [28] have shown that for a donor-acceptor multipole interaction of order S, the probability at time t after excitation of some arbitrary donor still being excited takes the form

$$\Phi_0(t) = \exp \left[(t/\tau) - (C/C_0) \, \Gamma\,(1 - 3/S) \, (t/\tau)^{3/S} \right] \tag{2.6.2.2}$$

where τ is the fluorescence life time for the donors in the absence of acceptors, C is the acceptor concentration, C_0 is the Dexter "critical concentration" defined as the concentration of acceptors for which the transfer rate equals the spontaneous decay rate, $\Gamma(x)$ represents the Euler gamma function; and S = 6 for dipole-dipole, S = 8 for dipole-quadrupole, and S = 10 for quadrupole-quadrupole interactions. For the dipole-dipole interaction, the expression yields the well-known Forster [34] result for the donor decay

$$<N(t)> = \exp(-\gamma\sqrt{t}) \qquad (2.6.2.3)$$

where

$$\gamma = \frac{4}{3}\pi^{3/2} n_a \sqrt{C_{da}} \qquad (2.6.2.4)$$

The above expressions account for energy transfer between donor and acceptors, however, energy transfer may also take place between donor ions. The latter must be considered for the interpretation of the temporal behavior of donor fluorescence due to energy transfer. The decay may be greatly altered, if a large number of donor-donor transfers take place before donor-acceptor transfer. The donor-acceptor transfer will be dominated by transfer between adjacent ions, which is greater than that allowed by the initial distribution of excited donors (Fig 2.6.2.1).

Different theories have been developed to explain the donor-assisted transfers. However, the most commonly used are: (i) the diffusion model [35] applicable to systems where donor-donor transfer is non-negligible but does not dominate donor-acceptor transfer and (ii) the hopping model [36] applicable when donor-donor transfer dominates donor-acceptor transfer.

The most direct result of diffusion is to remove the variation in donor environments. The excitation can transfer to the acceptor more efficiently by diffusing through the sublattice of donors to interact at a much shorter distance rather than directly interacting over a larger distance. If the diffusion rate is much faster than the average donor-acceptor interaction rate, the donor-acceptor transfer will be over roughly the same distance for the entire ensemble. This leads to an exponential decay reflecting the smoothing out of the local variation in number and distance of acceptors.

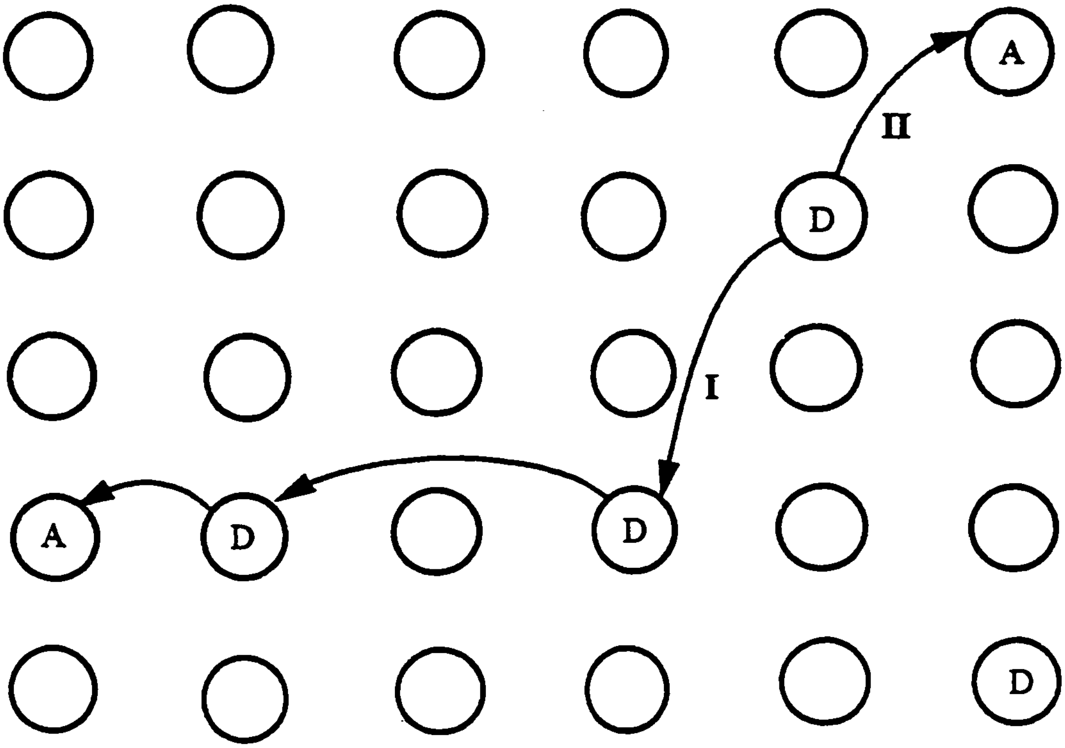

Figure 2.6.2.1 : Migration-assisted energy transfer. If donor-donor transfer is more probable than donor-acceptor transfer, then process I will be more probable than process II, direct donor-acceptor transfer.

Experimentally, both a non-exponential decay at short times and a longer exponential tail are observed at moderate donor concentration (N_{donor} ~ 5%). The reason for this behavior is due to the fact that some sites will interact directly with nearby acceptors, while others with no adjacent acceptors will decay with a slower rate. The latter will show enhanced decay rates since the excitation has migrated closer to an acceptor. The fluorescent decay is given by

$$\frac{I(t)}{I_0} = \exp\left[-At - B\sqrt{t} \right] \tag{2.6.2.5}$$

where A is the sum of the intrinsic decay rate τ_0^{-1} and the decay due to migration assisted energy transfer ω :

$$\tau^{-1} = \tau_0^{-1} + \omega \tag{2.6.2.6}$$

B represents the energy transfer rate due to migration and is used to calculate the microscopic interaction parameter.

The hopping model considers the transfer of excitation from donor to donor as occurring through a random walk of the donor excitation among the donor sites. The hopping of excitation is assumed to continue until the excitation decays spontaneously or is annihilated by transfer to an acceptor. The problem has been solved by considering the annihilation of the donor excitation as occurring within a finite region around each acceptor. The donor migration continues undisturbed outside this region, and is annihilated by the acceptor in case it hops inside the region. If the excitation can be annihilated in one hop, each hop can be treated as random and uncorrelated with regard to the strength of the donor-acceptor interaction. Hence the statistical parameter ϕ, the probability that a donor is still excited after some time interval is given by

$$\phi(t) = \phi_0(t)\, e^{-t/\tau_0} + \tau_0^{-1} \int_0^t \phi(t')\, \phi_0(t - t')\, e^{-(t - t')/\tau_0}\, dt' \qquad (2.6.2.7)$$

where ϕ_0 has been defined previously in eq. 2.6.2.2 and τ_0 is the average time for an excitation hop. Equation 2.6.2.7 can be solved numerically, and when the donor-donor and donor-acceptor interactions are strictly dipole-dipole this equation gives the time dependence of the donor fluorescence intensity at short times. This is described by the following equation

$$I(t) = I_0 \exp\{ -t/\tau - \gamma\sqrt{t} - \varpi t \} \qquad (2.6.2.8)$$

where

$$\gamma = 4/3\ \pi^{3/2}\ n_a \sqrt{C_{da}} \tag{2.6.2.9}$$

and

$$\varpi = \pi\ (2\pi/3)^{3/2} \sqrt{C_{da}} \sqrt{C_{dd}}\ n_a n_d \tag{2.6.2.10}$$

where n_a and n_d are the dopant concentrations of the acceptor and donor respectively, and C_{da} and C_{dd} are the dipole-dipole interaction strengths for donor-acceptor and donor-donor transfer respectively. Hence, in the case of a very fast donor-donor migration ($C_{dd} >> C_{da}$) the system behaves as if dominated by a single donor-acceptor transfer rate and the donor decay is again exponential. This expression stands for times much shorter than the time of a donor-donor hop [37], and must be used cautiously.

2.7 REFERENCES

1. S. Hüfner, “Optical Spectra of Transparent Earth Compounds”, Academic Press Inc., London (1978).
2. B. G. Wybourne, “ Spectroscopic Properties of Rare Earth”, Wiley, New York (1965).
3. G. H. Dieke, “Spectra and Energy Levels of Rare Earth Ions in Crystals”, Wiley, New York (1968).
4. C. W. Nielson, and G. F. Kroster, “Spectroscopic co-efficients for the p^n, d^n, and f^n configurations”, M. I. T. Press, Cambridge, MA. U.S.A. (1963).
5. R. B. Judd, “Operator Techniques in Atomic Spectroscopy”, McGraw-Hill, New York, NY. U.S.A. (1963).
6. H.A. Bethe, Ann. Physik, 3, 133 (1929).
7. J. H. Van Vleck, J. Phys. Chem., 41, 67 (1937).
8. A. Abragam, H. M. L. Pryce, Proc. Roy. Soc. (London), A205, 135 (1951).
9. R.J. Elliott, K.W.H. Stevens, Proc. Roy. Soc. (London) A, 215, 437 (1952).
10. R.J. Elliott, K.W.H. Stevens, Proc. Roy. Soc. (London) A, 219, 387 (1953).
11. R.P. Leavitt, C.A. Morrison, D.E. Wortman, Rare Earth ion-host crystal field interactions. Three parameter theory of crystal fields. Harry Diamond Laboratories, Report TR-1673 (1975).

12. R.M. Sternheimer, M. Blume, R.F. Peierls, Phys. Rev., 173, 376 (1968).

13. C.A. Morrison, R.P. Leavitt, J. Chem. Phys., 71 (6), 2366 (1979).

14. N.C. Chang, J.B. Gruber, R.P. Leavitt, C.A. Morisson, J. Chem. Phys., 78, 3877 (1982).

15. a) J.P.M. Wonderberg, Physica, 9, 217, 936 (1942).

    b) J. Hoogschagen, Physica, 11, 513 (1943).

    c) J. Hoogschagen, A.P. Snoek, C.J. Gorter, Physica, 11, 518 (1943).

16. R. B. Judd, Phys. Rev., 127, 750 (1962).

17. G. S. Ofelt, J. Chem. Phys., 37, 511 (1962).

18. a) G. Racah, Phys. Rev., 62, 438 (1942)

    b) G. Racah, Phys. Rev., 63, 367 (1943).

19. A.R. Edmonds, Angular momentum in quantum mechanics, Princeton, Princeton University Press (1960).

20. L.J.F. Broer, C. J. Gorter, J. Hoogschagen, Physica, 11, 231 (1945).

21. C.W. Nielson, G. F. Kroster, M. I. T. Press, Cambridge, MA. U.S.A. (1963).

22. W.T. Carnall, P.R. Fields, K. Rajnak, J. Chem. Phys., 49, 4424 (1968).

23. Th. Förster, Disc. Faraday Soc., 27, 7 (1959).

24. Th. Förster, Radiation Res. Suppl., 2, 326 (1960).

25. A.N. Terenin, Usp. Fiz Nauk, 43, 47, (1951) [English transl. : AEC-tr-3031-(1958)]

26. Th. Förster, Ann. Phys., 2, 55 (1948).

27. D. L. Dexter, J. Chem. Phys., 21, 836 (1953).

28. M. Inokuti, F. Hirayama, J. Chem. Phys., 43, 1978 (1965).

29. F. Varsanyi, G. H. Dieke, Phys. Rev. Lett., 7, 442 (1961).

30. E. Nakazawa, S. Shinoya, Phys. Rev. Lett., 25, 1710 (1970).

31. D. L. Dexter, J. H. Schulman, J. Chem. Phys., 22, 1063 (1954).

32. R. C. Hilborn, Am. J. Phys., 50, 982 (1982).

33. S. I. Golubov, Yu. V. Konobeev, Sov. Phys. Sol. Sta., 13, 2679 (1972).

34. Th. Förster, Z. Naturforsch., A4, 321 (1949).

35. M. Yokota, O. Tanimoto, J. Phys. Soc. Jap., 22, 779 (1967).

36. A. I. Burshtein, Sov. Phys. JETP, 35, 882 (1972).

37. L. D. Zusman, Sov. Phys. JETP, 46, 347 (1977).

CHAPTER 3

3. EXPERIMENTAL

3.1 CRYSTAL GROWTH

The yttrium vanadate crystals doped with different concentrations of Er^{3+} were grown at the University of Parma, Italy using the flux technique. The $YVO_4:Er^{3+}$ crystals were grown using the techniques [1,2] developed for the synthesis and growth of rare-earth orthophosphate (RPO_4) and orthoarsenate ($RAsO_4$) single crystals from molten salt solutions. The procedure involves the dissolution of a rare-earth oxide in melted lead pyrophosphate ($Pb_2P_2O_7$) for RPO_4 or lead pyroarsenate ($Pb_2As_2O_7$) for $RAsO_4$ at high temperatures, with spontaneous nucleation and crystal growth of the desired crystal via slow cooling of the solution.

Yttrium vanadate is isomorphic to yttrium phosphate and arsenate and has the tetragonal xenotype structure (D_{4h}^{19} - $I4_1/amd$) [3]. The crystallographic and chemical relationship between these compounds suggested that, if a suitable solvent comparable to $Pb_2P_2O_7$ and $Pb_2As_2O_7$ existed in the lead- vanadium-oxygen system, the flux growth technique could be extended to the synthesis and growth of rare-earth orthovanadates.

The compound $Pb_2V_2O_7$ exists and melts congruently at about 725°C which is not very different from $Pb_2P_2O_7$ (824°C) or $Pb_2As_2O_7$ (780°C). $Pb_2V_2O_7$ can be easily prepared by direct fusion of the appropriate oxides. Therefore using $Pb_2V_2O_7$ as the solvent, single crystals of yttrium vanadate could be produced [4,5].

Nine grams of Y_2O_3 (yttrium oxide) were added to 91g of V_2O_5 and 214g of reagent grade PbO (lead oxide). The reactants were placed in a 100 ml platinum crucible with the yttrium oxide at the bottom. The crucible was covered with a platinum lid and heated to 1330°C. The mixture was held at this temperature for 14 hours and then slowly cooled to 950°C at 1-2 °C/hr. At 950°C the furnace was turned off and the sample cooled in situ. The crystals formed were embedded in a matrix of the solidified flux which could be easily removed with dilute nitric acid.

The $Pb_2V_2O_7$ flux is a good solvent for growing the vanadate crystals because of its ease of preparation and extremely low vapor pressure. Low surface evaporation is related to small concentration gradients, and premature formation of nucleation sites near the surface is avoided. For this reason it is probable that much larger YVO_4 crystals can be grown if this flux mixture is used in combination with the Czochralski or Bridgeman techniques, and an appropriate temperature gradient. The YVO_4 doped crystals (0.1, 1, 2.5 , and 10 % Er^{3+} by weight) grew either in the form of long, clear pink rods about 7.5 mm x 2 mm x 2 mm or clear pink plates of dimensions 5 mm x 3 mm x 1 mm. The trivalent erbium ions enter substitutionally for Y^{3+}. Using the crystallographic data and the nominal concentration we calculated the corresponding Er^{3+} concentrations in ions/cm^3 (Table 3.1.1).

Table 3.1.1: Concentration of Er^{3+} in YVO_4 given in percent and ions /cm^3

Concentration (% Er^{3+})	Concentration (10^{20} Er^{3+} / cm^3)
0.1	0.1253
1.0	1.253
2.5	3.133
10	12.53

3.2 CRYSTAL STRUCTURE

Crystallographic investigations by Chakoumakos [6] have shown that YVO_4 crystals are tetragonal, belonging to the space group $I4_1/amd$ (D_{4h}^{19}) with unit cell parameters, a = b = 7.1183 Å, c = 6.2893 Å, Z = 4. There is only one yttrium site for which the rare earth dopant may substitute. The ionic radii of Er^{3+}, Y^{3+} and V^{5+} are 103, 104, and 68 pm, respectively. The yttrium site is D_{2d} and is co-ordinated by eight oxygens. Each vanadium is co-ordinated by four oxygens in a nearly tetrahedral geometry (Fig 3.2.1). The V-O bond length is almost invariant throughout the lanthanide orthovanadate series (≈ 1.76 Å) and is shorter than the sum of the lanthanide and oxygen radii [7]. Each lanthanide is linked to two vanadate tetrahedra via edge sharing and to four other tetrahedra through a single bridging oxygen. The RV_2O_{10} is composed of two complete vanadate units on each side of the rare-earth atom. In Table 3.2.1 we show the crystallographic data for YVO_4. Figure 3.2.2 shows the oxygen nearest neighbors in the rare earth site [8].

Table 3.2.1 : Crystallographic data for YVO_4

Ion	Position	Symmetry	x	y	z
Y	4a	D_{2d}	0	0	0
V	4b	D_{2d}	0	0	1/2
O	16h	C_s	0	x	z

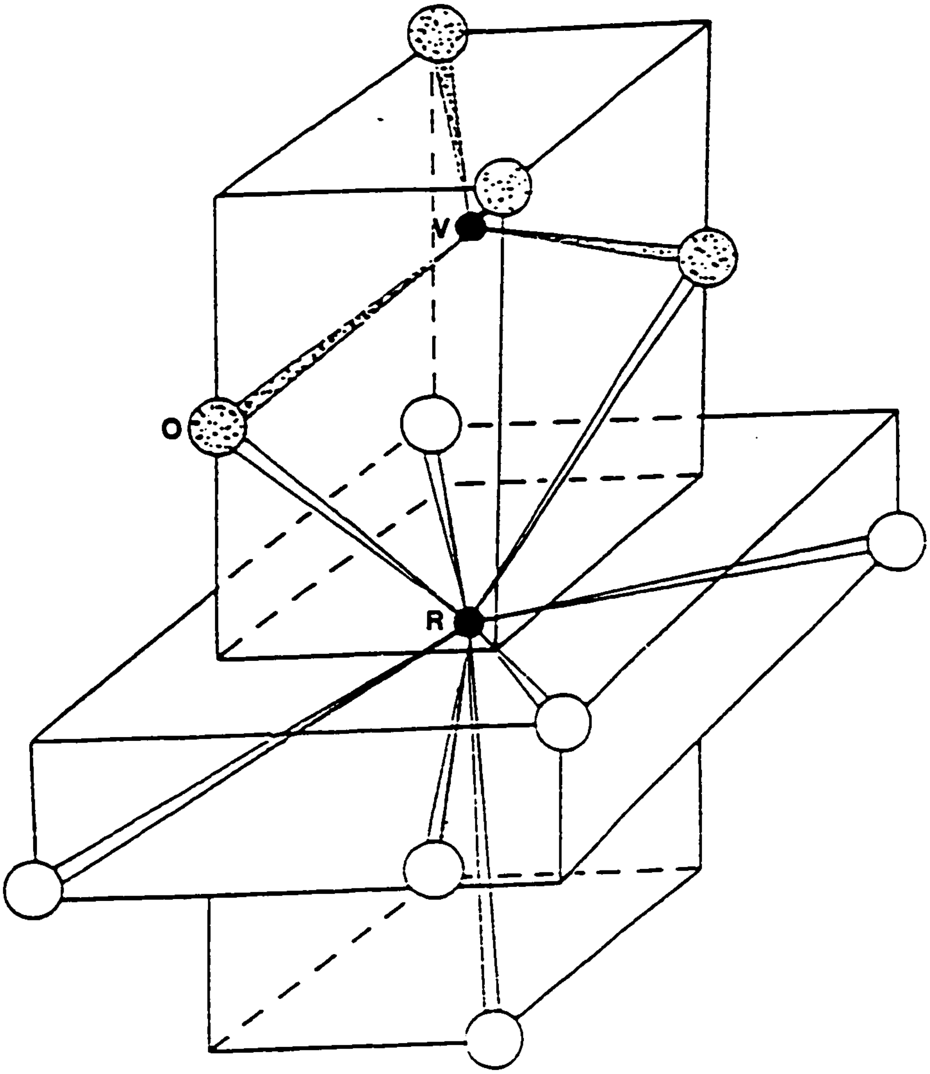

Fig 3.2.1 : The RV_2O_{10} zircon structure which is composed of two complete vanadate units on each side of the rare-earth atom.

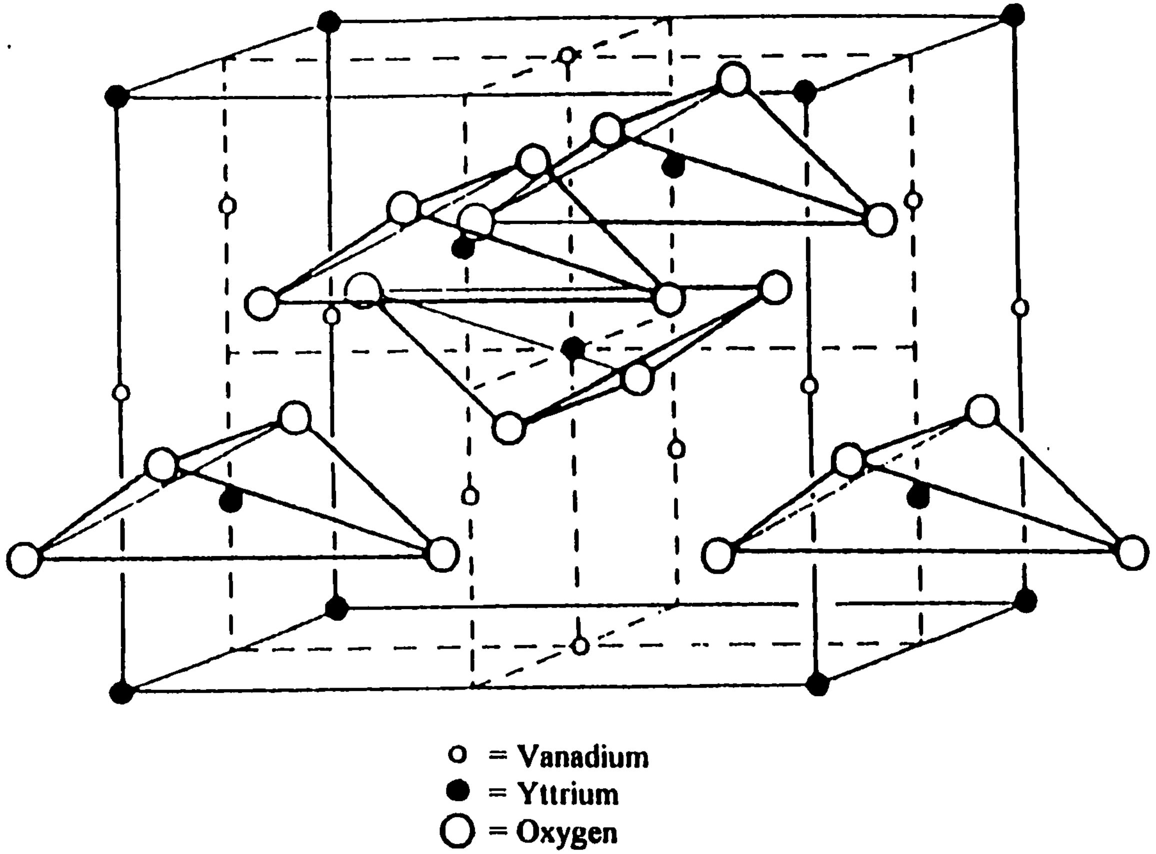

Fig 3.2.2 : The tetragonal unit cell of yttrium vanadate. The cell contains four YVO_4 molecules. Eight face- oxygen ions associated with four vanadium-oxygen tetrahedra that are located at four off-center face positions of vanadium have been omitted from the cell for the purpose of clarity.

3.3 SPECTROSCOPY

3.3.1 Absorption and Fluorescence

The absorption spectra were recorded with a computer controlled Cary 5E spectrophotometer. The instrument was equipped with the appropriate sources for the ultraviolet, visible and infrared regions. A Hamamatsu R928 photomultiplier tube was used for the ultraviolet and visible region and a thermoelectrically cooled Pb-S detector for the infrared region. The infrared detector has fairly low sensitivity and high noise, limiting the resolution of the spectrum in the infrared to approximately 0.1 nm, compared to a resolution of 0.05 nm in for the ultraviolet-visible region.

Fluorescence spectra were obtained by excitation with a tunable dye laser (Spectra Physics 375) operating with DCM (Concentration = 1.5×10^{-3} M dissolved in a 7:2:1 benzyl alcohol, glycerol, ethylene glycol solvent mixture) pumped by a Coherent CR-18 25W argon ion laser. The dye laser was also used, to pump in the vicinity of the ${}^4F_{9/2} \leftarrow {}^4I_{15/2}$ transition (652.7 nm). The argon ion laser was also used to pump a $Ti:Al_2O_3$ laser (titanium sapphire laser) . Both the dye and titanium sapphire lasers were used in the study of direct fluorescence as well as for the energy transfer and upconversion studies.

The pump beam was focused and horizontally directed through the crystal, and the line of fluorescence was imaged onto the slit using a camera lens. The sample was positioned such that the pumped region was at the surface of the crystal in order to eliminate any self absorption effect. The spectra were recorded using a Jarrell-Ash 1-meter Czerny Turner double monochromator and a maximum slit width of 150 μm. The gratings are mounted on a cosecant bar driven by a stepper motor with a step size of 0.01 cm^{-1}/step. The signal was monitored by an RCA-C31034-02 photomultiplier, which has a flat spectral response from 200 to 850 nm. The photomultiplier tube was thermoelectrically cooled so that the background dark count rate was below 10 counts per second. The photomultiplier signal is processed by a preamplifier model SR 440 Stanford Research Systems. The preamplifier contains four wide band width, dc-coupled amplifiers designed to be used independently or cascaded to provide gains of 5, 25, 125, and 625 thus amplifying the output from the photomultiplier tube to the photon counter. A gain of 25 was used in all of the experiments.

The gated photon counter Model SR 400 Stanford Research Systems is a data acquisition system that interfaces between the computer and the spectroscopic hardware shown in figure 3.3.1.1. The signal is recorded under computer control using the Stanford SR465 software data acquisition/analysis system. Low

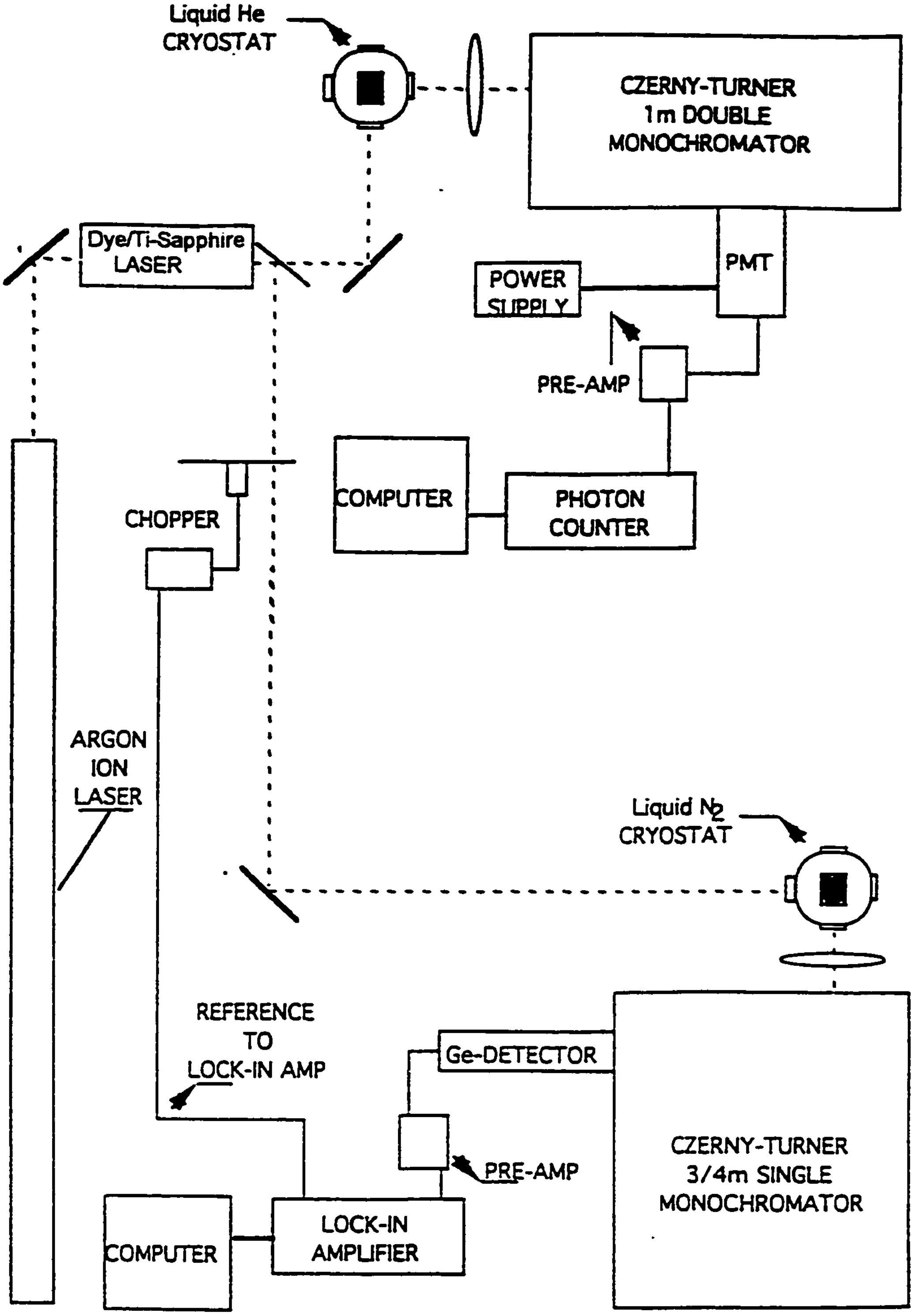

Figure 3.3.1.1 : Schematic arrangement of the apparatus for the measurement of the emission spectra and decay times.

temperature spectra were acquired using a Janis Research STVP-4 continuous flow cryostat.

The infrared emission spectra were recorded with a Jarrell-Ash 3/4 meter monochromator in second order. The fluorescence signal was monitored with a North Coast EO-817P, liquid nitrogen cooled germanium detector and analyzed using a Stanford Research SR 510 Lockin amplifier.

3.3.2. Lifetime Measurements

Decay and rise time measurements were obtained by exciting the samples with the pulsed radiation of a frequency doubled Nd^{3+}:YAG laser-pumped dye laser (Quantel Model Datachrom) associated with a hydrogen Raman cell. The laser delivers excitation pulses of 15 ns duration and 0.1 cm^{-1} spectral width and the Raman cell shifts the energy of the dye laser beam going through it by $\pm$ 4155 cm^{-1} and $\pm$ 2×4155 cm^{-1} (plus sign for anti-Stokes, minus sign for Stokes). With the aid of the Raman cell we are able to excite directly the high energy levels of the Er^{3+} ion located in the ultraviolet-visible region of the spectrum, using the Raman anti-Stokes one and two of the laser radiations obtained with dyes such as Rhodamine R590 (Exciton denomination). The fluorescence was analyzed using a

Jobin-Yvon model H25 monochromator, with a 600 groves/mm grating blazed at 1 µm, and detected by a very sensitive and fast A-D-C model 403 HL (with a time response of about 500 ns) liquid nitrogen cooled germanium photodiode, for the infrared region. A Hamamatsu 1477 photomultiplier was used to monitor the signal in the visible. The signals were fed into a LeCroy model 9400 Digital Oscilloscope interfaced to a computer.

Fluorescence lifetime measurements were also obtained using an argon ion laser, a dye laser (DCM dye), or a Ti-Sapphire laser excitations with the aid of a Stanford Research optical chopper, Model SR 450. The photon counter was triggered by a Photodiode synchronized by the laser pulse. The fluorescence was analyzed using a Tektronix TDS 520A two channel digitizing oscilloscope (500 MHz).

3.4 REFERENCES

1. P. Sueptitz, J. Teltow, Phys. Status Solidii, 23 (1), 9 (1967).
2. R. W. Dreyfus, A. S. Nowick, Phys. Rev., 126 (4), 1367 (1962).
3. M. Dubois, P. Berge, G. Blanc, Disc. Faraday Soc., 31, 167 (1961).
4. G. Garton, S. H. Smith, B. M. Wanklyn, Crystal Growth, 13/14, 588 (1972).
5. R. S. Feigelson, Am. Ceram. Soc., 47 (5), 257 (1964).
6. B.C. Chakoumakos, M.M. Abraham, L.A. Boatner, J. Solid State Chem., 109, 197 (1994).
7. L. F. Johnson, H. J. Guggenheim, Appl. Phys. Lett., 19, 44 (1971).
8. P.P. Yaney, L.G. DeShazer, J. Opt. Soc. Am., 66 (12), 1405 (1976).

CHAPTER 4

4. RESULTS AND DISCUSSION

The first concern which arose when this thesis was initiated, was to determine the energy levels of Er^{3+} in YVO_4. Polarized absorption and emission spectra were measured at temperatures between 7K and 300K. The spectra were analyzed and a complete energy level scheme for Er^{3+} was determined. Crystal field calculations were performed and the crystal field parameters were obtained. Judd-Ofelt theory was applied to the room temperature absorption spectra to obtain the Judd-Ofelt parameters, predict the radiative decay rates and branching ratios for the Er^{3+} transitions from the various excited states to the lower J-manifolds. Upconversion and fluorescence dynamic studies are also presented. A comparison between the theoretical and experimental results made in this thesis for YVO_4:Er^{3+} will provide a useful assessment for the Er^{3+} ion in other vanadate host materials.

This chapter is divided into seven sections. The first section is dedicated to the derivation of the selection rules for the Er^{3+} ion in D_{2d} symmetry. Section two describes in detail the absorption and emission spectra. This is necessary in order to establish unequivocally the energy level diagram for Er^{3+} in YVO_4. The third section presents a detailed analysis of the intensities of the transitions and a discussion of the Judd-Ofelt parameters Ω_λ. Section four presents the crystal field analysis. Section five discusses the thermalization of the $^2H_{11/2}$ state. Lastly sections six and seven are dedicated to upconversion and fluorescence dynamics, respectively.

4.1 SELECTION RULES FOR ERBIUM (III) IN YVO_4

In the YVO_4 crystal there is only one site for which the Er^{3+} ions may substitute, this is the yttrium site. The yttrium site symmetry is D_{2d} and is co-ordinated by eight oxygens (see Figure 3.2.1).

Er^{3+} has a ground electronic configuration [Xe]$4f^{11}$ that is split by the Coulomb and spin orbit interactions into a number of multiplets. Figure 4.1.1 shows the multiplet structure of Er^{3+} where the multiplets are labelled using Russell-Saunders term(s) ($^{2S+1}L_J$) of their wavefunctions. The crystal field splits these multiplets as shown in figure 4.1.1. These levels are labelled by the double group irreducible representations (Γ_6 and Γ_7) of the D_{2d} point group and all crystal field states are doubly degenerate, Kramers doublets. Hund's rule requires that the

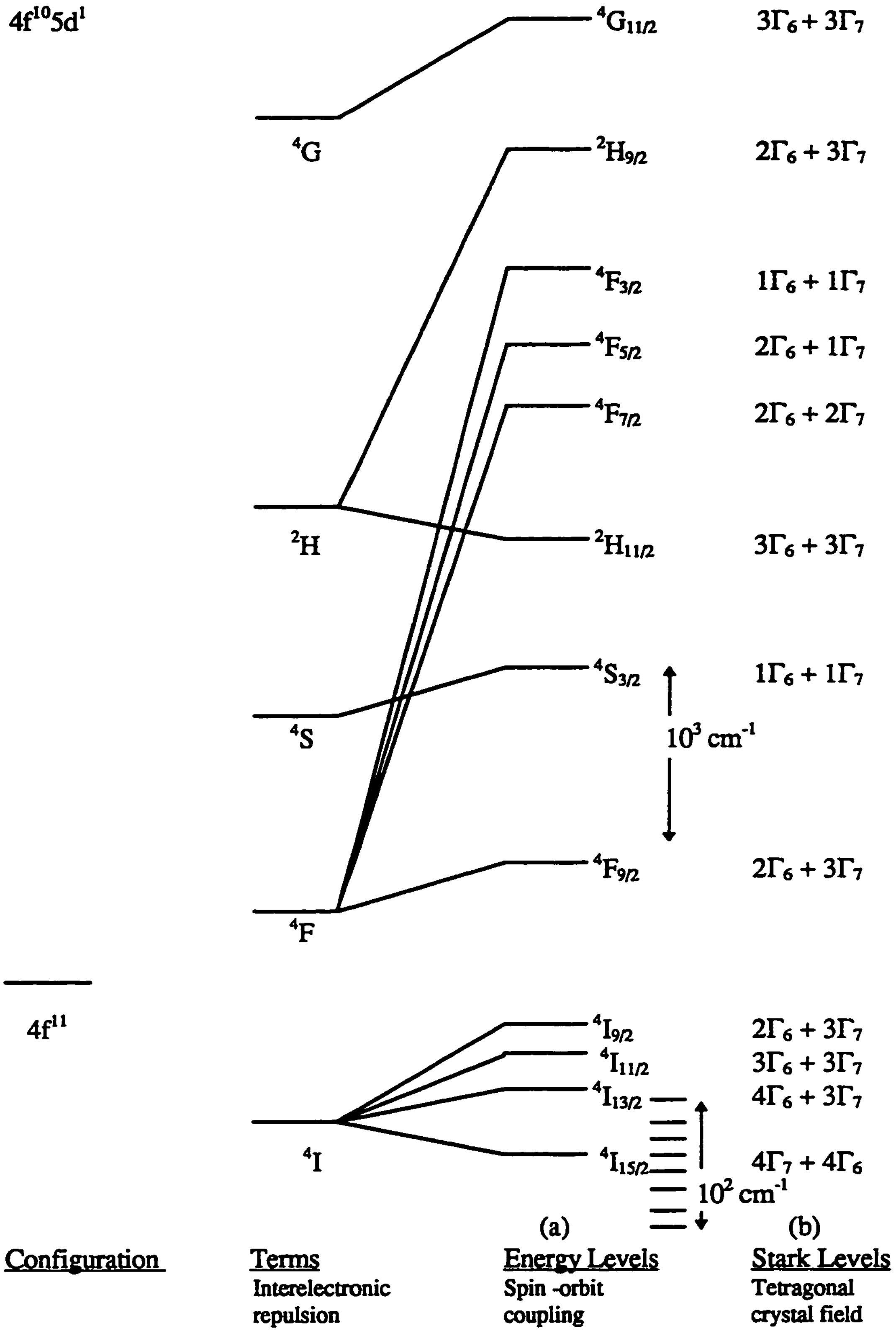

Figure 4.1.1 : Splitting of the LS terms of the $4f^{11}$ configuration by a) Spin orbit coupling of the free ion, and b) the influence of a tetragonal crystal field.

$^4I_{15/2}$ state be the ground and the excited states are the following : $^4I_{13/2,\,11/2,\,9/2}$, $^4F_{9/2,\,7/2,\,5/2,\,3/2}$, $^4S_{3/2}$, $^2H_{11/2,\,9/2}$, ...etc.

In section 2.4 we discussed how group theory is used in obtaining the selection rules. In this section we will apply group theory to the specific case considered in this thesis, Er^{3+} in D_{2d} symmetry.

The point group D_{2d} contains the following symmetry elements E, $2S_4$, C_2, $2C_2'$, and $2\sigma_d$. In Table 4.1.1 the character table for the point group is shown. The upper part of the character table is for terms with even J, whereas the lower part applies to terms with half integer J values. The latter is the case for Er^{3+}. Using Bethe's notation, the two irreducible representations appropriate for the J levels of Er^{3+} are Γ_6 and Γ_7. The corresponding irreducible representations using Mulliken's notation are 'E and 'E$_3$, respectively.

Using the following equation

$$\chi_J(\alpha) = \frac{\sin\left(J + \frac{1}{2}\right)\alpha}{\sin \alpha/2} \tag{4.1.1}$$

Table 4.1.1 : Character table for the group D_{2d}

D_{2d}		E	$2S_4$	C_2	$2C_2$'	$2\sigma_d$	
Γ_1	A_1	1	1	1	1	1	
Γ_2	A_2	1	1	1	-1	-1	R_Z
Γ_3	B_1	1	-1	1	1	-1	
Γ_4	B_2	1	-1	1	-1	1	Z
Γ_5	E	2	0	-2	0	0	(x,y) ; (R_x, R
Γ_6	‘E	2	$\sqrt{2}$	0	0	0	
Γ_7	‘E_3	2	$-\sqrt{2}$	0	0	0	

where α is the angle of rotation for each of the symmetry operations the full rotation group representation may be obtained (Table 4.1.2). The full rotation compatibility table (Table 4.1.3) is obtained using the following equation

$$P_{\Gamma_x}^{J} = \frac{1}{h}\sum n_R \chi_J \chi_{IR} \tag{4.1.2}$$

where h is the order of the group, n is the co-efficient of the operation, χ_J the value calculated from equation 4.1.1 and χ_{IR} the irreducible representations obtained from the character table.

A transition between two states may or may not be allowed in a particular polarization. The transition between two representations is allowed if the product of the initial state by the representation of a component of the transition operator contain the representation of the final state. Therefore, the allowdness is strictly related to the polarization of the radiation. In table 4.1.4 we show the selection rules for the electric dipole radiation for D_{2d} symmetry , where σ and π denote the occurrence of a transition in electric dipole radiation with the incident radiation polarized with its electric vector perpendicular or parallel to the crystal axis. The YVO_4 crystal is uniaxial and the c-axis coincides with the quantization axis.

Table 4.1.2 : Character table for the D_{2d} operator in the Full Rotation Group Representations*.

	E	S_4	C_2	C_2'	σ_d
$\overset{\pm}{D}_{1/2}$	2	$\pm\sqrt{2}$	0	0	0
$\overset{\pm}{D}_{3/2}$	4	0	0	0	0
$\overset{\pm}{D}_{5/2}$	6	$\mp\sqrt{2}$	0	0	0
$\overset{\pm}{D}_{7/2}$	8	0	0	0	0
$\overset{\pm}{D}_{9/2}$	10	$\pm\sqrt{2}$	0	0	0
$\overset{\pm}{D}_{11/2}$	12	0	0	0	0
$\overset{\pm}{D}_{13/2}$	14	$\mp\sqrt{2}$	0	0	0
$\overset{\pm}{D}_{15/2}$	16	0	0	0	0

* Er^{3+} has 11 electrons ($4f^{11}$), hence takes the negative signs.

Table 4.1.3 : Full rotation compatibility table for D_{2d} group.

J	Γ_6	Γ_7
1/2	0	1
3/2	1	1
5/2	2	1
7/2	2	2
9/2	2	3
11/2	3	3
13/2	4	3
15/2	4	4

Table 4.1.4 : Electric dipole selection rules for D_{2d} site symmetry, where + and - denote allowed and forbidden transitions respectively.

	σ polarization		π polarization	
	Γ_6	Γ_7	Γ_6	Γ_7
Γ_6	+	-	-	+
Γ_7	-	+	+	-

4.2 SPECTROSCOPY

4.2.1 Absorption Spectroscopy

Polarized absorption spectra of Er^{3+} in YVO_4 at 7 and 300K in the spectral range 300 to 1800 nm were used to assign the various Stark components of the following levels: $^4I_{15/2}$, $^4I_{13/2}$, $^4I_{11/2}$, $^4I_{9/2}$, $^4F_{9/2}$, $^4S_{3/2}$, $^2H_{11/2}$, $^4F_{7/2}$, $^4F_{5/2}$, $^4F_{3/2}$, $^2H_{9/2}$, $^4G_{11/2}$, and $^2K_{15/2}$. The temperature dependent absorption peaks (hot bands) were established by comparing the 7K spectrum with the absorption obtained at 300K. Analysis of the hot bands established the Stark levels of the $^4I_{15/2}$ ground state manifold at 38, 63, 143, 268 and 300 cm^{-1}. The higher levels of the ground state manifold were confirmed from the emission spectrum (see section 4.2.2). Absorption spectra were recorded for 0.1, 1, 2.5 and 10% Er^{3+} doped samples in both polarization and at low (T=7K) and room temperatures. The absorption spectra were found to be similar and the absorption coefficients are proportional to the Er^{3+} concentration. Figures 4.2.1.1 to 4.2.1.9 show the absorption spectra for the 2.5% Er^{3+}:YVO_4 sample at 7K and for two polarizations.

The effect of temperature is clearly demonstrated in Figure 4.2.1.10. In this figure we observe that at 7K only two peaks are observed. These two peaks may

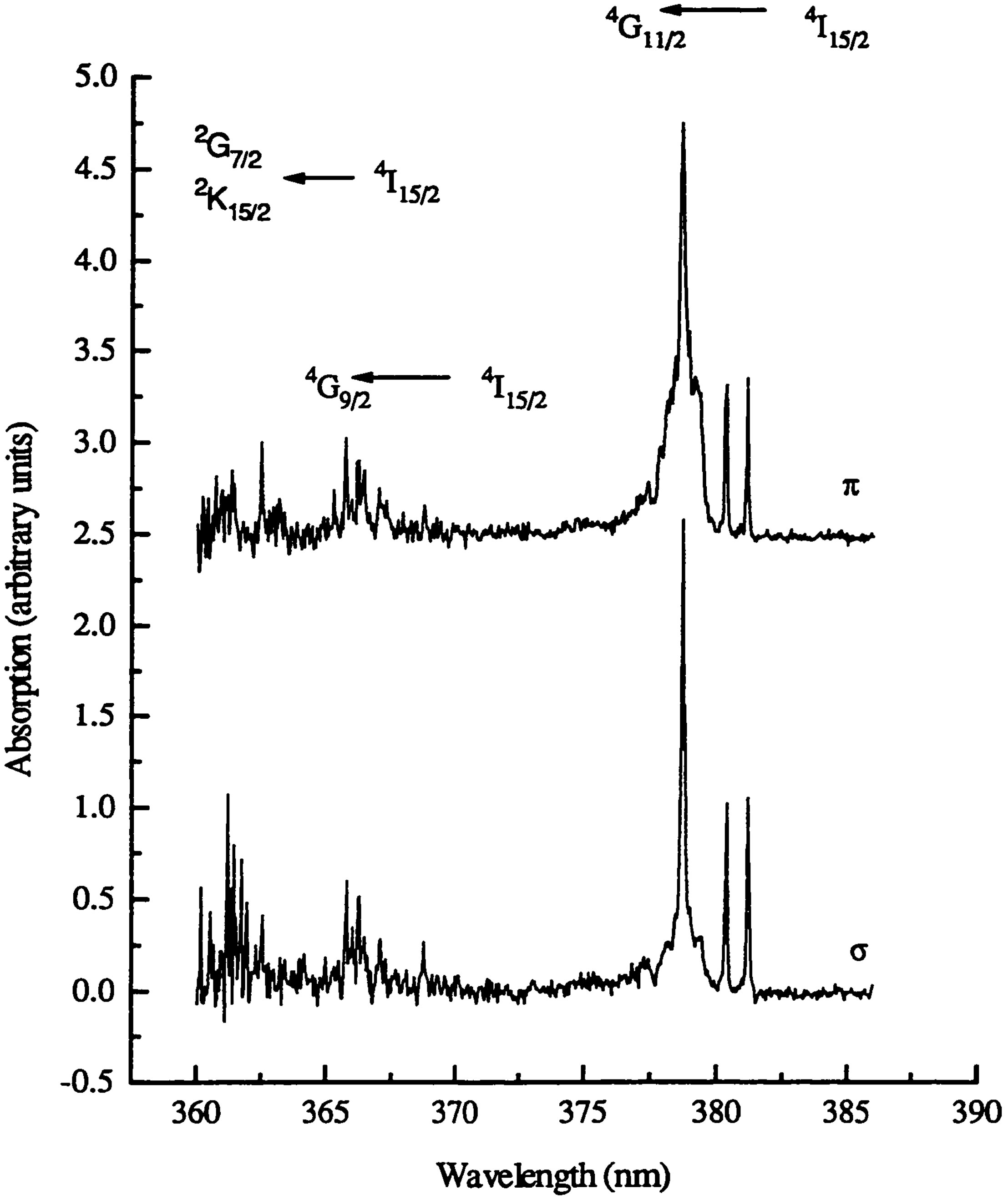

Figure 4.2.1.1 : Polarized absorption spectra of the transitions $^2G_{7/2}$, $^2K_{15/2}$, $^4G_{9/2}$, $^4G_{11/2} \leftarrow {}^4I_{15/2}$ at 7K for the 2.5% Er^{3+} doped YVO_4 crystal

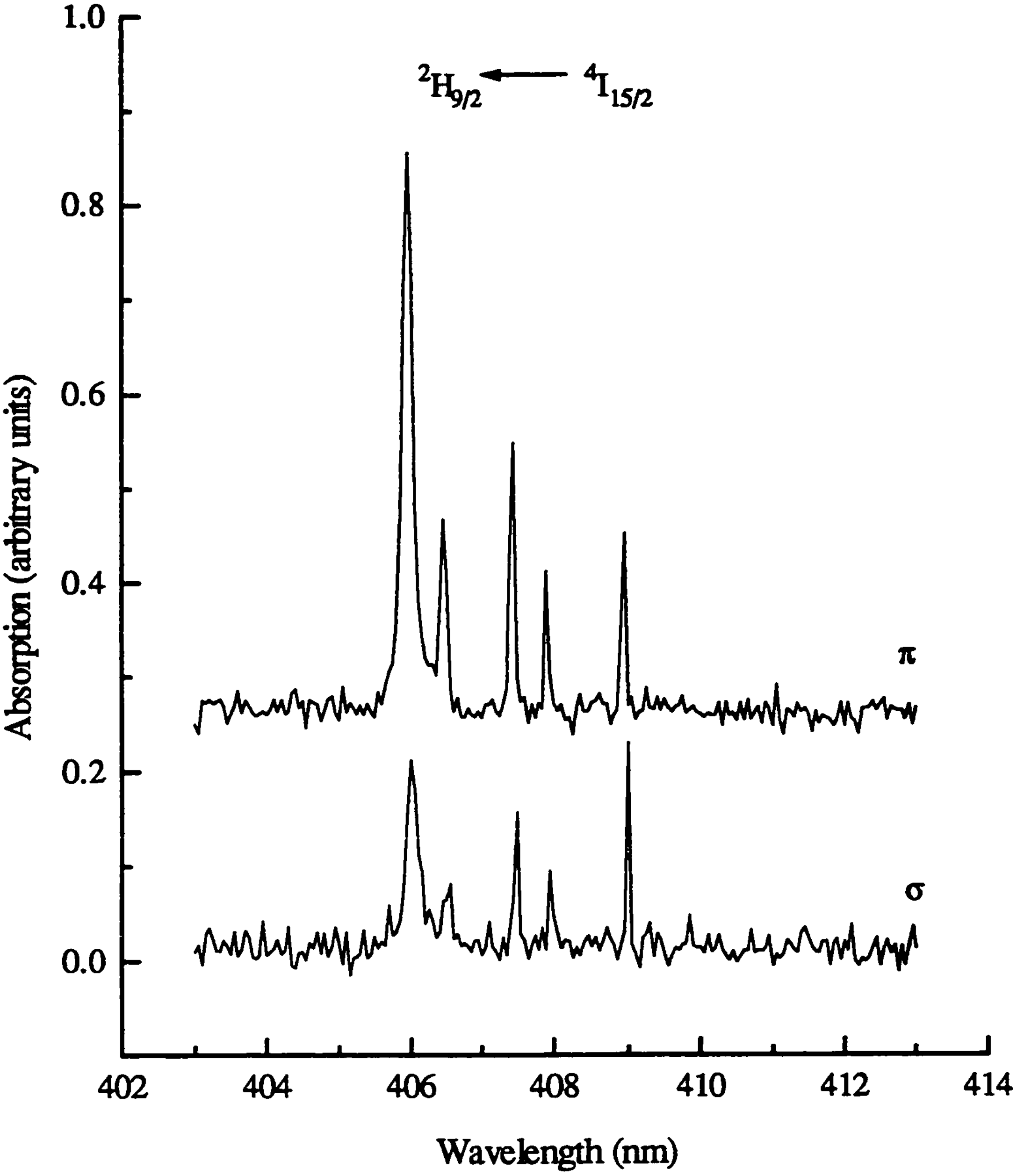

Figure 4.2.1.2 : Polarized absorption spectra of the transition $^2H_{9/2} \leftarrow {}^4I_{15/2}$ at 7K for the 2.5% Er^{3+} doped YVO_4 crystal

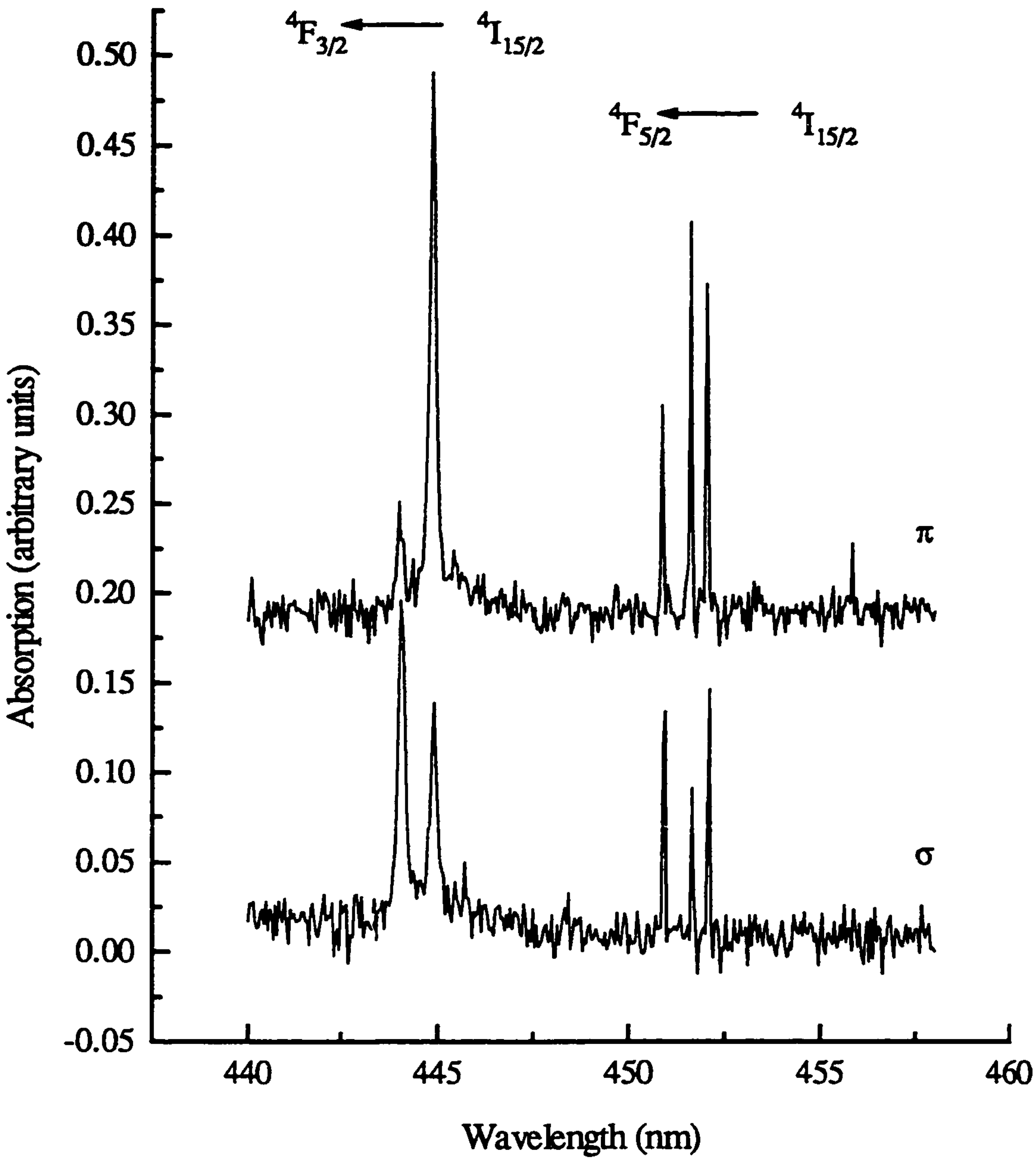

Figure 4.2.1.3 : Polarized absorption spectra of the transitions $^4F_{3/2}$, $^4F_{5/2} \leftarrow {}^4I_{15/2}$ at 7K for the 2.5% Er^{3+} doped YVO_4 crystal

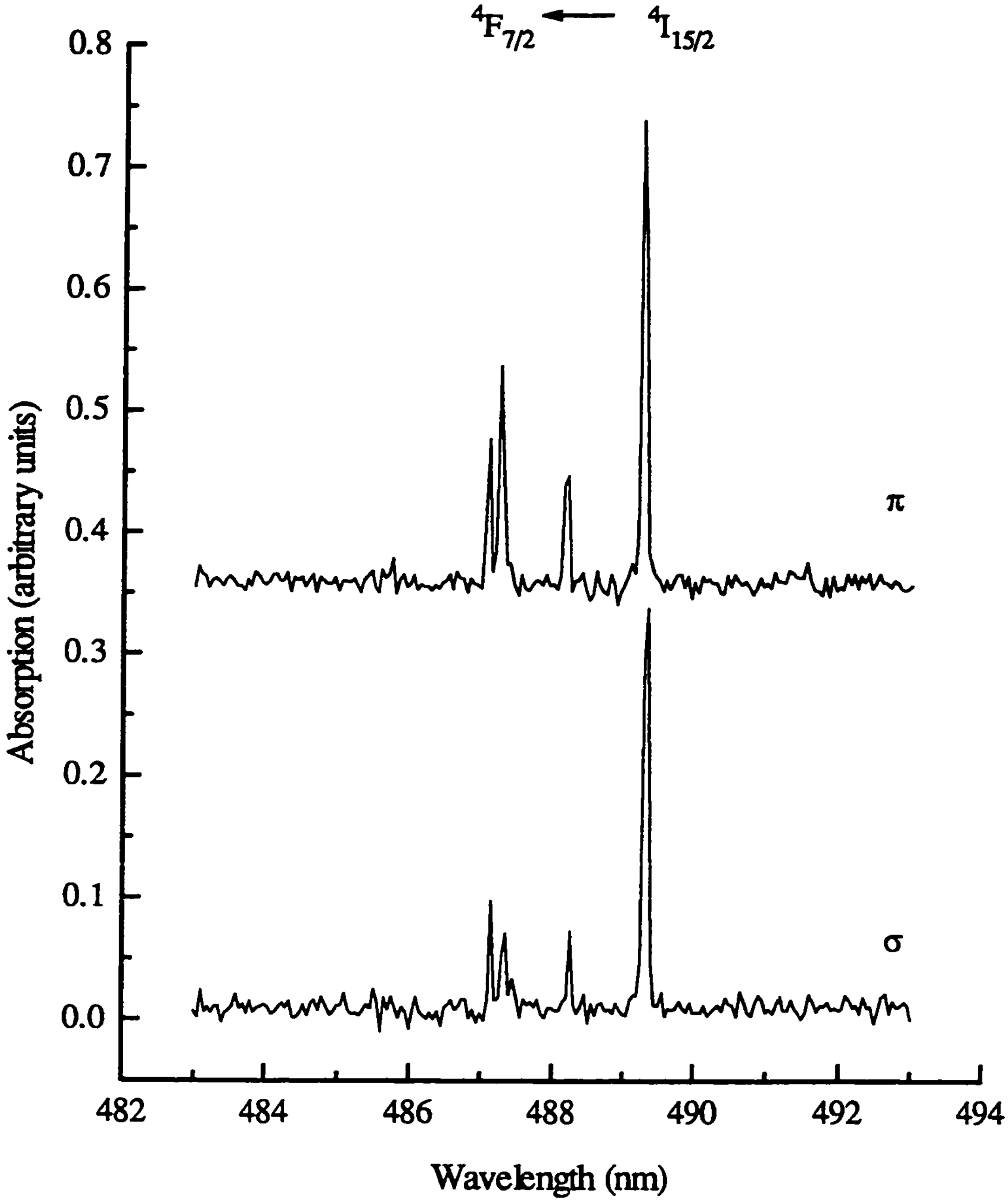

Figure 4.2.1.4 : Polarized absorption spectra of the transition $^4F_{7/2} \leftarrow {}^4I_{15/2}$ at 7K for the 2.5% Er^{3+} doped YVO_4 crystal

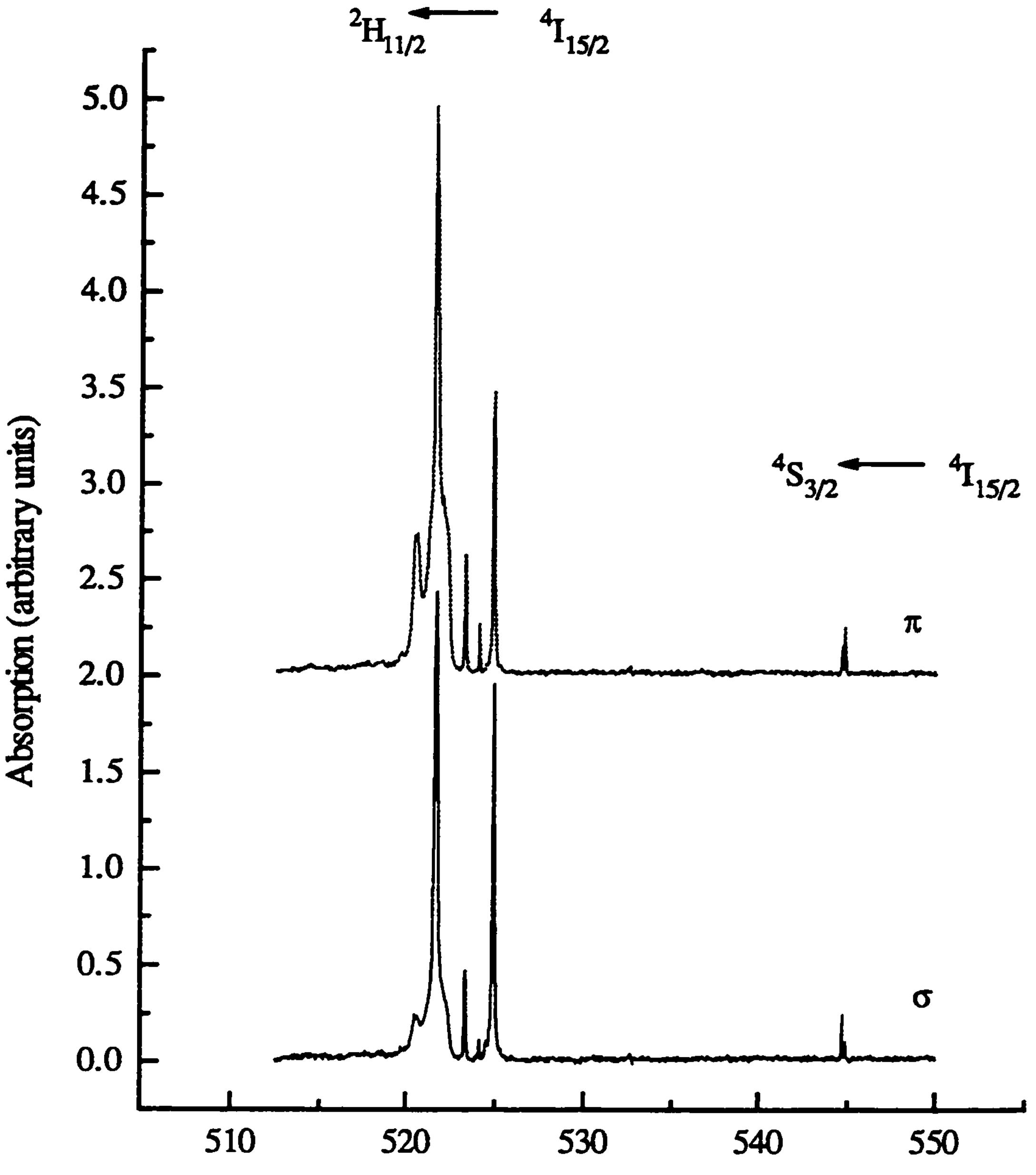

Figure 4.2.1.5 : Polarized absorption spectra of the transitions $^2H_{11/2}$, $^4S_{3/2} \leftarrow {}^4I_{15/2}$ at 7K for the 2.5% Er^{3+} doped YVO_4 crystal

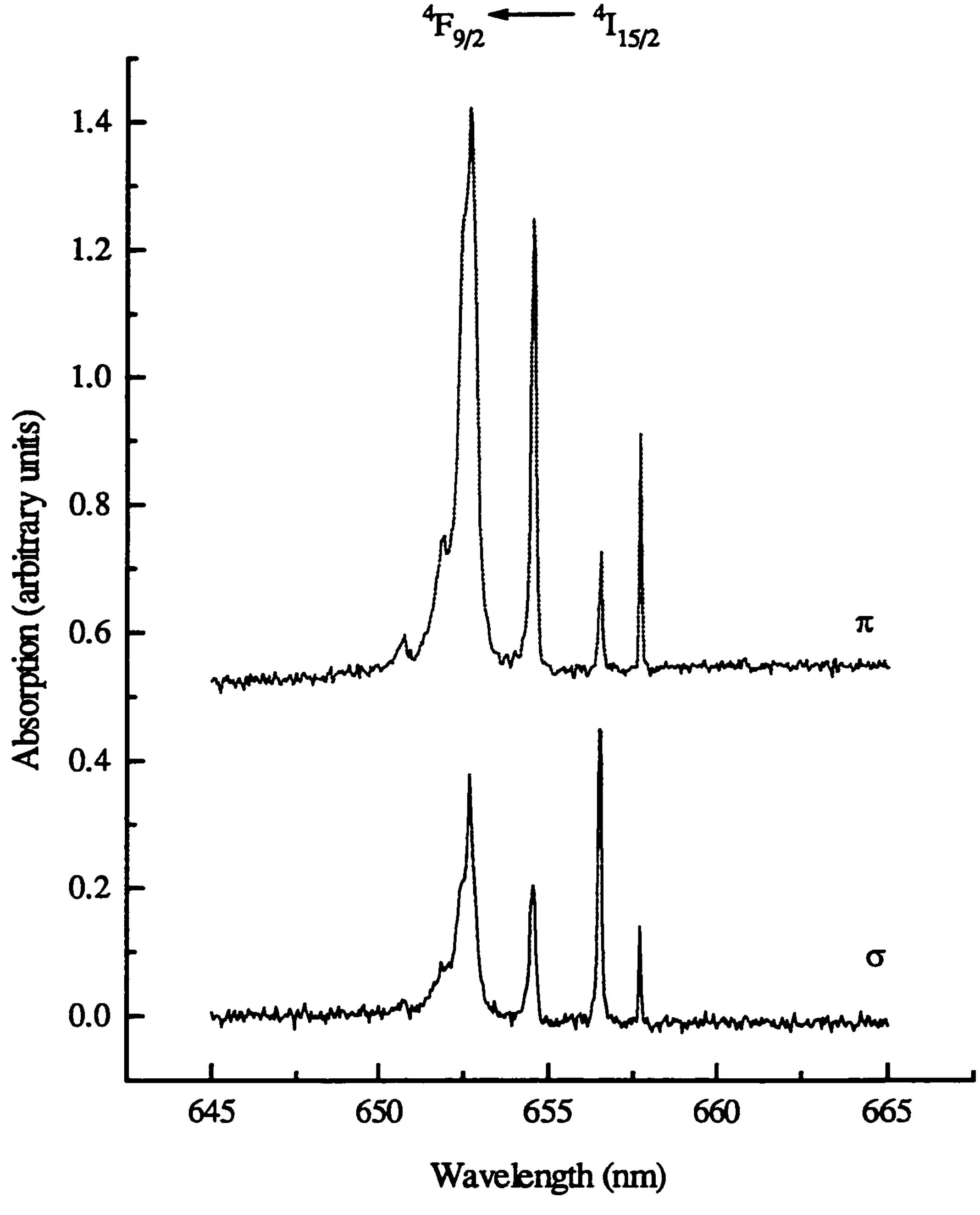

Figure 4.2.1.6 : Polarized absorption spectra of the transition $^4F_{9/2} \leftarrow {^4I_{15/2}}$ at 7K for the 2.5% Er^{3+} doped YVO_4 crystal

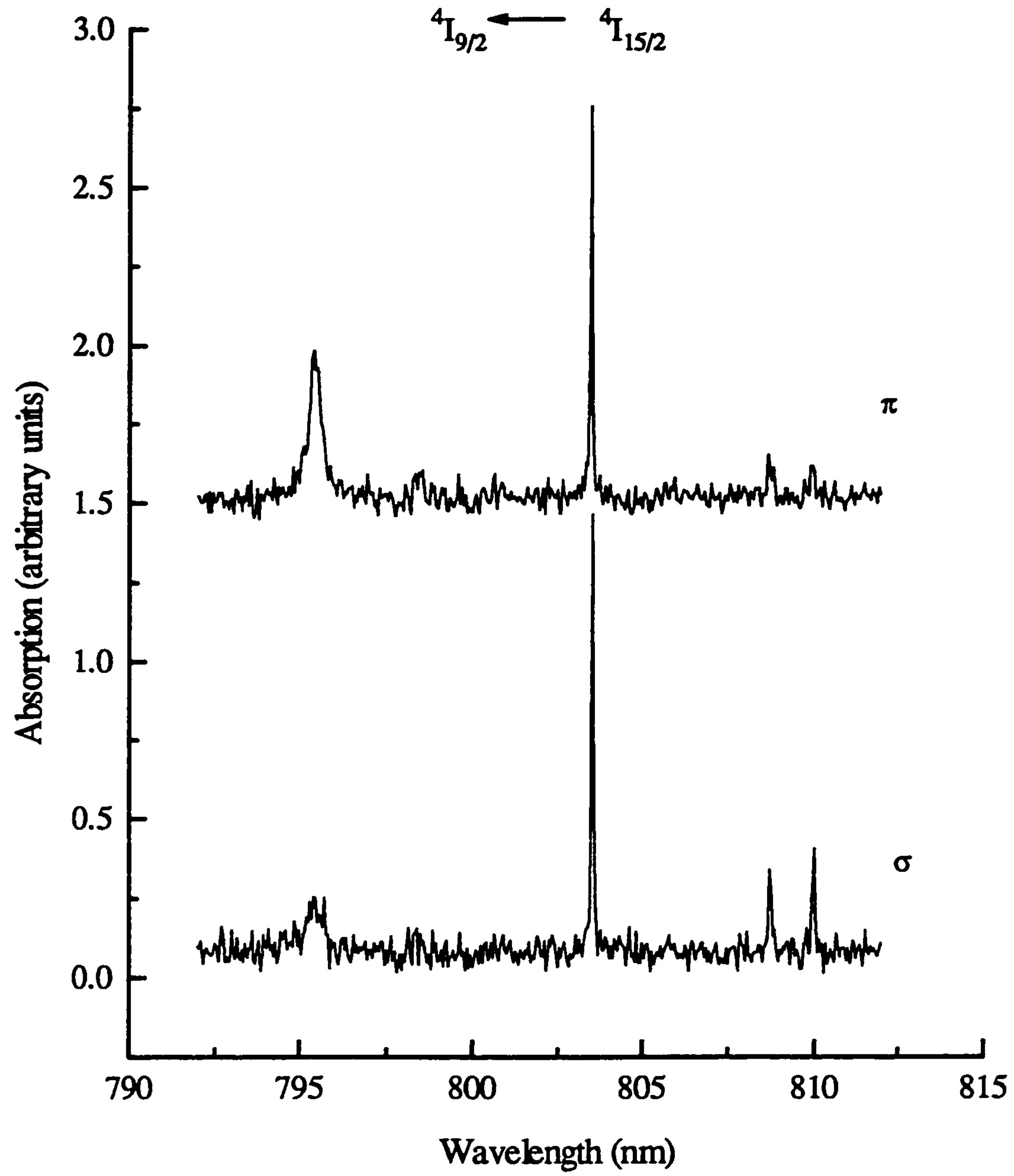

Figure 4.2.1.7 : Polarized absorption spectra of the transition $^4I_{9/2} \leftarrow {}^4I_{15/2}$ at 7K for the 2.5% Er^{3+} doped YVO_4 crystal

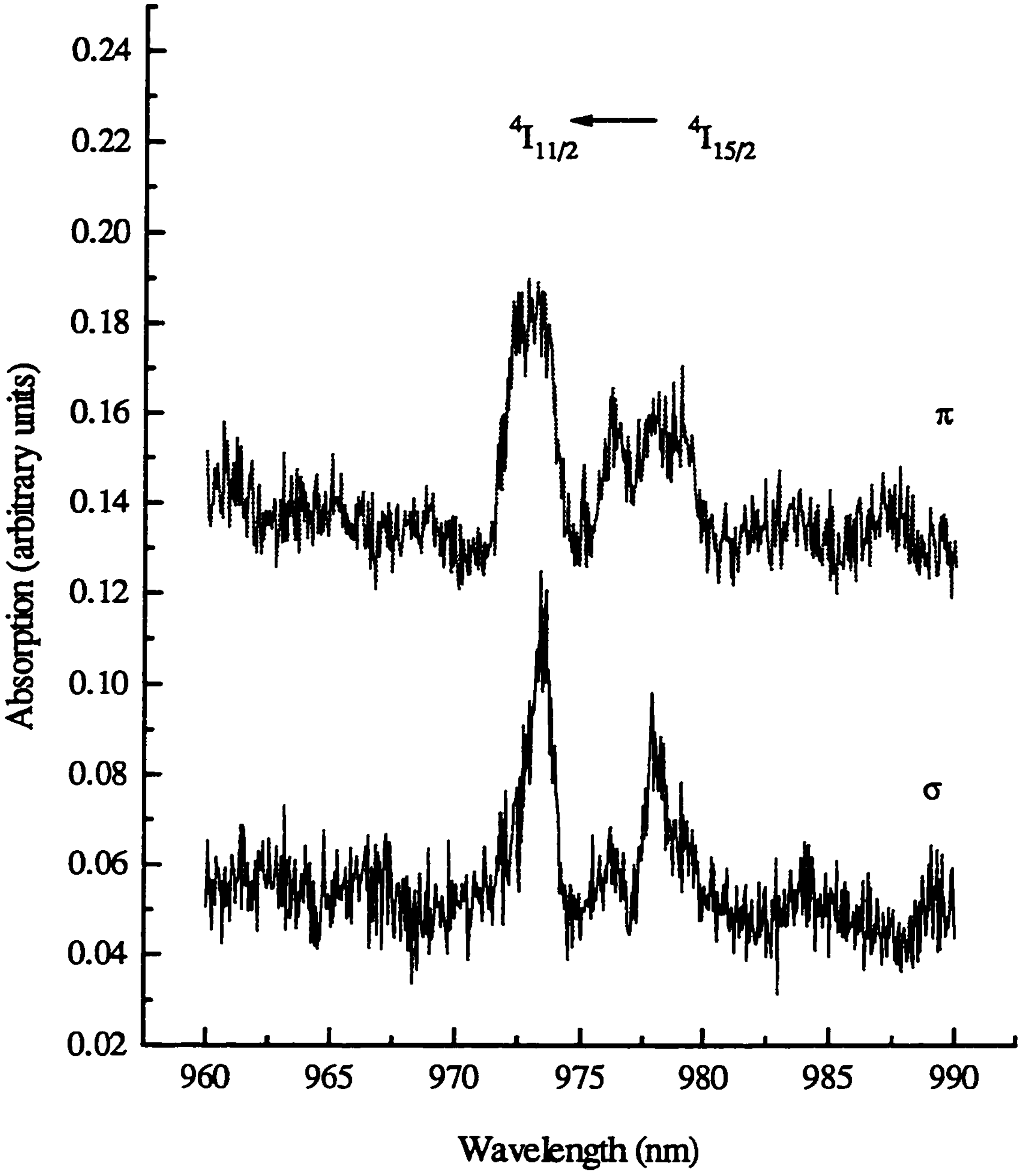

Figure 4.2.1.8 : Polarized absorption spectra of the transition $^4I_{11/2} \leftarrow {}^4I_{15/2}$ at 7K for the 2.5% Er^{3+} doped YVO_4 crystal

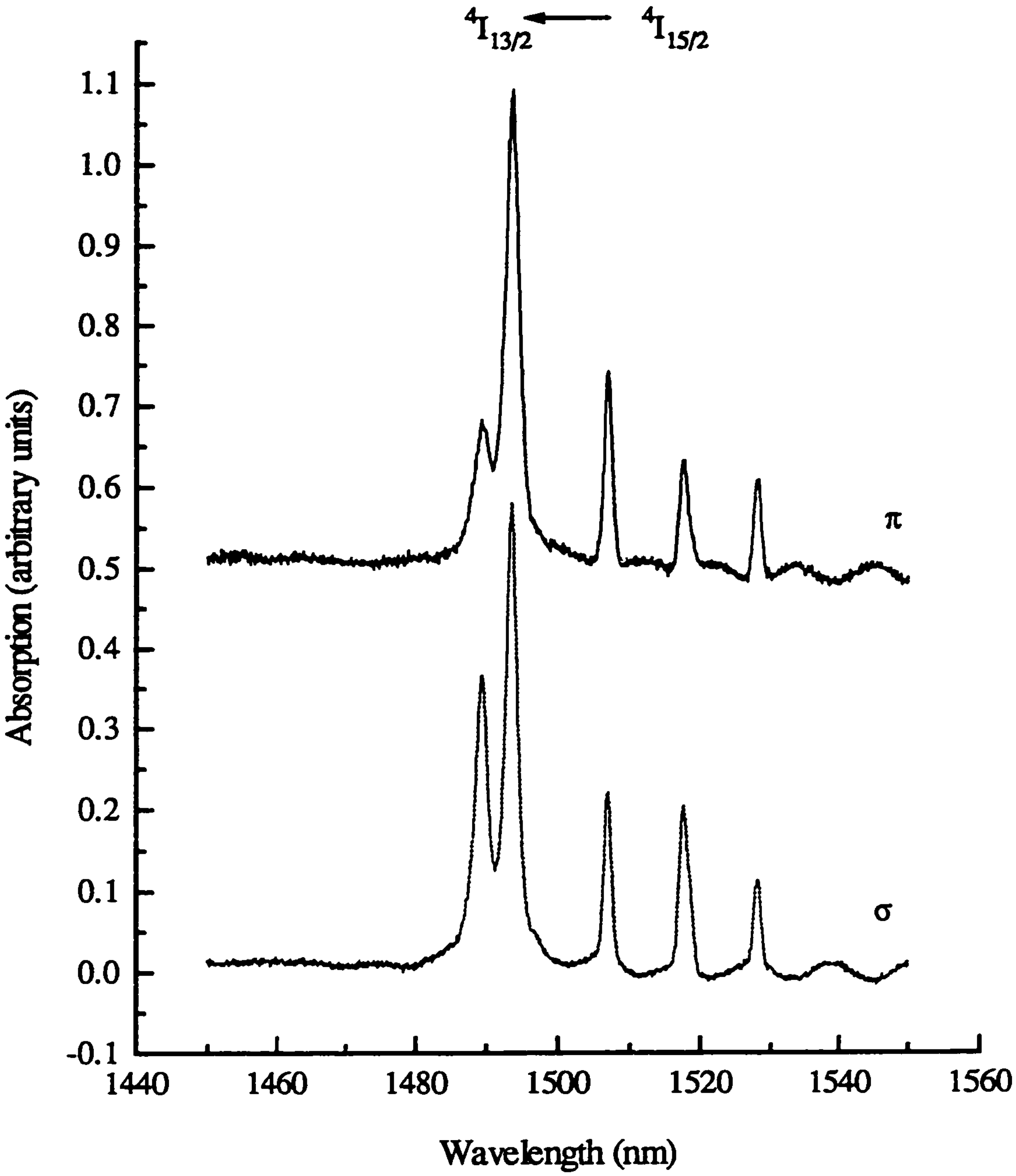

Figure 4.2.1.9 : Polarized absorption spectra of the transition $^4I_{13/2} \leftarrow {}^4I_{15/2}$ at 7K for the 2.5% Er^{3+} doped YVO_4 crystal

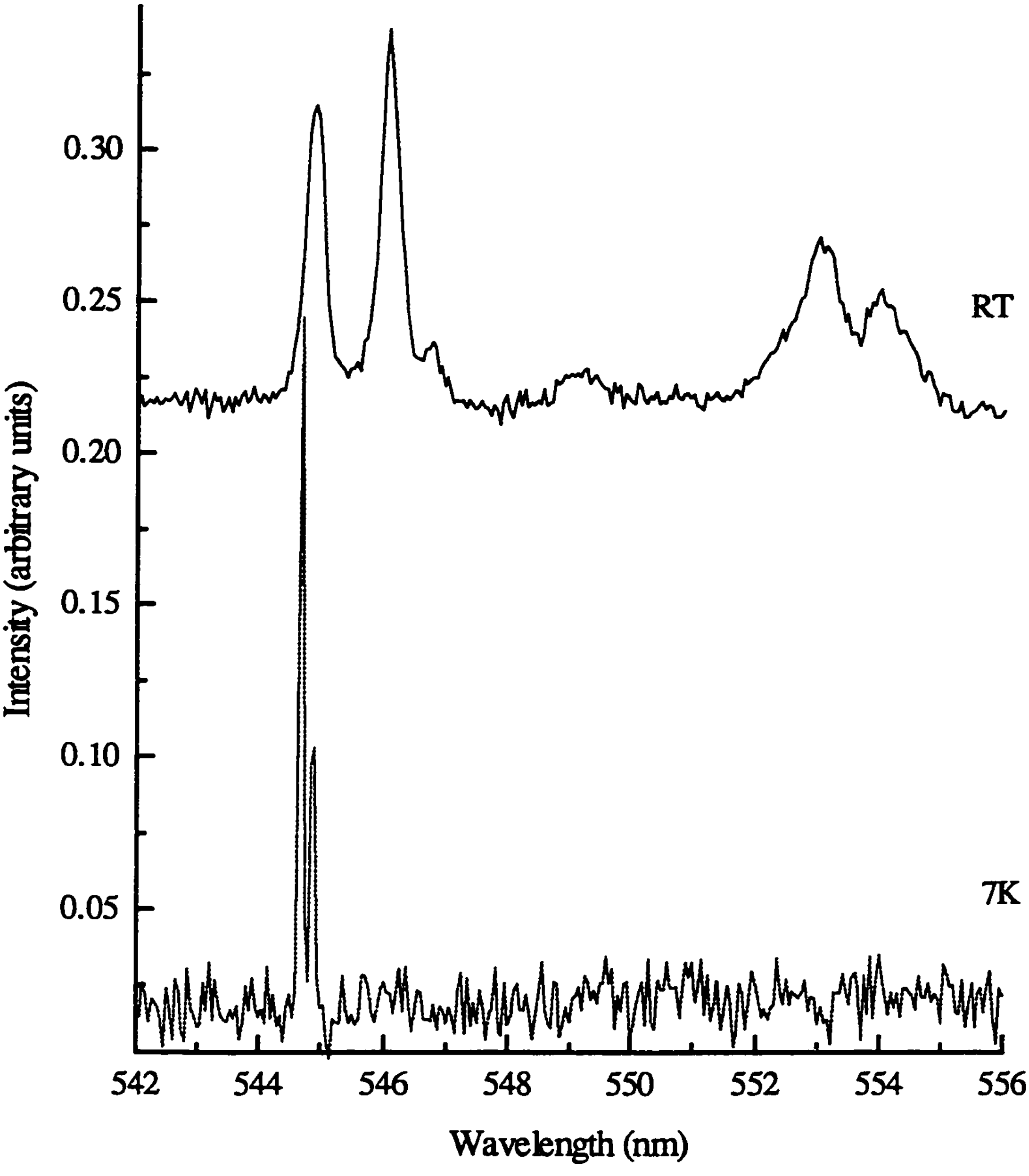

Figure 4.2.1.10 : Absorption spectra of the transition $^4S_{3/2} \leftarrow {}^4I_{15/2}$ at 7K and RT for the 2.5% Er^{3+} doped YVO_4 crystal

be assigned to the transitions Γ_7 ($^4S_{3/2}$) ← Γ_7 ($^4I_{15/2}$) and Γ_6 ($^4S_{3/2}$) ← Γ_7 ($^4I_{15/2}$) (Figure 4.2.1.11). Both transitions occur from the lowest Stark level of the ground state to the two excited Stark levels of the $^4S_{3/2}$ state. The splitting between the $^4S_{3/2}$ levels is 5 cm^{-1}. This also confirms that the Er^{3+} ions occupy only one type of environment since we have previously shown that in D_{2d} symmetry the $^4S_{3/2}$ state can only split into two levels. In Figure 4.2.1.10 the absorption spectrum at 300K shows more than four major peaks. These peaks obviously show broadening due to temperature and the number of peaks is due to transitions from the higher Stark levels of the $^4I_{15/2}$ state.

Fig 4.2.1.12 shows the observed energy levels with their corresponding Bethe symbols.

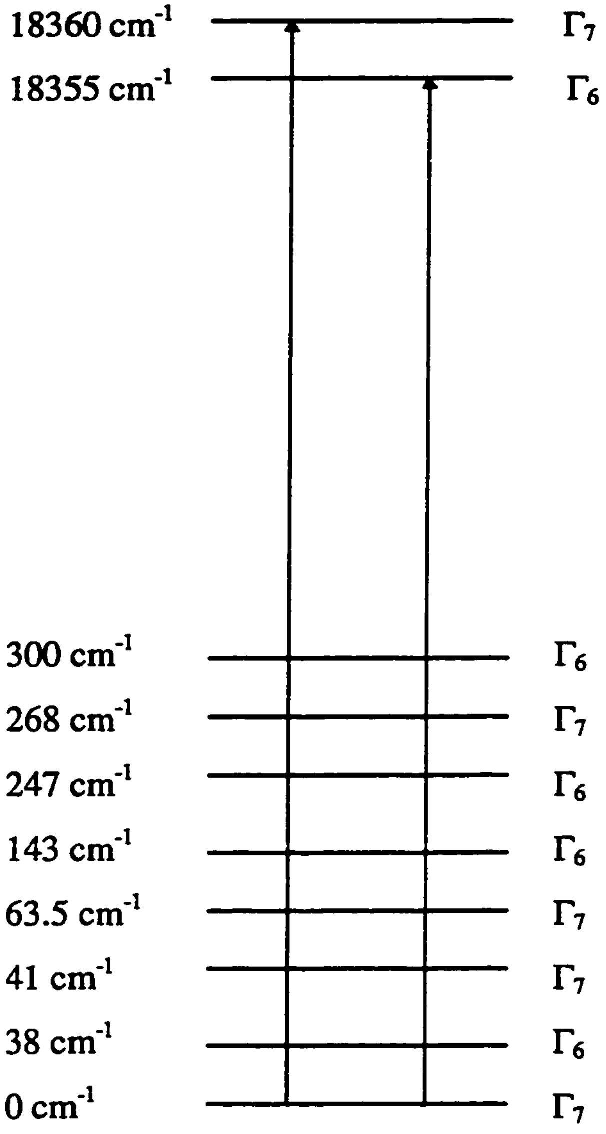

Figure 4.2.1.11 : Transitions from the $^4I_{15/2}$ ground state to the $^4S_{3/2}$ excited state obtained at 8K.

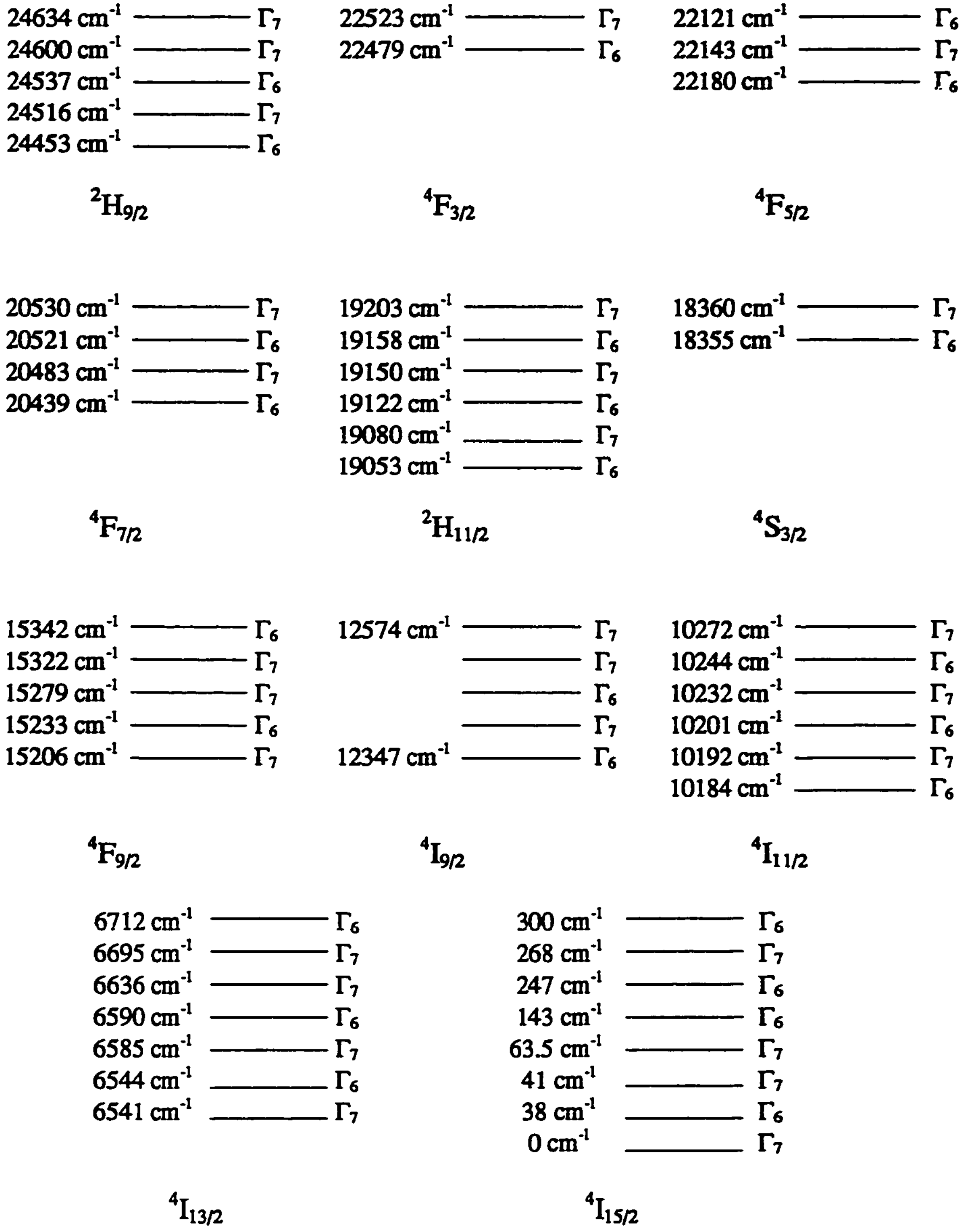

Figure 4.2.1.12: Observed Stark splittings of Er^{3+} doped yttrium vanadate crystals

4.2.2 Emission Spectroscopy

Room and low temperature (7K) fluorescence spectra (488 nm excitation) were recorded for all sample concentrations in the two polarizations and they showed similar features. Analysis of the spectra confirmed the Stark levels of the ground state, $^4I_{15/2}$ and excited state $^4I_{13/2}$ manifold. Bands were also observed in the 525, 580, 605, 660, 800 and 850 nm region of the spectrum and they can be attributed to the following transitions : $^2H_{11/2} \rightarrow {}^4I_{15/2}$, $^2H_{9/2} \rightarrow {}^4I_{13/2}$, $^4F_{5/2} \rightarrow {}^4I_{13/2}$, $^4F_{9/2} \rightarrow {}^4I_{15/2}$, $^4I_{9/2} \rightarrow {}^4I_{15/2}$, $^4S_{3/2} \rightarrow {}^4I_{13/2}$, respectively.

Figure 4.2.2.1 shows the low temperature (8K) polarized emission spectra for the transition $^4S_{3/2} \rightarrow {}^4I_{15/2}$. We note that for both polarizations thirteen peaks (different intensities) are observed at the following wavelengths: 544.7 nm (18360 cm^{-1}), 544.8 nm (18355 cm^{-1}), 545.9 nm (18319 cm^{-1}), 546.1 nm (18312 cm^{-1}), 546.6 nm (18296.5 cm^{-1}), 546.7 nm (18291.5 cm^{-1}), 548.9 nm (18217 cm^{-1}), 549.1 nm (18212 cm^{-1}), 552.2 nm (18108 cm^{-1}), 552.7 nm (18092 cm^{-1}), 552.9 (nm 18087 cm^{-1}), 553.7 nm (18060 cm^{-1}), 553.9 nm (18055 cm^{-1}).

Based on the selection rules for D_{2d} symmetry and the fact that emission generally occurs from the lowest Stark level of the excited state a total of eight peaks (transitions) are predicted to occur. However, the splitting of the $^4S_{3/2}$ state is

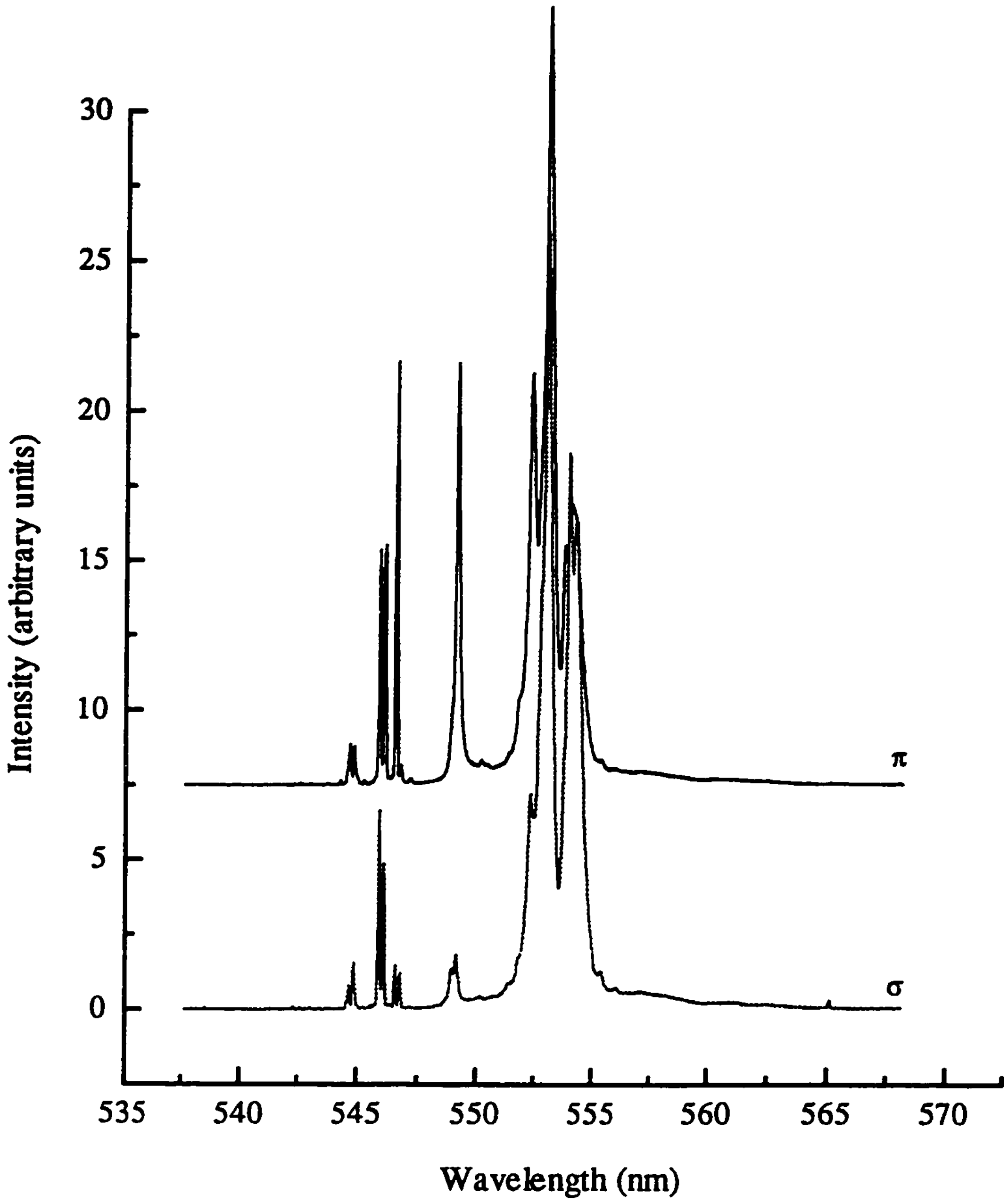

Figure 4.2.2.1 : Low temperature (8K) polarized emission spectra for the transition $^4S_{3/2} \rightarrow {}^4I_{15/2}$, $\lambda_{ex} = 488$ nm

approximately 5 cm^{-1} and thermalization of the upper level (Γ_7) is possible at 8K (1 cm^{-1} = 1.439 K). This leads to emission from both the Γ_7 and Γ_6 states (Figure 4.2.2.2)

Theoretically a total of sixteen peaks are predicted for the transition $^4S_{3/2} \rightarrow {}^4I_{15/2}$, for a single crystal field site. The observation of thirteen peaks clearly indicates a certain degree of overlap and confirms the fact that the Er^{3+} ions are found in only one type of environment.

Polarized emission spectra of the $^4S_{3/2} \rightarrow {}^4I_{13/2}$ transition were recorded at 7K and are shown in Figure 4.2.2.3. Each spectrum shows fourteen peaks at the following wavelengths: 846.1 nm (11819 cm^{-1}), 846.3 nm (11816 cm^{-1}), 846.5 nm (11814 cm^{-1}), 846.7 nm (11811 cm^{-1}), 849.2 nm (11775 cm^{-1}), 849.5 nm (11770 cm^{-1}), 849.7 nm (11769 cm^{-1}), 850.0 nm (11765 cm^{-1}), 852.9 nm (11724 cm^{-1}), 853.3 nm (11719 cm^{-1}), 857.3 nm (11665 cm^{-1}), 857.6 nm (11660 cm^{-1}), 858.5 nm (11648 cm^{-1}), 858.9 nm (11643 cm^{-1}). In this case the fourteen peaks predicted theoretically were observed ($^4S_{3/2}$ (Γ_7 , Γ_6) $\rightarrow$ $^4I_{13/2}$ (Γ_6, Γ_7, Γ_6, Γ_6, Γ_7, Γ_7, Γ_6)). From the spectra (Fig 4.2.2.3) the energy splittings of the $^4I_{13/2}$ multiplet were determined. Fig 4.2.2.4 shows the energy splittings and the allowed transitions for the $^4S_{3/2} \rightarrow {}^4I_{13/2}$ transition.

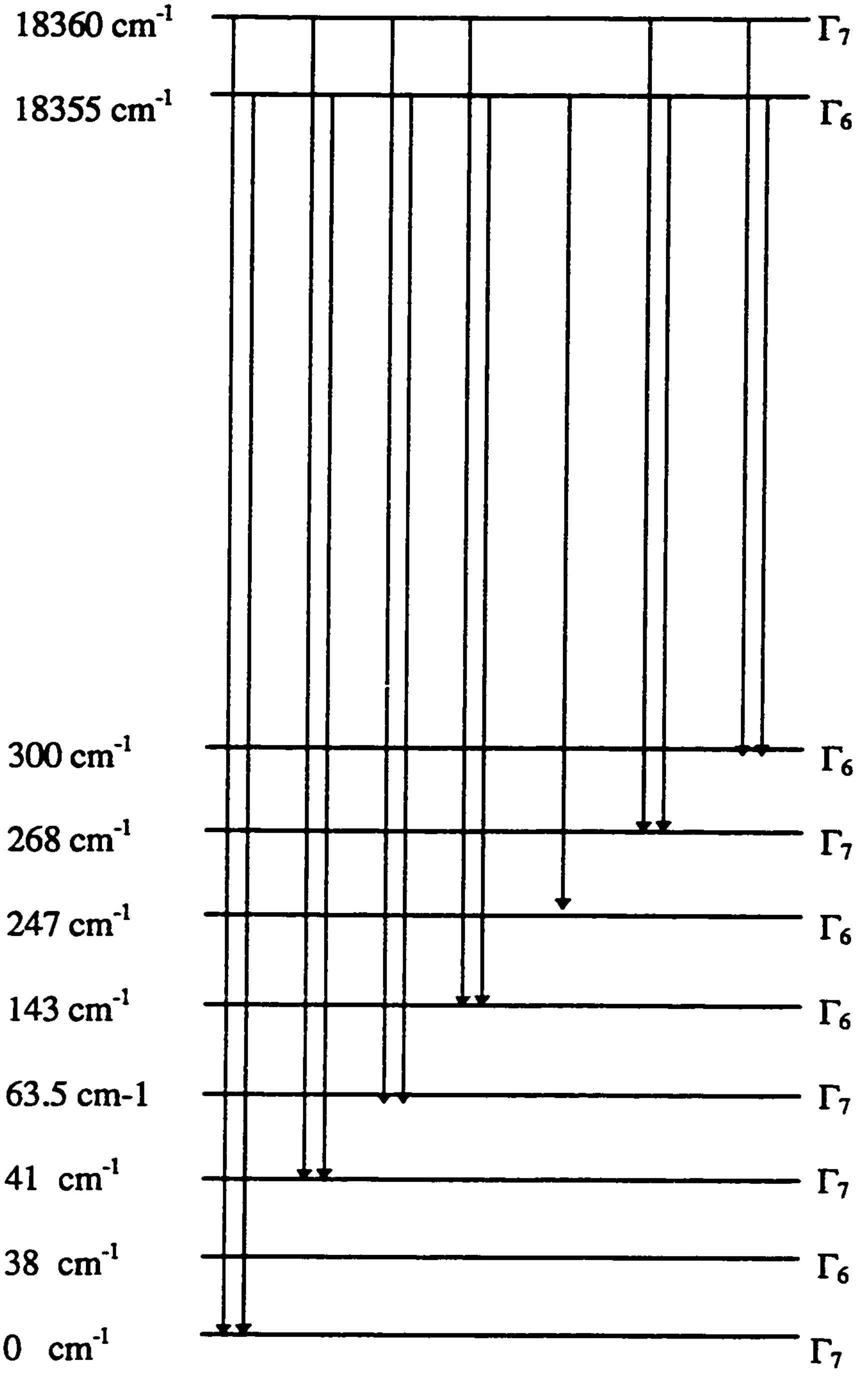

Figure 4.2.2.2 : Energy level splittings and the allowed transitions observed for the $^4S_{3/2} \rightarrow {}^4I_{15/2}$ transition at 8K, $\lambda_{Ex} = 488$ nm.

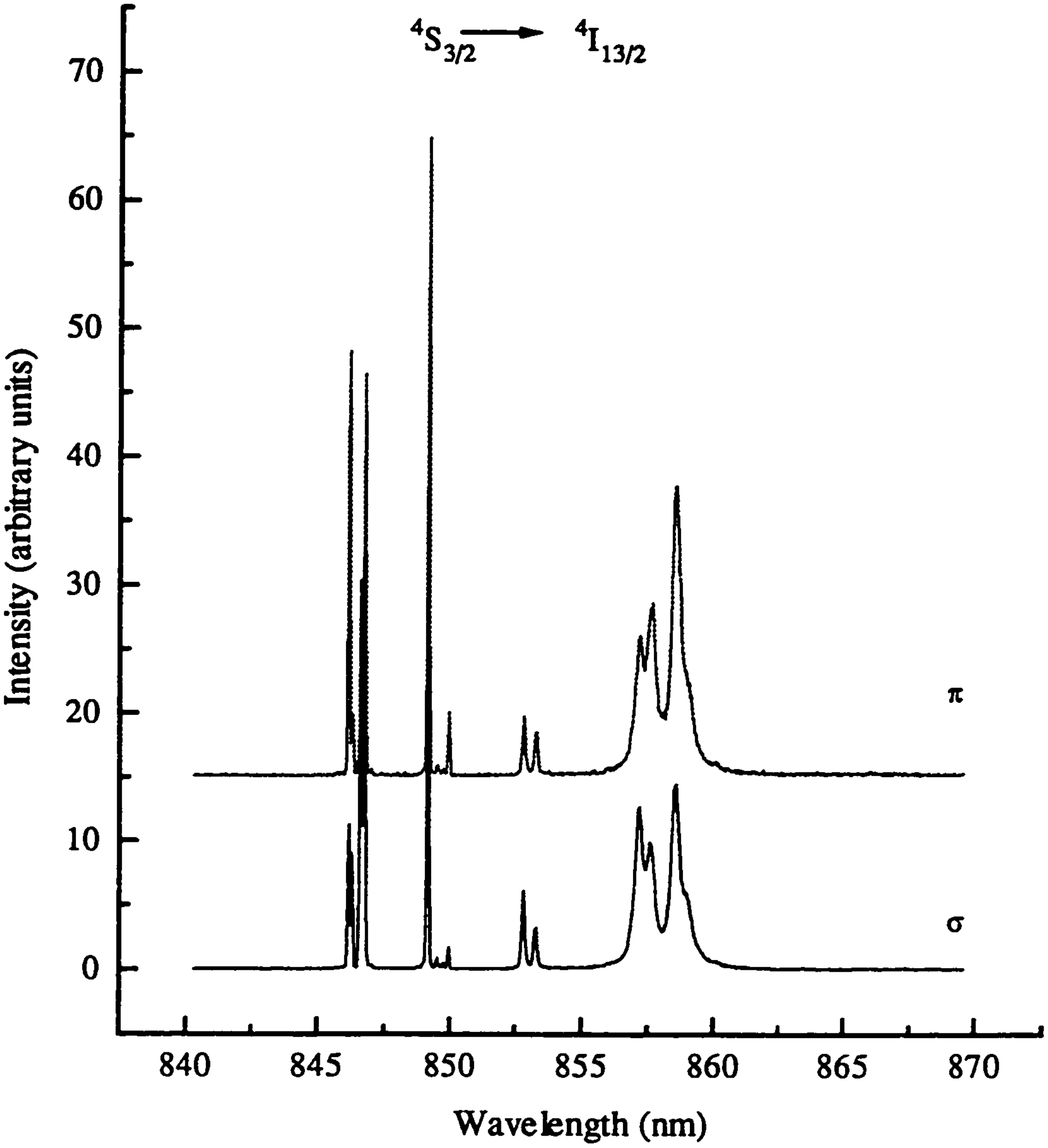

Figure 4.2.2.3 : Polarized emission spectra (8K) for the transition $S_{3/2} \rightarrow {}^4I_{13/2}$, $\lambda_{ex} = 488$ nm

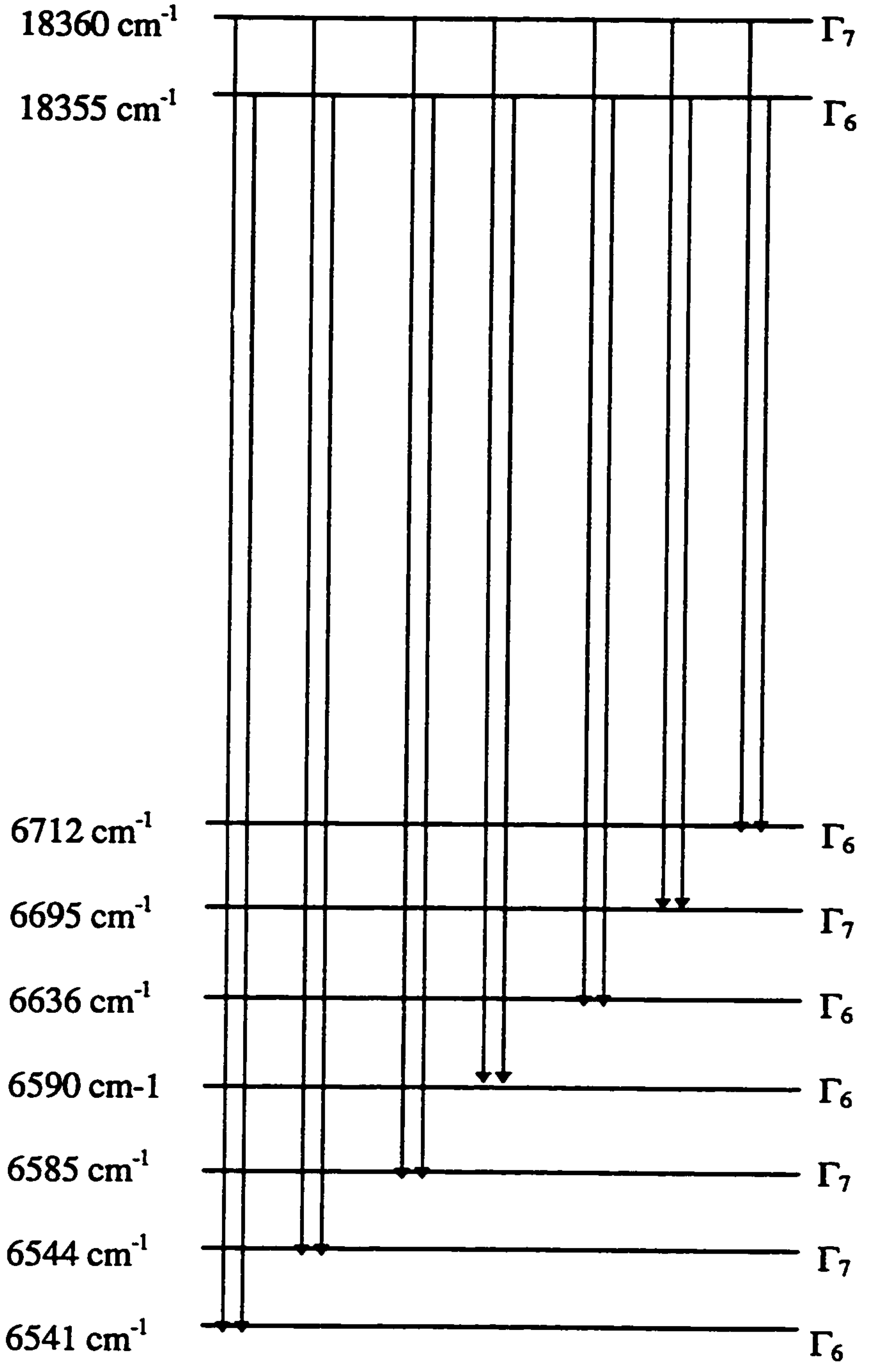

Figure 4.2.2.4 : Energy level splittings and the allowed transitions for the $^4S_{3/2} \rightarrow {}^4I_{13/2}$ transition at 8K, $\lambda_{Ex} = 488$ nm.

Transitions from the $^2H_{11/2}$ to the $^4I_{15/2}$ level are clearly visible at T > 77K. (Fig. 4.2.2.5). Thermalization of the $^2H_{11/2}$ level will be discussed in detail in section 4.5 .

Figures 4.2.2.6, 4.2.2.7 and 4.2.2.8 show the low temperature (77K) and room temperature emission spectra for the following transitions, $^2H_{9/2} \rightarrow {}^4I_{13/2}$, $^4F_{5/2} \rightarrow {}^4I_{13/2}$, $^4F_{9/2} \rightarrow {}^4I_{15/2}$ and $^4I_{9/2} \rightarrow {}^4I_{15/2}$. The main feature observed for these transitions is the marked decrease in intensity of the low temperature spectra. This is not unexpected considering that the excited states $^4F_{9/2}$ and $^4I_{9/2}$ are populated via radiative transitions from the higher excited states. The process is mediated by phonons. Considering that the highest frequency vibration of YVO_4 is 890 cm^{-1} [1] the energy gap $^4F_{7/2}$ - $^4F_{9/2}$ (5097 cm^{-1}) can be bridged by 6 phonons. The energy gap $^4F_{9/2}$ - $^4I_{9/2}$ (2632 cm^{-1}) can be bridged by 3 phonons.

In the infrared region of the spectrum the following transitions were observed : $^4I_{11/2} \rightarrow {}^4I_{15/2}$ (≈ 1.0 μm), $^2H_{9/2} \rightarrow {}^4F_{9/2}$ (≈ 1.07 μm), $^4F_{9/2} \rightarrow {}^4I_{13/2}$ (≈ 1.14 μm), $^4S_{3/2} \rightarrow {}^4I_{11/2}$ (≈ 1.25 μm), $^4G_{11/2} \rightarrow {}^2H_{11/2}$ (≈ 1.35 μm) and $^4I_{13/2} \rightarrow {}^4I_{15/2}$ (≈ 1.55 μm) (Fig. 4.2.2.9).

Fluorescence spectra were recorded for 0.1, 1, 2.5 and 10% Er^{3+} doped samples at low (T=7K) and room temperatures. The spectra were found to be

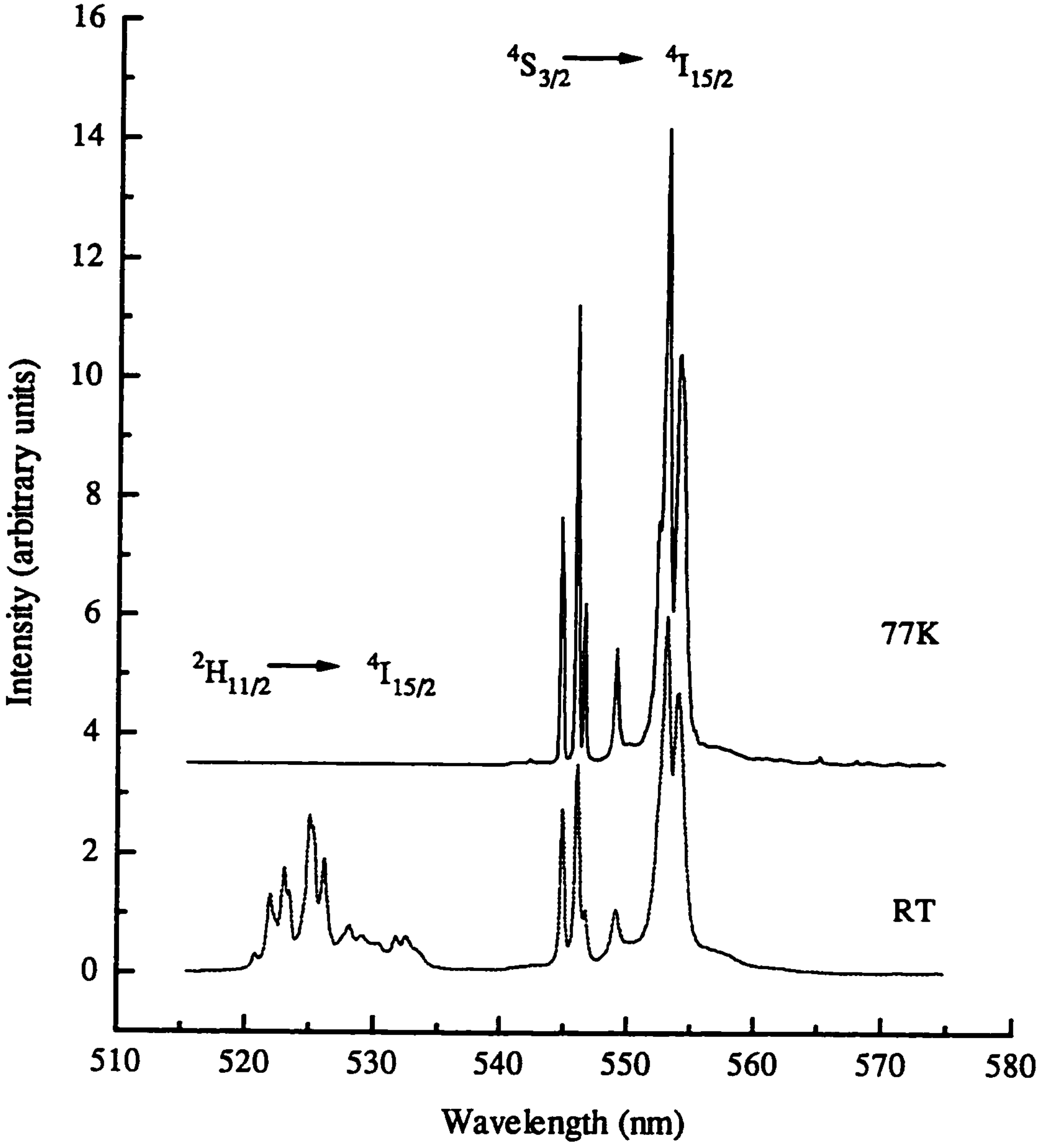

Figure 4.2.2.5 : Room and low temperature (77K) emission spectra for the transitions $^2H_{11/2}$, $^4S_{3/2} \rightarrow {}^4I_{15/2}$, $\lambda_{ex} = 488$ nm.

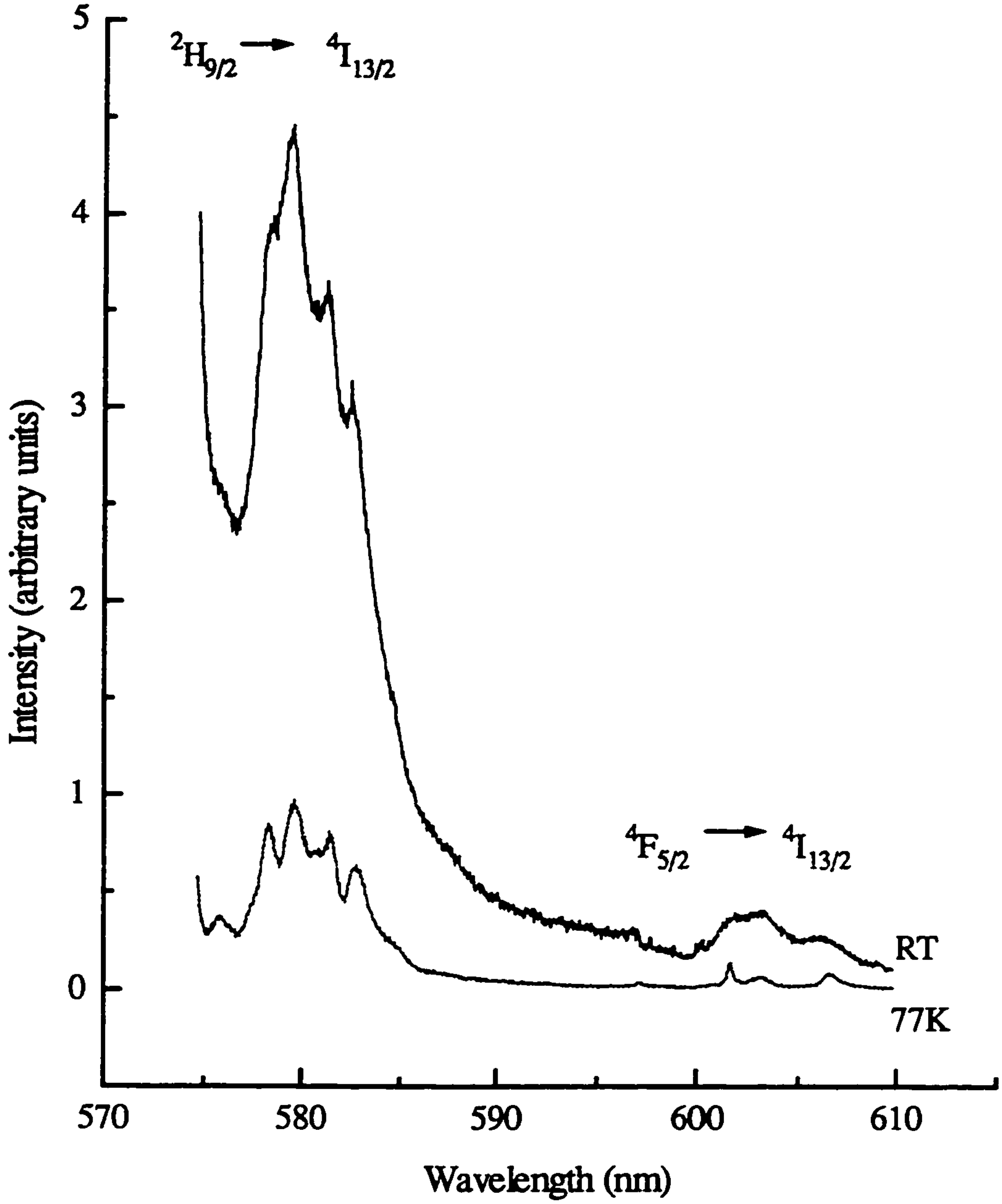

Figure 4.2.2.6 : Room and low temperature (77K) emission spectra for the transitions $^2H_{9/2}$, $^4F_{5/2} \rightarrow {}^4I_{13/2}$, $\lambda_{ex} = 488$ nm.

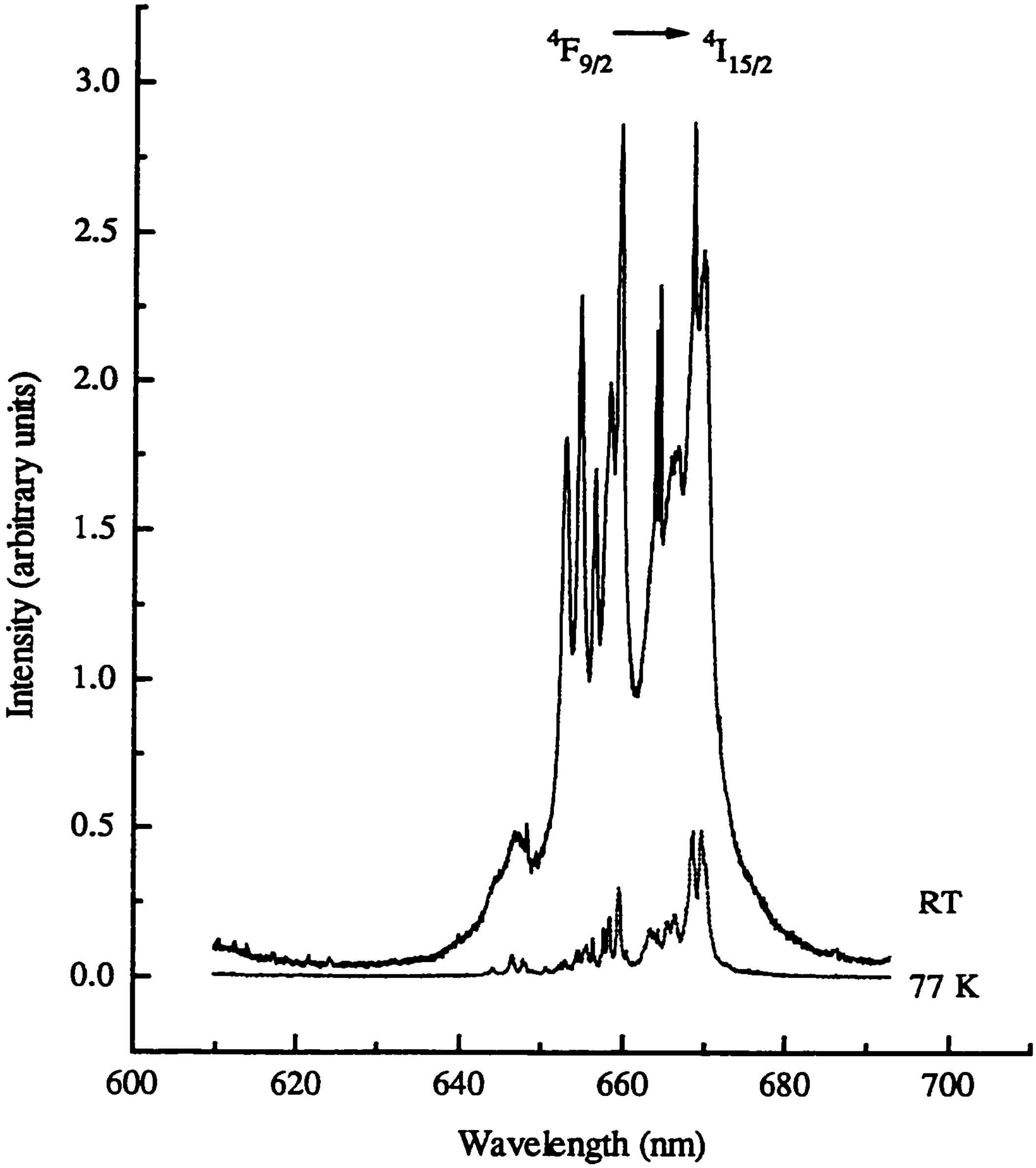

Figure 4.2.2.7 : Room and low temperature (77K) emission spectra for the transition $^4F_{9/2} \rightarrow {}^4I_{15/2}$, $\lambda_{ex} = 488$ nm.

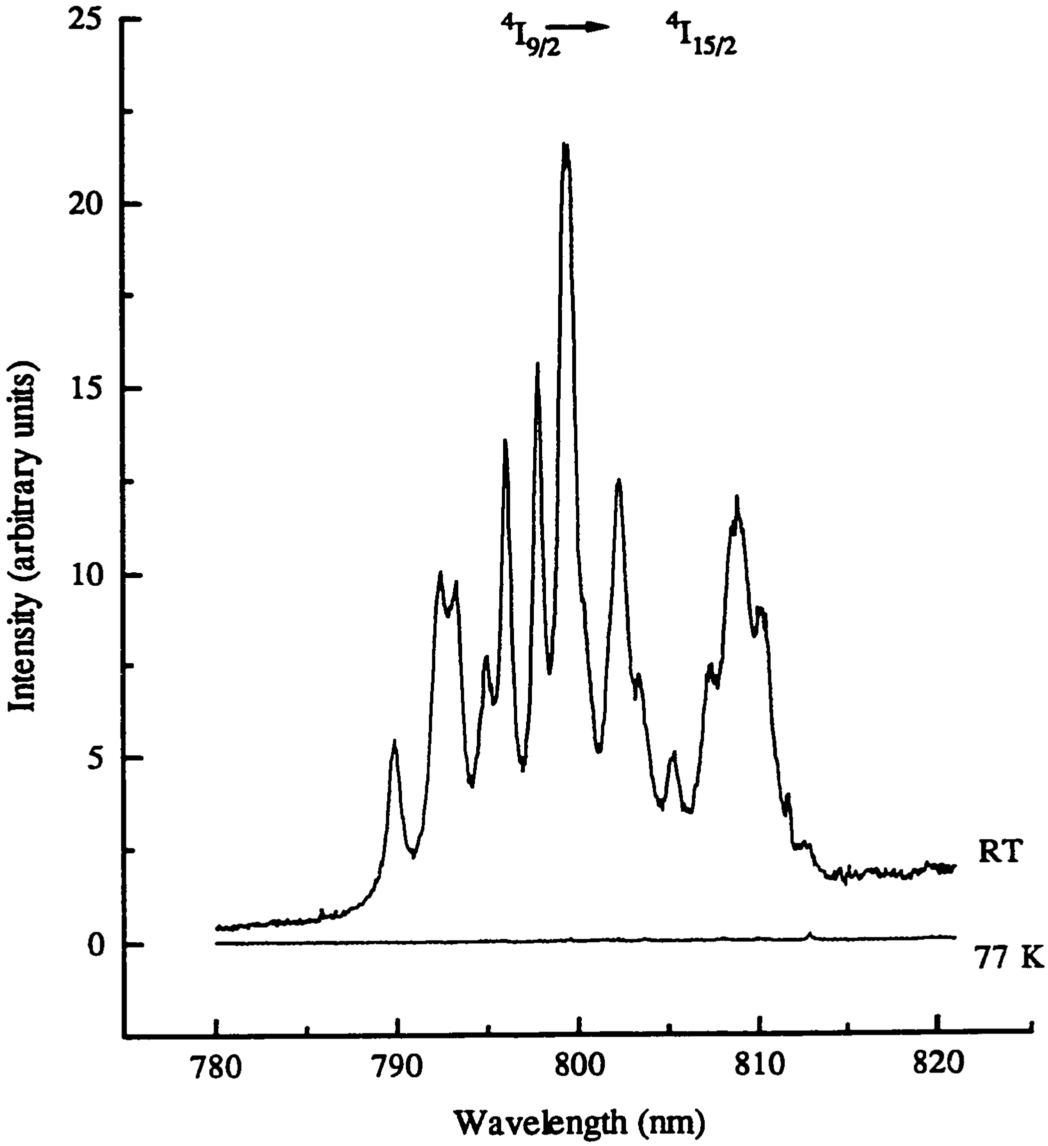

Figure 4.2.2.8 : Room and low temperature (77K) emission spectra for the transition $^4I_{9/2} \rightarrow {}^4I_{15/2}$, $\lambda_{ex} = 488$ nm.

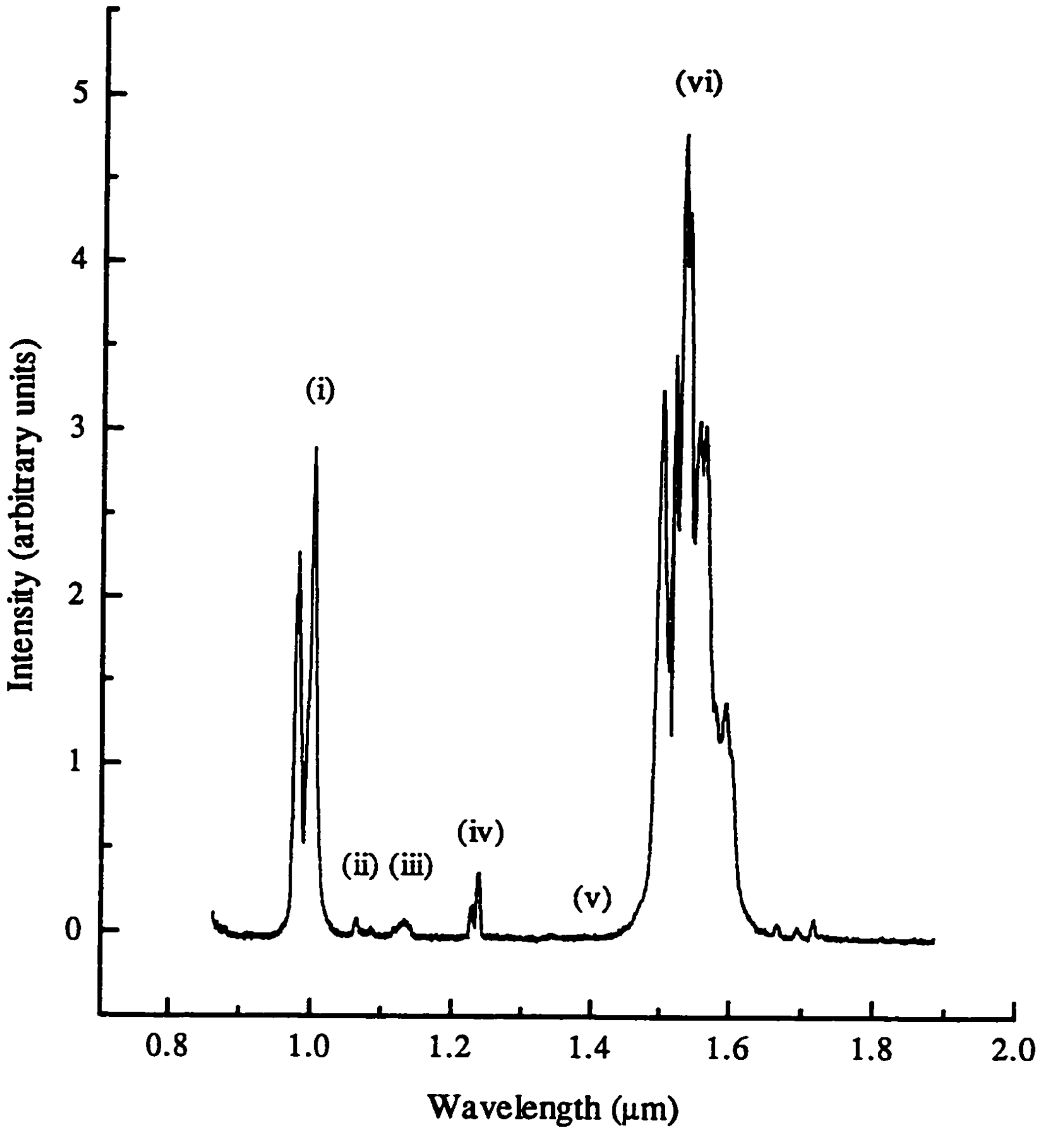

Figure 4.2.2.9 : Infrared emission upon 488 nm excitation at room temperature; i) $^4I_{11/2}\rightarrow^4I_{15/2}$, ii) $^2H_{9/2}\rightarrow^4F_{9/2}$, iii) $^4F_{9/2}\rightarrow^4I_{13/2}$, iv) $^4S_{3/2}\rightarrow^4I_{11/2}$, v) $^4G_{11/2}\rightarrow^2H_{11/2}$ and vi) $^4I_{13/2}\rightarrow^4I_{15/2}$.

similar and the fluorescence intensities were proportional to the Er^{3+} concentration up to 2.5% only, see Figure 4.2.2.10..

Figure 4.2.2.10 shows the room temperature green emission ($^2H_{11/2}$, $^4S_{3/2} \rightarrow$ $^4I_{15/2}$) of YVO_4 crystals doped with different concentrations of Er^{3+} upon 488 nm excitation. The fluorescence intensity was observed to increase with concentration and reached a maximum intensity in the 2.5% Er^{3+} doped crystal. The 10% Er^{3+} doped crystals showed much weaker fluorescence intensities in comparison to the other concentrations due to quenching.

The efficiency of Er^{3+} emission from the different manifolds depends on the multiphonon relaxation rates which in turn depends on the phonon energies of YVO_4. Raman spectroscopy has revealed the highest phonon energy to be 890 cm^{-1} [1]. This value is relatively large in comparison to other hosts. For example, the cut off phonon energies of Y_2O_3, CaF_2, and $CsCdBr_3$ are 560 [2], 465 [3], and 163 [4] cm^{-1}, respectively.

Emission from the $^4F_{7/2}$ state reflects the consequence of these differences. The $^4F_{7/2} \rightarrow {}^2H_{11/2}$ energy gaps are 1365, 1103, 1185, 1211 cm^{-1} for YVO_4, Y_2O_3 [5], CaF_2 [6], and $CsCdBr_3$ [7], requiring at least two, two, three and eight

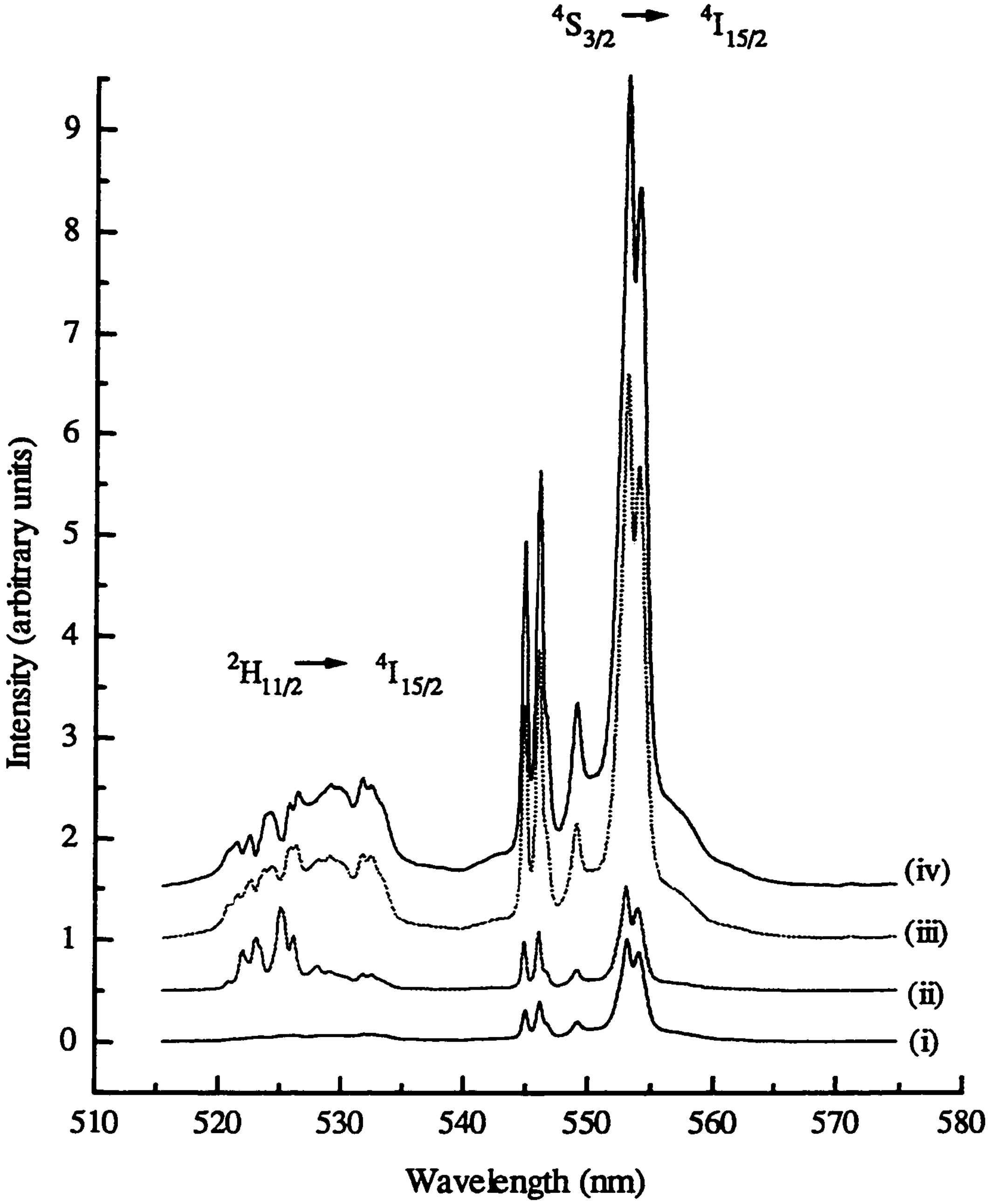

Figure 4.2.2.10 : Green emission of yttrium vanadate crystals, upon 488 nm excitation at room temperature, doped with different concentrations of Er^{3+}; i) 10 % , ii) 0.1% , iii) 1% , iv) 2.5%.

phonons, respectively, for multiphonon relaxation. Since the decay probability is generally found to be exponential in phonon number [8], the emission from the $^4F_{7/2}$ level is much more efficient in $CdCsBr_3$, while it is too weak to be detected in Y_2O_3 [9] and YVO_4.

4.3 JUDD-OFELT ANALYSIS

The intensities of the f-f transitions for Er^{3+} in YVO_4 have been treated using the approach of Judd-Ofelt. The environment of the Er^{3+} ion may be described by the three phenomenological parameters Ω_2, Ω_4 and Ω_6. These parameters are related to the symmetry of the site in which the Er^{3+} ions reside and to the degree of covalency of the Er^{3+}- O bond. To illustrate this, we show in Table 4.3.1 the values of Ω_t obtained in different hosts.

A noticeable difference is observed in the values of Ω_2 the most remarkable being the low value which has been reported for LaF_3 [10]. We also note that the values of the Ω_4 and Ω_6 vary to a lesser extent. Therefore, we may conclude that the Ω_2 parameter is influenced to a greater extent by the covalency of the Er^{3+}-ligand bond. In this section we will discuss the Judd-Ofelt parameters obtained for Er^{3+} in YVO_4 making use of the factors mentioned above.

The room temperature absorption spectra (discussed in section 4.2.1) allowed us to assign the transitions from the ground state, $^4I_{15/2}$, to the different excited states. The other parameters necessary to calculate the Judd-Ofelt parameters are the doubly reduced matrix elements, $\langle \| U^t \| \rangle$ (Table 4.3.2) which

Table 4.3.1 : Judd-Ofelt parameters Ω_t ($\times 10^{-20}$ cm^2) for some Er^{3+} doped laser crystals.

Compound	Site Symmetry	Ω_2	Ω_4	Ω_6
LaF_3 [10]	C_2	0.38	0.51	0.80
$Y_3Al_5O_{12}$ [11]	D_2	0.47	0.96	0.61
$CaYALO_4$ [12]	C_{4v}	3.78	2.52	1.91
Y_2SiO_5 [13]	C_1	2.84	1.42	0.82
Y_2O_3 [14]	C_2	4.6	1.2	0.48
$YAlO_3$ [15]	C_{1h}	1.06	2.63	0.78
YVO_4 (this work)	D_{2d}	13.45	2.23	1.67

Table 4.3.2: Doubly reduced matrix elements used in calculating the Judd-Ofelt parameters for Er^{3+} in YVO_4

$S'L'J'$	$[U^{(2)}]^2$	$[U^{(4)}]^2$	$[U^{(6)}]^2$
$^4I_{13/2}$	0.0195	0.1173	1.4299
$^4I_{11/2}$	0.0291	0.0004	0.3969
$^4I_{9/2}$	0	0.1856	0.0122
$^4F_{9/2}$	0	0.5275	0.4612
$^4S_{3/2}$	0	0	0.2230
$^2H_{11/2}$	0.7326	0.4222	0.0927
$^4F_{7/2}$	0	0.1467	0.6280
$^4F_{5/2}$	0	0	0.2237
$^4F_{3/2}$	0	0	0.1256
$^2H_{9/2}$	0	0.0157	0.2278

have been computed by Carnall et al [16] and are virtually constant irrespective of the ion environment and the measured line strength, S^{ed}_{meas}.

In practice the integrated absorption co-efficient, $\int\alpha(\lambda)d\lambda$, of an electronic dipole transition is related to the line strength, S, via the relation

$$\int\alpha(\lambda)d\lambda = \frac{8\pi^3e^2\bar{\lambda}\rho}{3ch(2J+1)}\frac{1}{n}\left[\frac{(n^2+2)^2}{9}\right]S^{\,ed}_{meas} \qquad 4.3.1$$

where $\alpha(\lambda)$ is the absorption co-efficient at wavelength λ, ρ is the concentration of Er^{3+} (ions/cm^3), $\bar{\lambda}$ is the mean wavelength of the absorption band, J is the total angular momentum of the initial level (for Er^{3+}, 15/2), n is the index of refraction and $(n^2+2)^2/9$ is the local field correction [17]. The experimental oscillator strength, f, was calculated using the following equation

$$f = \frac{2.303\,mc^2}{\pi e^2 n}\int\alpha(\lambda)d\lambda \qquad 4.3.2$$

In order to do the calculations, the integrated absorption co-efficients had to be determined from the absorption spectrum. This was done by converting the absorption spectrum such that the abscissa has units of frequency (s^{-1}) and the ordinate has units of absorption co-efficient (cm^{-1}), followed by the determination of the area under each absorption peak. The results of this calculation are presented in Table 4.3.3.

The Judd-Ofelt parameters may be calculated using the measured electric dipole line strength (equation 4.3.1) and solving the set of equations given by the following

$$S_{meas}^{ed} = \sum_{t=2,4,6} \Omega_t \left| \left\langle [S,L]\, J \middle\| U^{(t)} \middle\| [S',L']\, J' \right\rangle \right|^2 \qquad 4.3.3$$

The Judd-Ofelt parameters were obtained by a multiple least squares fit between S_{meas}^{ed} and S_{calc}^{ed}. Table 4.3.4 reports the S_{meas}^{ed} and S_{calc}^{ed} for the absorption transitions and the Judd-Ofelt parameters.

The calculation for the Judd-Ofelt parameters as described above treats the Ω_t as phenomenological parameters obtained from the experimental oscillator strengths and the calculated reduced matrix elements. Since, an excellent set of reduced matrix elements is available (Carnall et al.) the values of the Ω_t parameters will depend on the accuracy of the experimental oscillator strengths

Table 4.3.3 : Observed and calculated oscillator strengths for Er^{3+} in YVO_4

S L J	λ (nm)	$f_{exp} \times 10^{-6}$	$f_{cal} \times 10^{-6}$
$^4I_{13/2} \leftarrow {}^4I_{15/2}$	1523	1.98	1.97
$^4I_{15/2} \leftarrow {}^4I_{15/2}$	985.2	1.01	1.06
$^4I_{9/2} \leftarrow {}^4I_{15/2}$	802.95	0.50	0.71
$^4F_{9/2} \leftarrow {}^4I_{15/2}$	657.03	3.65	3.55
$^4S_{3/2} \leftarrow {}^4I_{15/2}$	549.17	0.60	0.69
$^2H_{11/2} \leftarrow {}^4I_{15/2}$	524.68	20.4	20.40
$^4F_{7/2} \leftarrow {}^4I_{15/2}$	490.89	2.97	3.04
$^4F_{5/2} \leftarrow {}^4I_{15/2}$	453.63	1.04	0.83
$^4F_{3/2} \leftarrow {}^4I_{15/2}$	444.95	0.23	0.48
$^2H_{9/2} \leftarrow {}^4I_{15/2}$	408.95	1.11	1.06

Table 4.3.4 : Measured and calculated absorption line strengths for 2.5% Er^{3+} in YVO_4. Line strengths, S, in units of 10^{-20} cm^2. The Judd-Ofelt parameters, Ω_t, are also shown.

Transition	$\bar{\lambda}$ (nm)	S_{meas}^{ed}	S_{calc}^{ed}
$^4I_{13/2} \leftarrow {}^4I_{15/2}$	1523	1.914	1.908
$^4I_{11/2} \leftarrow {}^4I_{15/2}$	985.2	0.541	0.566
$^4I_{9/2} \leftarrow {}^4I_{15/2}$	802.95	0.181	0.257
$^4F_{9/2} \leftarrow {}^4I_{15/2}$	657.03	1.087	1.058
$^4S_{3/2} \leftarrow {}^4I_{15/2}$	549.17	0.060	0.068
$^2H_{11/2} \leftarrow {}^4I_{15/2}$	524.68	5.822	5.822
$^4F_{7/2} \leftarrow {}^4I_{15/2}$	490.89	0.529	0.541
$^4F_{5/2} \leftarrow {}^4I_{15/2}$	453.63	0.128	0.103
$^4F_{3/2} \leftarrow {}^4I_{15/2}$	444.95	0.019	0.038
$^2H_{9/2} \leftarrow {}^4I_{15/2}$	408.95	0.205	0.195

$\Omega_2 = 13.45 \times 10^{-20}$ cm^2 $\Omega_4 = 2.23 \times 10^{-20}$ cm^2 $\Omega_6 = 1.67 \times 10^{-20}$ cm^2

used to compute. The major sources of errors in determining the oscillator strengths are: i) accuracy of dopant concentration, ii) strength of the transition, iii) dopant site distribution, and iv) accuracy of the refractive index. Therefore, it is not surprising to find relatively large root mean square (rms) values, which is a measure of the quality of the fit, where the σ_{rms} deviation is given by:

$$\sigma_{rms} = \left[\frac{\text{sum of squared deviation}}{\text{number of transitions - number of fitted parameters}}\right]^{1/2} \qquad 4.3.4$$

The rms value for the line strength was calculated to be 1.59×10^{-7} which is considered very good for these types of calculations. In other hosts such as Y_2O_3 [14] and $YAlO_3$ [15] rms values of 0.5×10^{-6} and 0.35×10^{-6} respectively, have been calculated.

One should also keep in mind that the values of Ω_t obtained also depend to some extent upon the particular transition included in the data set. From equation 4.3.3 it can be seen that in the fitting procedure each Ω_t is weighted with the value of the reduced matrix element associated with it. From Table 4.3.2 we observe that, in general, a large number of transitions have relatively large values of $[U^{(6)}]^2$, less have large values of $[U^{(4)}]^2$ and a few have large values of $[U^{(2)}]^2$. This will undoubtedly give that Ω_6 is the best defined parameter and conversly Ω_2 the least [18].

From Table 4.3.3. we note that the transition $^2H_{11/2} \leftarrow {}^4I_{15/2}$ has the largest value for the oscillator strength. This transition is hypersensitive [19] and obeys the selection rules $|\Delta J| \leq 2$, $|\Delta L| \leq 2$ and $\Delta S = 0$. The intensity is particularly sensitive to the host, and is solely determined by the Ω_2 term. Jorgensen and Judd [19] noted that the selection rules for hypersensitive transitions were just the selection rules on $[U^{(2)}]^2$ and that hypersensitivity could be rationalized as the peculiar sensitivity of Ω_2 to the environment.

From Table 4.3.1 we observe that the Ω_t parameters vary substantially with the environment of the Er^{3+} ion. These variations are determined by the crystal field parameters A_{kq}, which in turn depend upon the positions and the charges of the surrounding ligands. The intensity of certain transitions might be intense in systems permitting a certain A_{kq} term, while weak for other systems excluding them. The values of the Ω_4 and Ω_6 parameters (Table 4.3.1) do not vary as much as those for Ω_2. It should be noted that the Ω_2 parameter is determined essentially by transitions to the $^4G_{11/2}$ and $^2H_{11/2}$ levels. The transition to the $^4G_{11/2}$ can not be measured accurately, since the corresponding absorption band is situated on the absorption edge of the yttrium vanadate matrix. The Ω_2 is related to the oscillator strength of the $^2H_{11/2} \leftarrow {}^4I_{15/2}$ transition which is substantially more intense in the YVO_4 crystal (see Table 4.3.3), showing that the YVO_4 matrix is less ionic in character [20].

The phenomenologically obtained Ω_2 parameters are a combination of static and vibronic perturbations. Both static and vibronic intensities can be increased if a significant amount of covalency is postulated. This covalency can modify the angular part of the 4f function which will preferentially affect Ω_2, and hence giving an Ω_2 parameter almost an order of magnitude larger in YVO_4 than the other hosts. The relatively small Ω_2 value for some of the hosts such as that of the LaF_3 system is believed to be attributable to the formal prohibition of the A_{10} crystal field term for the D_{3h} rare earth site symmetry. The A_{10} term is disallowed for the D_{2d} site of YVO_4 and a small Ω_2 value was expected. However, a large value for Ω_2 was found. This may be attributed to the inaccuracy in calculating the Ω_2 value as discussed in the above paragraph. We feel that the inaccuracy in the calculations cannot account for such a high value of Ω_2. A more likely explanation is that a strong covalent bond, exists between Er and oxygen. The relatively high values for Ω_4 and Ω_6 indicate that the YVO_4 is a hard crystal with a higher degree of disorder in comparison to other hosts (Table 4.3.1).

The probability for the spontaneous transition $A_{aa'}$ from a given state a to the state a′ is the sum of the electric-dipole and magnetic dipole transition probabilities $A^{ed}_{aa'}$ and $A^{md}_{aa'}$. $A^{ed}_{aa'}$ was calculated using the electric dipole operator F_e^2 and magnetic dipole operator M_n^2 given by equation 2.5.1.10 and 2.5.1.11, respectively, to give

$$A_{aa'} = \frac{32\pi^3\sigma^3}{3\eta(4\pi\varepsilon_0)} \left[\frac{n(n^2+2)^2}{9} F_e^2 + n^3 M_n^2 \right] \qquad (4.3.5)$$

where n = 2.02 [21] is the average refractive index over the σ and π polarizations for Er^{3+}:YVO_4 and σ (cm^{-1}). The data are summarized in Table 4.3.5 which also includes the values of the intramanifold branching ratio $\beta_{aa'}$ given by

$$\beta = \frac{A_{aa'}}{\sum_{a'} A_{aa'}} \qquad 4.3.6$$

where the sum represents the total transition probability for radiative decay from the initial manifold. The β values obtained for YVO_4:Er^{3+} compared well with those found for Er^{3+} in Y_2SiO_5 [13]. The radiative lifetime is given by:

Table 4.3.5 : Calculated spontaneous emission probability $A_{aa'}$, radiative branching ratios $\beta_{aa'}$, and radiative lifetimes of 2.5% Er^{3+} in YVO_4.

Transition	σ (cm^{-1})	A_{ed} (s^{-1})	A_{md} (s^{-1})	τ_{R_a} (ms)	$\beta_{aa'}$
$^4I_{13/2} \rightarrow {}^4I_{15/2}$	6550	353	82.6	2.3	1
$^4I_{11/2} \rightarrow {}^4I_{15/2}$	10121	536.6	0	1.62	0.87
$^4I_{13/2}$	3571	60.7	16.6		0.13
$^4I_{9/2} \rightarrow {}^4I_{15/2}$	12453	427	0	1.71	0.73
$^4I_{13/2}$	5903	150	0		0.26
$^4I_{11/2}$	2331	3.3	2.88		0.01
$^4F_{9/2} \rightarrow {}^4I_{15/2}$	15205	4246	0	0.21	0.89
$^4I_{13/2}$	8654.7	245.2			0.05
$^4I_{11/2}$	5083	245.5			0.05
$^4S_{3/2} \rightarrow {}^4I_{15/2}$	18299	3433.2	0	0.195	0.67
$^4I_{13/2}$	11749.6	1396.3			0.27
$^4I_{11/2}$	8193.5	114.9			0.02
$^4I_{9/2}$	5861.7	180.7			0.03
$^2H_{11/2} \rightarrow {}^4I_{15/2}$	19072.7	37311.2	0	0.026	0.96
$^4I_{13/2}$	12522.4	531.3			0.01
$^4F_{7/2} \rightarrow {}^4I_{15/2}$	20358.3	8744.1	0	0.087	0.76
$^4I_{13/2}$	13808	1504.7			0.13
$^4I_{11/2}$	10236.4	722.6			0.06
$^4I_{9/2}$	7904.5	425			0.03
$^4F_{5/2} \rightarrow {}^4I_{15/2}$	22114.6	4032	0	0.112	0.45
$^4I_{13/2}$	15564.3	3682.7			0.41
$^4I_{11/2}$	11992.7	389.2			0.04
$^4I_{9/2}$	9660.8	421.2			0.04
$^4F_{9/2}$	6909.6	369.2			0.04
$^4F_{3/2} \rightarrow {}^4I_{15/2}$	22114.6	3417.5	0	0.137	0.47
$^4I_{13/2}$	15564.3	329.4			0.04
$^4I_{11/2}$	11992.7	2628.5			0.36
$^4I_{9/2}$	9660.8	833.7			0.11
$^2H_{9/2} \rightarrow {}^4I_{15/2}$	24735.9	3768.2	0	0.085	0.32
$^4I_{13/2}$	18185.6	5873.4			0.50
$^4I_{11/2}$	14614	1609.7			0.14
$^4I_{9/2}$	12282.1	229.7			0.02
$^4F_{9/2}$	9530.9	123.9			0.01

$$\tau_{R_a} = \frac{1}{\sum_{a'} A_{aa'}} \qquad 4.3.7$$

The measured fluorescence lifetime of the different levels for Er^{3+} in YVO_4 were much faster than the calculated values, as an example the $^4S_{3/2}$ level had a measured lifetime of 6.7 μs in the 2.5% Er^{3+}:YVO_4 crystal and a calculated lifetime of 195 μs (see table 4.3.5). This is due to competing nonradiative processes, in particular multiphonon emission and ion-ion exchange. Detailed discussion of these processes will be given in sections 4.6 and 4.7.

It is important to note that only the transitions involving the $^4I_{13/2}$ and $^4I_{11/2}$ excited states contain a significant magnetic dipole contribution. The transition probability, $A^{md}_{aa'}$, was obtained using the following equation :

$$\left(A^{md}_{aa'}\,(LaF_3)\right)\frac{n^3(YVO_4)}{n^3(LaF_3)} = A^{md}_{aa'}\,(YVO_4{:}Er^{3+}) \qquad (4.3.8)$$

4.4 CRYSTAL-FIELD CALCULATIONS

In the study we analyzed the energy levels of 14 $^{2S+1}L_J$ multiplet manifolds of the $4f^{11}$ (Er^{3+}) electronic configuration. They include 59 crystal field levels of the 70 predicted to be split out in D_{2d} symmetry. The 59 levels were determined from absorption and emission measurements (σ and π polarization), carried out at 7 and 300K. The experimental Stark level energies were used as the input data in the parameterized Hamiltonian. The free ion wavefunctions were determined using a Hamiltonian containing the Coulombic interaction, in the form of the Racah parameters, $E^{(1)}$, $E^{(2)}$ and $E^{(3)}$ and the spin orbit interaction, ξ . Interconfigurational interaction was also included in the form of the parameters, α, β and γ. The free ion parameters chosen for our calculations were obtained from Carnall et al [16]. For Er^{3+} in aqueous solution the parameters are:

$E^{(1)} = 6769.9$, $E^{(2)} = 32.388$, $E^{(3)} = 646.62$,

$\xi = 2380.7$,

$\alpha = 18.347$, $\beta = -509.28$ and $\gamma = 649.71$ (all in cm^{-1}).

The crystal field potential at the Er^{3+} ion sites has D_{2d} symmetry, therefore the Hamiltonian may be expressed as:

$$H_{CF} = \sum_{k,q} B_{kq} \sum_{i=1}^{N} C_{kq}(i) \qquad (4.4.1)$$

where B_{kq} are the crystal field interaction parameters which describes the effect of the crystal on the free-ion energy levels, and C_{kq} is a spherical tensor of rank q and order k. The second sum is over i = 1 to N, where N is the number of electrons ($4f^{11}$), for f electrons, k is limited to values ≤ 6. The even-k terms in Eq. 4.4.1 remove the degeneracy of the free-ion J states of rare earths and cause Stark splittings of ≈ 10^2 cm^{-1}. From the general relationship $B_{k,-q}=(-1)^q B_{kq}$ we note that Equation (4.4.1) may be expanded to the form

$$H_{CF} = B_{20}C_{20} + B_{40}C_{40} + B_{44}[C_{44} + C_{4,-4}] + B_{60}C_{60} + B_{64}[C_{64} + C_{6,-4}] \qquad (4.4.2)$$

In order to initiate the calculation, a set of starting values for B_{kq} must be obtained. The calculated lattice parameters A_{kq}, which are the irreducible spherical tensor components of the electrostatic crystal field calculated from direct point charge lattice sums, are related to the B_{kq} through the radial factors, ρ_k as follows:

$$B_{kq} = \rho_k A_{kq} \qquad (4.4.3)$$

where $\rho_2 = 0.1706$, $\rho_4 = 0.4053$ and $\rho_6 = 0.9649$ [22], and are ion dependent host independent quantities. The set of B_q^k was varied in a least squares calculation which used 59 energy levels in the multiplets $^4I_{15/2}$ through $^2K_{15/2}$. After using the calculated levels to aid in establishing an energy level diagram for Er^{3+} in YVO_4, the parameters in equation 4.4.1 were varied until a least rms value of 6.71 cm^{-1} between the 59 calculated and experimental energy levels were obtained. The B_{kq} yielding this fit are given in Table 4.4.1and they are in good agreement with published results [23,24]. The calculated and experimental energy levels are given in Table 4.4.2.

The crystal field parameter B_{20} is particularly sensitive to the magnitude of the electrostatic interactions. The lattice dependent portion of B_{20} is given by

$$B_{20} \propto \frac{3z^2-r^2}{r^3} \tag{4.4.4}$$

Roughly speaking then, the larger (in magnitude) values of B_{20} imply that the co-ordinating ligands are closer to the rare earth ion. This would imply that a stronger interaction exists between the rare earth ion and the ligands. The absolute value of the B_{20} parameter is larger for Er^{3+} in comparison to Eu^{3+} and Nd^{3+} in the same host crystal (Table 4.4.1). This is not unexpected since Er^{3+} has a greater electron density. The influence of the anion (AsO_4^{3-}, PO_4^{3-}, and VO_4^{3-}) on the crystal field parameters

Table 4.4.1 : Crystal Field Parameters B_{kq} for trivalent Rare earth ions in Yttrium Vanadate Single Crystals

B_{20}	B_{40}	B_{44}	B_{60}	B_{64}	RE^{3+}: Host Crystal
-218	322	914	-702	10	Er^{3+}:YVO_4 [23]
-206	364	926	-688	31.5	Er^{3+}:YVO_4 [24]
-216	196	908	-682	37	Er^{3+}:YVO_4 This work
-122	403	701	-962	-40	Eu^{3+}:YVO_4 [25]
-122	626	1024	-1170	-251	Nd^{3+}:YVO_4 [25]

Table 4.4.2 : Calculated and experimental energy levels of Er^{3+} in D_{2d} symmetry.

$^{2S+1}L_J$	Energy			Free Ion Mixture
	Theoretical	Experimental	Γ_n	
$^4I_{15/2}$	-7	0	Γ_7	99.8 $^4I_{15/2}$
	38	38	Γ_6	99.97 $^4I_{15/2}$ + 0.01 $^4I_{13/2}$ + 0.01 $^4F_{9/2}$
	39	41	Γ_7	99.96 $^4I_{15/2}$ + 0.03 $^4I_{13/2}$
	65	64	Γ_7	99.98 $^4I_{15/2}$ + 0.01 $^4I_{13/2}$ + 0.01 $^4F_{9/2}$
	139	143	Γ_6	99.97 $^4I_{15/2}$ + 0.01 $^4I_{13/2}$
	244	247	Γ_6	99.95 $^4I_{15/2}$ + 0.03 $^4I_{13/2}$ + 0.01 $^4F_{9/2}$
	277	268	Γ_7	99.97 $^4I_{15/2}$ + 0.02 $^4I_{13/2}$
	299	300	Γ_6	99.98 $^4I_{15/2}$ + 0.01 $^4I_{13/2}$
$^4I_{13/2}$	6540	6541	Γ_7	99.88 $^4I_{13/2}$ + 0.08 $^4I_{11/2}$ + 0.01 $^4I_{9/2}$
	6543	6544	Γ_6	99.95 $^4I_{13/2}$ + 0.02 $^4I_{11/2}$ + 0.01 $^4I_{15/2}$
	6583	6585	Γ_7	99.91 $^4I_{13/2}$ + 0.04 $^4I_{11/2}$ + 0.03 $^4I_{15/2}$
	6590	6590	Γ_6	99.85 $^4I_{13/2}$ + 0.09 $^4I_{11/2}$ + 0.02 $^4I_{15/2}$
	6635	6636	Γ_7	99.89 $^4I_{13/2}$ + 0.06 $^4I_{11/2}$ + 0.03 $^4I_{15/2}$
	6698	6695	Γ_7	99.91 $^4I_{13/2}$ + 0.05 $^4I_{11/2}$ + 0.03 $^4I_{15/2}$
	6713	6712	Γ_6	99.91 $^4I_{13/2}$ + 0.06 $^4I_{11/2}$ + 0.02 $^4I_{9/2}$
$^4I_{11/2}$	10183	10184	Γ_6	99.90 $^4I_{11/2}$ + 0.04 $^4I_{9/2}$ + 0.02 $^4F_{9/2}$
	10191	10192	Γ_7	99.84 $^4I_{11/2}$ + 0.05 $^4I_{13/2}$ + 0.04 $^4I_{9/2}$
	10204	10201	Γ_6	99.87 $^4I_{11/2}$ + 0.06 $^4I_{13/2}$ + 0.04 $^4I_{9/2}$
	10222	10232	Γ_7	99.80 $^4I_{11/2}$ + 0.09 $^4I_{13/2}$ + 0.06 $^4I_{9/2}$
	10257	10244	Γ_6	99.78 $^4I_{11/2}$ + 0.16 $^4I_{13/2}$ + 0.03 $^4F_{9/2}$
	10269	10272	Γ_7	99.90 $^4I_{11/2}$ + 0.03 $^4I_{9/2}$ + 0.03 $^4I_{13/2}$
$^4I_{9/2}$	12340	12347	Γ_6	99.93 $^4I_{9/2}$ + 0.02 $^4I_{11/2}$ + 0.01 $^4I_{13/2}$
	12427	---	Γ_7	99.92 $^4I_{9/2}$ + 0.02 $^4I_{11/2}$ + 0.01 $^4I_{11/2}$
	12439	---	Γ_6	99.86 $^4I_{9/2}$ + 0.09 $^4I_{11/2}$ + 0.02 $^2H_{11/2}$
	12501	---	Γ_7	99.82 $^4I_{9/2}$ + 0.09 $^4I_{11/2}$ + 0.03 $^4S_{3/2}$
	12581	12574	Γ_7	99.91 $^4I_{9/2}$ + 0.03 $^4I_{11/2}$ + 0.02 $^4F_{9/2}$

continued...

$^{2S+1}L_J$	Energy			Free Ion Mixture
	Theoretical	Experimental	Γ_n	
$^4F_{9/2}$	15211	15206	Γ_7	99.92 $^4F_{9/2}$ + 0.04 $^4I_{11/2}$ + 0.01 $^4I_{15/2}$
	15230	15233	Γ_6	99.91 $^4F_{9/2}$ + 0.02 $^4F_{5/2}$ + 0.02 $^4I_{11/2}$
	15285	15279	Γ_7	99.90 $^4F_{9/2}$ + 0.04 $^4I_{11/2}$ + 0.01 $^2H_{11/2}$
	15322	15322	Γ_7	99.90 $^4F_{9/2}$ + 0.03 $^4I_{11/2}$ + 0.03 $^4F_{5/2}$
	15333	15342	Γ_6	99.91 $^4F_{9/2}$ + 0.03 $^4I_{11/2}$ + 0.02 $^2H_{11/2}$
$^4S_{3/2}$	18352	18355	Γ_6	98.79 $^4S_{3/2}$ + 1.10 $^2H_{11/2}$ + 0.04 $^4I_{9/2}$
	18363	18360	Γ_7	96.80 $^4S_{3/2}$ + 3.14 $^2H_{11/2}$ + 0.02 $^4G_{11/2}$
$^2H_{11/2}$	19061	19053	Γ_6	99.71 $^2H_{11/2}$ + 0.15 $^4F_{7/2}$ + 0.07 $^4S_{3/2}$
	19091	19080	Γ_7	99.30 $^2H_{11/2}$ + 0.48 $^4S_{3/2}$ + 0.14 $^4F_{7/2}$
	19120	19122	Γ_6	97.18 $^2H_{11/2}$ + 2.72 $^4S_{3/2}$ + 0.03 $^4F_{7/2}$
	19149	19150	Γ_7	99.41 $^2H_{11/2}$ + 0.34 $^4S_{3/2}$ + 0.16 $^4F_{7/2}$
	19158	19158	Γ_6	99.51 $^2H_{11/2}$ + 0.36 $^4S_{3/2}$ + 0.03 $^4F_{5/2}$
	19189	19203	Γ_7	99.39 $^2H_{11/2}$ + 0.29 $^4S_{3/2}$ + 0.26 $^4F_{7/2}$
$^4F_{7/2}$	20434	20439	Γ_6	99.71 $^4F_{7/2}$ + 0.11 $^4F_{5/2}$ + 0.09 $^2H_{11/2}$
	20492	20483	Γ_7	99.65 $^4F_{7/2}$ + 0.24 $^2H_{11/2}$ + 0.02 $^4G_{11/2}$
	20518	20521	Γ_6	99.37 $^4F_{7/2}$ + 0.32 $^2H_{11/2}$ + 0.15 $^4F_{5/2}$
	20529	20530	Γ_7	99.73 $^4F_{7/2}$ + 0.12 $^2H_{11/2}$ + 0.06 $^4F_{5/2}$
$^4F_{5/2}$	22128	22121	Γ_6	97.24 $^4F_{5/2}$ + 2.65 $^4F_{3/2}$ + 0.04 $^2H_{11/2}$
	22144	22143	Γ_7	99.63 $^4F_{5/2}$ + 0.17 $^4F_{7/2}$ + 0.05 $^4F_{9/2}$
	22172	22180	Γ_6	99.29 $^4F_{5/2}$ + 0.43 $^4F_{3/2}$ + 0.17 $^4F_{7/2}$
$^4F_{3/2}$	22477	22479	Γ_6	99.67 $^4F_{3/2}$ + 0.12 $^4F_{7/2}$ + 0.09 $^4G_{9/2}$
	22525	22523	Γ_7	96.80 $^4F_{3/2}$ + 3.08 $^4F_{5/2}$ + 0.05 $^4F_{7/2}$
$^2H_{9/2}$	24445	24453	Γ_6	99.68 $^2H_{9/2}$ + 0.26 $^2K_{15/2}$ + 0.02 $^4F_{5/2}$
	24527	24516	Γ_7	99.49 $^2H_{9/2}$ + 0.28 $^4G_{11/2}$ + 0.18 $^2K_{15/2}$
	24536	24537	Γ_6	99.85 $^2H_{9/2}$ + 0.04 $^4G_{11/2}$ + 0.03 $^4F_{3/2}$
	24582	24600	Γ_7	99.61 $^2H_{9/2}$ + 0.18 $^2K_{15/2}$ + 0.16 $^4G_{11/2}$
	24650	24634	Γ_7	99.59 $^2H_{9/2}$ + 0.19 $^2K_{15/2}$ + 0.14 $^4G_{11/2}$

continued...

$^{2S+1}L_J$	Energy			Free Ion Mixture
	Theoretical	Experimental	Γ_n	
$^4G_{11/2}$	26223	---	Γ_6	$99.51\,^4G_{11/2} + 0.25\,^4G_{9/2} + 0.15\,^2K_{15/2}$
	26248	26236	Γ_7	$99.66\,^4G_{11/2} + 0.17\,^4G_{9/2} + 0.10\,^2K_{15/2}$
	26301	26292	Γ_6	$99.09\,^4G_{11/2} + 0.47\,^2K_{15/2} + 0.31\,^4G_{9/2}$
	26347	26357	Γ_7	$98.66\,^4G_{11/2} + 0.93\,^4G_{9/2} + 0.26\,^2H_{9/2}$
	26395	26403	Γ_6	$99.15\,^4G_{11/2} + 0.31\,^4G_{9/2} + 0.26\,^2K_{15/2}$
	26422	26424	Γ_7	$99.19\,^4G_{11/2} + 0.26\,^4G_{9/2} + 0.24\,^2K_{15/2}$
$^4G_{9/2}$	27452	---	Γ_7	$95.68\,^4G_{9/2} + 2.77\,^2G_{7/2} + 0.75\,^2K_{15/2}$
	27462	---	Γ_6	$96.56\,^4G_{9/2} + 1.95\,^2G_{7/2} + 0.90\,^2K_{15/2}$
	27465	---	Γ_7	$96.80\,^4G_{9/2} + 1.83\,^2G_{7/2} + 1.21\,^2K_{15/2}$
	27497	---	Γ_6	$95.41\,^4G_{9/2} + 3.41\,^2G_{7/2} + 0.72\,^2K_{15/2}$
	27504	---	Γ_7	$99.13\,^4G_{9/2} + 0.56\,^4G_{11/2} + 0.19\,^2K_{15/2}$
$^2K_{15/2}$	27655	27647	Γ_7	$97.49\,^2K_{15/2} + 1.27\,^4G_{9/2} + 0.82\,^2G_{7/2}$
	27662	27670	Γ_6	$98.78\,^2K_{15/2} + 0.69\,^4G_{9/2} + 0.34\,^2G_{7/2}$
	27709	---	Γ_6	$96.37\,^2K_{15/2} + 3.19\,^2G_{7/2} + 0.21\,^2H_{9/2}$
	27739	27739	Γ_7	$89.88\,^2K_{15/2} + 8.88\,^2G_{7/2} + 0.99\,^4G_{9/2}$
	27797	---	Γ_6	$96.43\,^2K_{15/2} + 3.06\,^2G_{7/2} + 0.19\,^4G_{9/2}$
	27822	---	Γ_7	$97.91\,^2K_{15/2} + 1.09\,^2G_{7/2} + 0.73\,^4G_{9/2}$

and the crystal field strength can now be considered. The crystal field strength parameter (S) was calculated using equation 2.3.9. The resulting values, obtained are given in Table 4.4.3. The crystal field strength parameter decreases in the order $S_{YAsO_4} < S_{YPO_4} < S_{YVO_4}$ suggesting that the As^{5+} ion is more strongly bonded to the oxygen which reduces the covalency of the Er-O bond. Further support to the role that the cations (As^{5+}, P^{5+}, and V^{5+}) plays in changing the local field at the Er^{3+} sites may be deduced from the values of the B_{20} parameter (Table 4.4.3). For the $YAsO_4$ the value of B_{20} is in fact smaller than those found for YPO_4 and YVO_4. This is consistent with the interpretation that we have presented.

Table 4.4.3 : Crystal Field Parameters B_{kq} of Er^{3+} in $(Y,Er)AsO_4$, $(Y, Er)PO_4$, and $(Y, Er)VO_4$

B_{20}	B_{40}	B_{44} (cm^{-1})	B_{60}	B_{64}	Crystal field Strength (cm^{-1})	RE^{3+}: Host Crystal
-61.1	93.4	831.4	-591.1	99.7	63.3	$Er^{3+}:YAsO_4$ [26]
282.8	144.8	800.5	-646.4	126.1	78.3	$Er^{3+}:YPO_4$ [26]
-216	196	908	-682	37	80.1	$Er^{3+}:YVO_4$ This work

4.5 THERMALIZATION OF THE $^2H_{11/2}$ LEVEL

Transitions originating from the $^2H_{11/2}$ level are clearly visible at $T > 77K$. At these temperatures, the energy gap of approximately 641 cm^{-1} from the lower lying $^4S_{3/2}$ state can be effectively bridged by high energy phonons. Thermalization of the $^2H_{11/2}$ state has been observed in crystals such as yttrium orthoaluminate ($YAlO_3$) [27] and lanthanum fluoride (LaF_3) [10], and glasses such as barium-thorium fluoride (BaF_2/ThF_4) [28] and fluorohafnates [27].

The temperature dependence of the $^2H_{11/2}$, $^4S_{3/2} \rightarrow {}^4I_{15/2}$ transitions is shown in Figures 4.5.1 and 4.5.2. An increase in the intensity of the $^2H_{11/2} \rightarrow {}^4I_{15/2}$ transition was observed as the temperature was raised from 77K to RT. This observation was accompanied with a decrease in the intensity of the $^4S_{3/2} \rightarrow {}^4I_{15/2}$ transition, due to the depopulation of the $^4S_{3/2}$, feeding level for the thermalization process.

An analysis based on a simple two-level thermalization process comprised of the $^4S_{3/2}$ (level 2), and $^2H_{11/2}$ (level 3) levels predicts that the thermalization of the $^2H_{11/2}$ level may be expressed by the following equation [30]

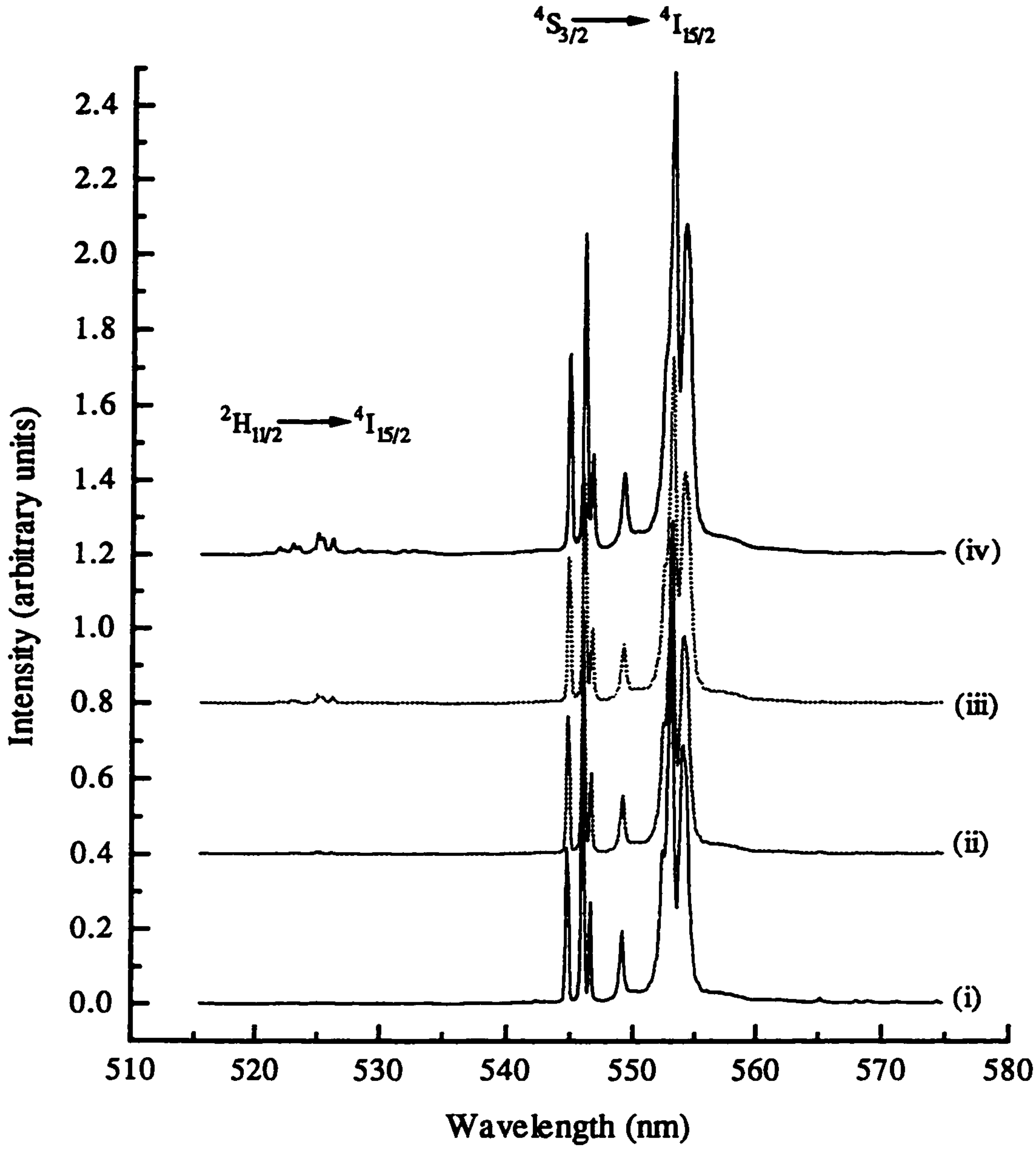

Figure 4.5.1: Temperature-dependent emission spectra of the $^2H_{11/2}$, $^4S_{3/2} \rightarrow {}^4I_{15/2}$ transitions excited at 488 nm for Er^{3+} in YVO_4 i) 77K, ii) 119K, iii) 152K, and iv) 166K.

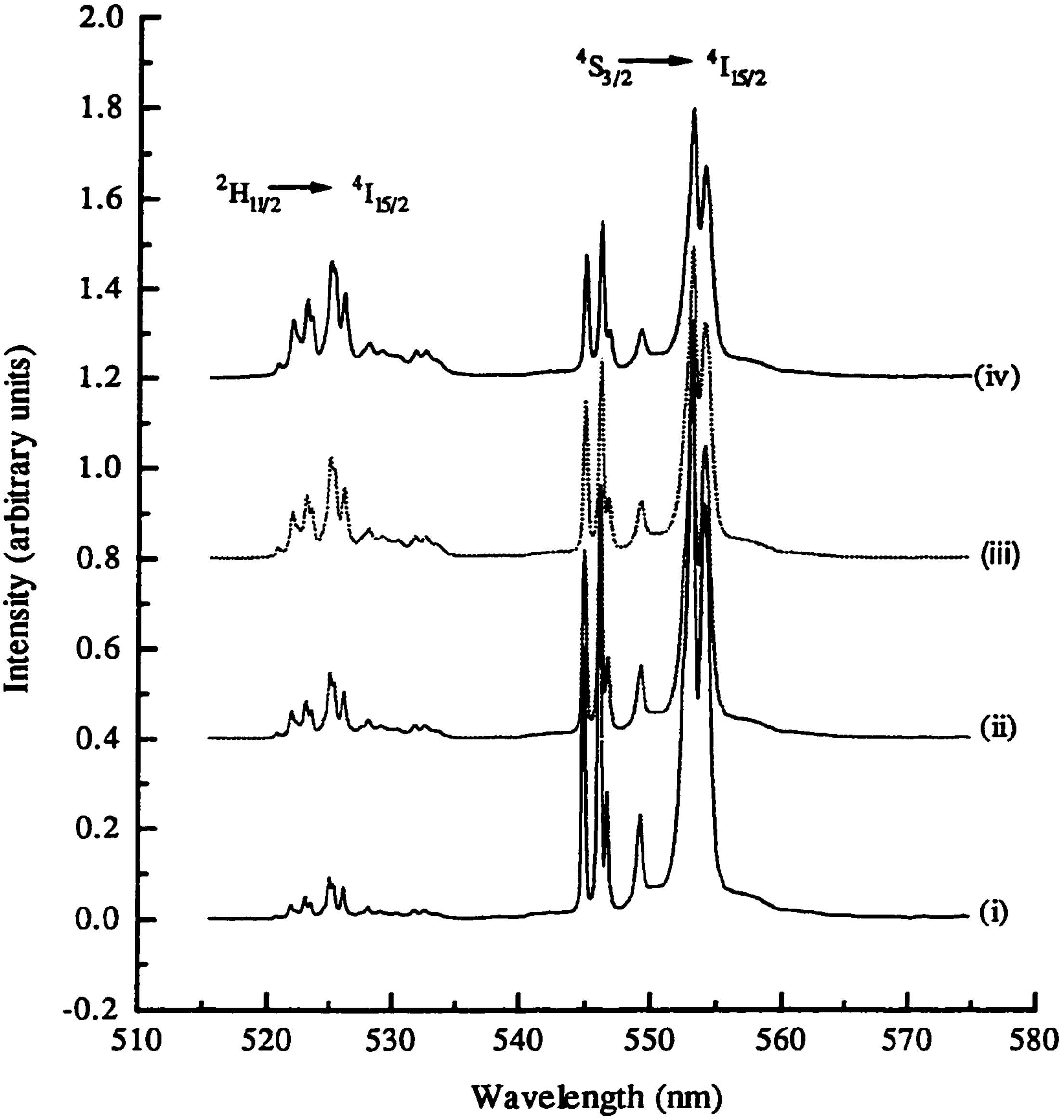

Figure 4.5.2: Temperature-dependent emission spectra of the $^2H_{11/2}$, $^4S_{3/2} \rightarrow {}^4I_{15/2}$ transitions excited at 488 nm for Er^{3+} in YVO_4 i) 182K, ii) 220K, iii) 264K, and iv) RT.

$$\frac{I_3}{I_2} = \frac{\rho_3^r \, g_3 \, \eta\omega_3}{\rho_2^r \, g_2 \eta\omega_2} \exp\left(-\frac{E_{32}}{kT}\right) \qquad (4.5.1)$$

where ρ_2^r and ρ_3^r are the total spontaneous-emission rates, $\eta\omega_2$ and $\eta\omega_3$ are the photon energies, g_2 and g_3 are the degeneracies (2J+1) of the ${}^4S_{3/2}$ and ${}^2H_{11/2}$ levels, respectively, and I_2 and I_3 are the integrated intensities of the ${}^2H_{11/2} \rightarrow {}^4I_{15/2}$ and ${}^4S_{3/2} \rightarrow {}^4I_{15/2}$ transitions, respectively, at a given temperature. The E_{32} term represents the energy gap between the ${}^2H_{11/2}$ and ${}^4S_{3/2}$ levels, *k* is the Boltzman's constant, and T is the temperature in degrees Kelvin. The photon energies of the two levels are similar and may be considered to be equal.

A plot of the logarithm of the ratios of the integrated intensities for the transitions the ${}^2H_{11/2} \rightarrow {}^4I_{15/2}$ and ${}^4S_{3/2} \rightarrow {}^4I_{15/2}$ as a function of 1/T is shown in Figure 4.5.3. The thermal population of the ${}^2H_{11/2}$ level was found to obey the Boltzman distribution for a two level thermalization process (equation 4.5.1). The slope of the line corresponds to an energy gap of 641 cm^{-1}. This value is in excellent agreement with the value ($\Delta E = 644$ cm^{-1}) determined from the spectra. The value of the preexponential factor may be estimated from the product of the ratio of the total spontaneous-emission rates (7.5) and the ratio of the degeneracies (3) and gives a value of 22.5. This value is not in good agreement with the fitted

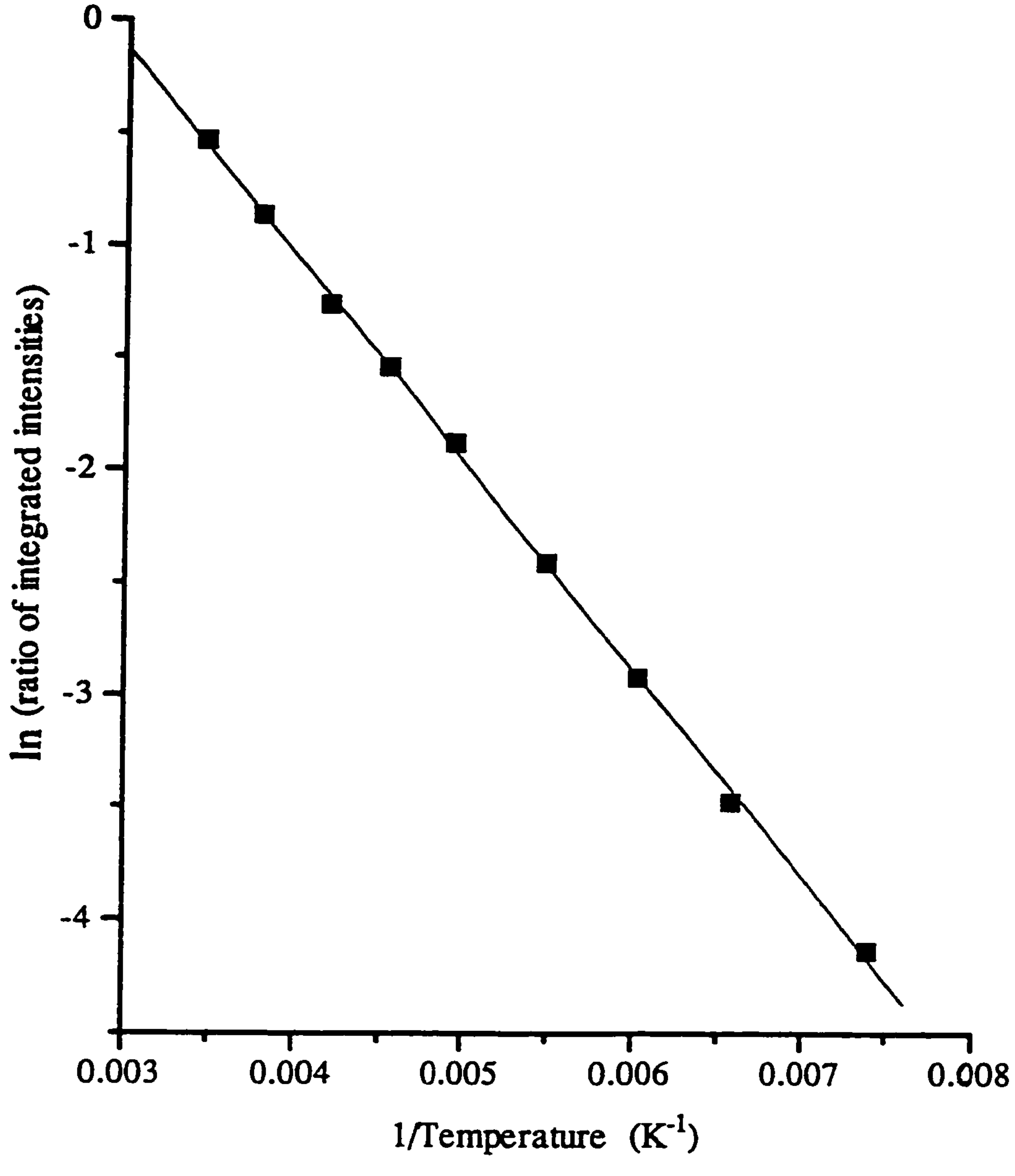

Figure 4.5.3: Plot of the logarithm of the integrated intensity for the transitions $^2H_{11/2} \rightarrow {}^4I_{15/2}$ and $^4S_{3/2} \rightarrow {}^4I_{15/2}$ as a function of temperature.

value of 13.8 , which is due to the values used to calculate the total spontaneous-emission rates (see section 4.3 for explanation).

Direct excitation (544.9 nm) into the $^4S_{3/2}$ level as a function of temperature (77-300K) showed a peak at 19004 cm^{-1} (526.20 nm) (Figure 4.5.4). This peak corresponds to the transition $^2H_{11/2} \rightarrow {}^4I_{15/2}$ and can only be due to thermalization.

The thermalization process was assumed to be a direct two-level process. This was confirmed by a power dependence study. The natural logarithm of the ratio of the intensities of the $^4S_{3/2} \rightarrow {}^4I_{15/2}$ (I_2) and $^2H_{11/2} \rightarrow {}^4I_{15/2}$ (I_1) transitions was plotted versus the natural logarithm of the excitation power. The data were fitted using the following equation

$$I_2 \propto I_1^n \qquad (4.5.2)$$

A straight line was obtained with a slope n = 1.0 which confirms that the thermalization process is a direct two-level process (Fig. 4.5.5).

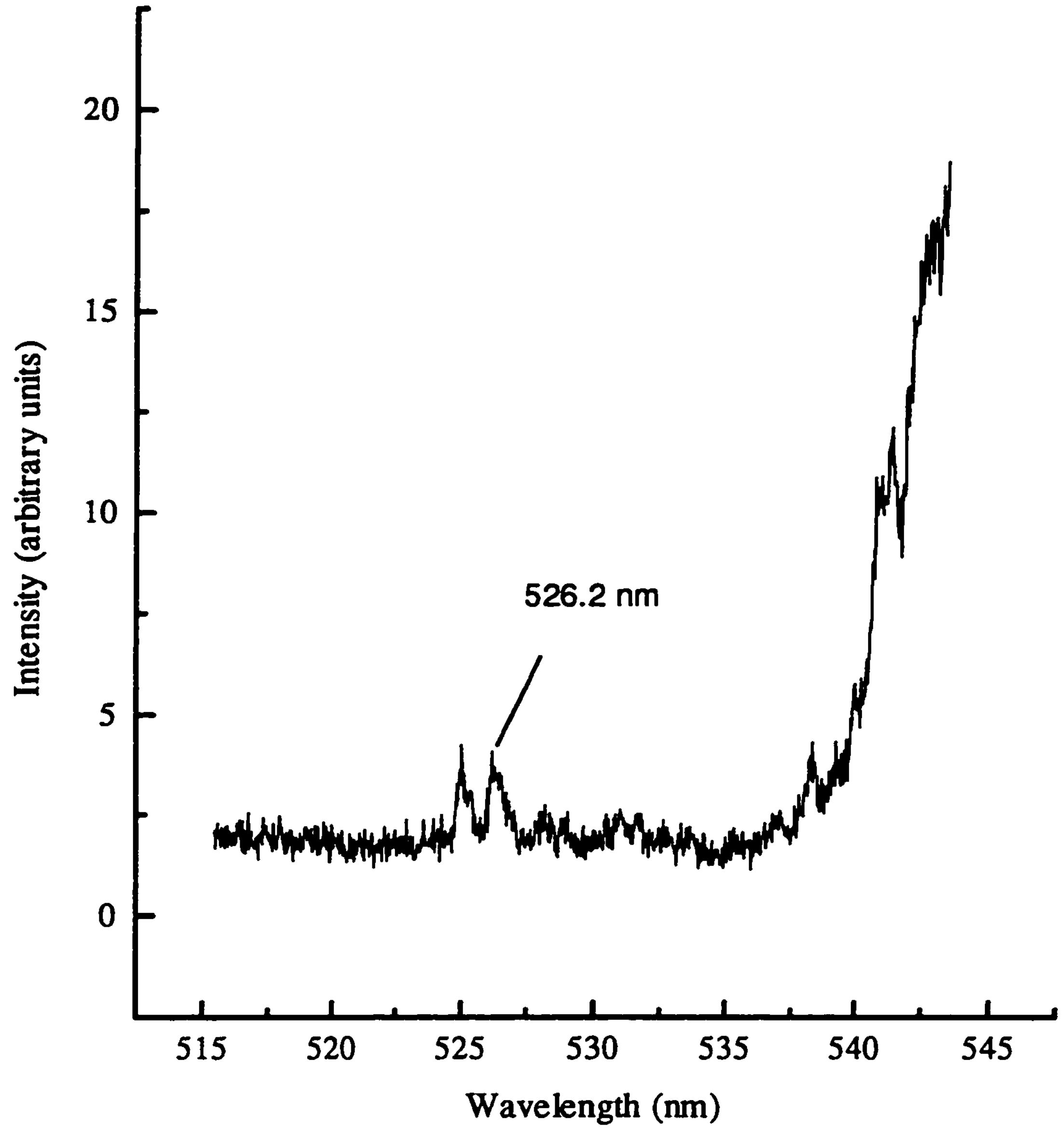

Figure 4.5.4: Thermalization of the $^2H_{11/2}$ level after 544.9 nm excitation into the $^4S_{3/2}$ level at 103K.

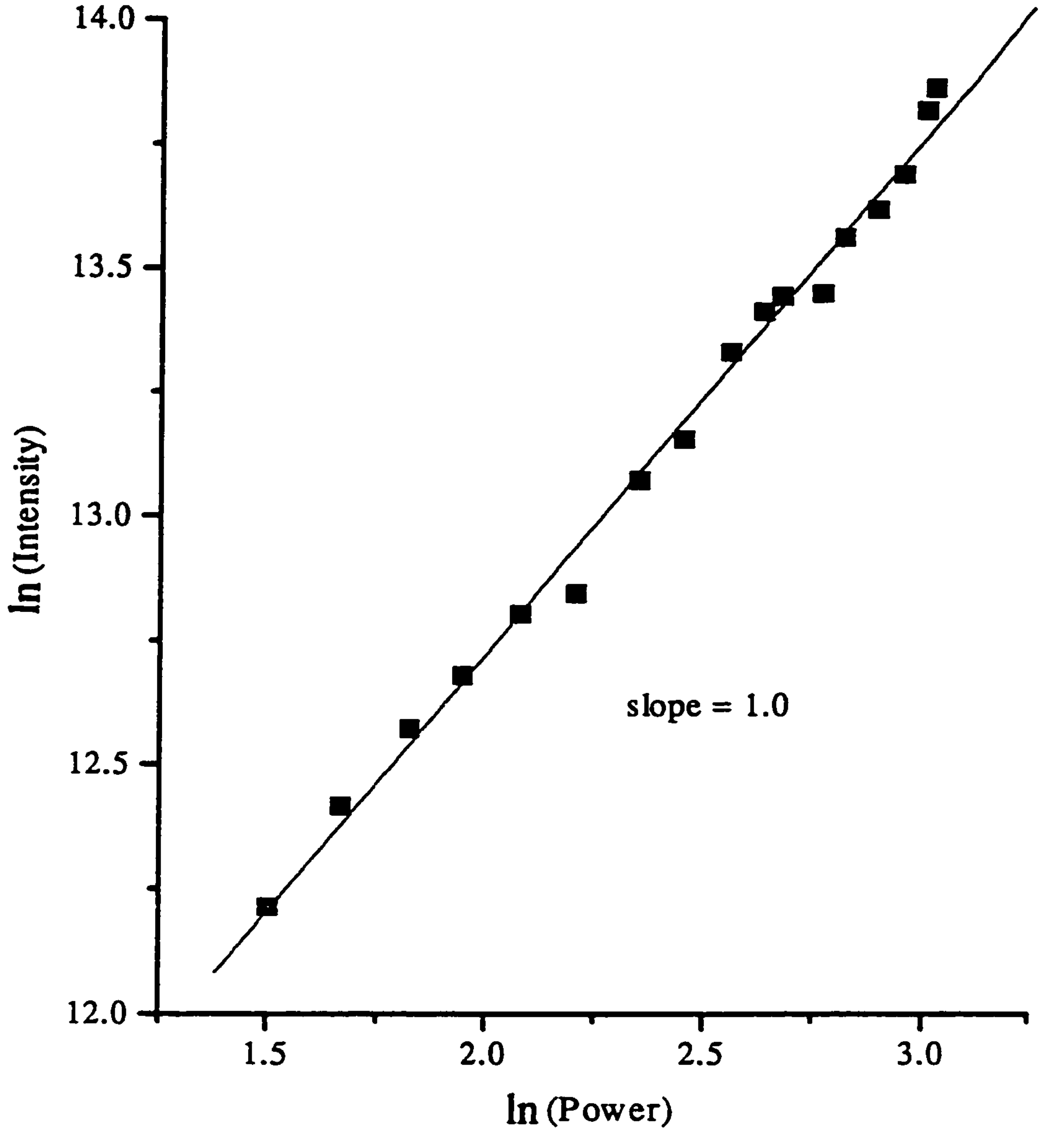

Figure 4.5.5: Laser output power dependence, of the $^2H_{11/2}$ level, on the incident power, obtained at RT following 544.9 nm excitation into the $^4S_{3/2}$ state.

4.6 UPCONVERSION IN $YVO_4 : Er^{3+}$

Upconversion is possible in rare earth doped materials since the $4f^N$ electronic structure of these ions provide many long lived intermediate levels that can be populated with infrared radiation as well as metastable higher lying levels that give rise to strong visible emission [31,32]. To date upconversion and upconversion lasing have been observed in a variety of rare earth ions: Pr^{3+}, Nd^{3+}, Ho^{3+}, Er^{3+} and Tm^{3+}. These ions exhibit metastable intermediate levels that are accessible by red and near infrared pump wavelengths available from such diverse sources as a Ti^{3+}-sapphire laser or III - V semiconductor diode lasers. Upconverted visible fluorescence has been observed for a variety of Er^{3+} doped fluoride and oxide crystals and glasses [29,33-37]. Different upconversion mechanisms have been identified [31]. The first type represents a sequential two photon absorption as exemplified by the 792 and 840 nm excited 550 nm upconversion emission of Er^{3+}:$YAlO_3$ at a temperature of 77K [38]. This process is known to be generally inefficient because of the small two photon absorption cross section. The second type represents upconversion by energy transfer between two neighbouring rare-earth ions. Two ions in close proximity are coupled by a non-radiative process in which one ion returns to the ground state while the other ion is promoted to higher excited state. These coupled neighbouring ions need not be of the same atomic type. The presence of a co-dopant can be used to optimize the absorption process and the upconversion emission process. An example of this type of mechanism is shown by the 35K temperature, 969 nm excited 470 and 560 nm upconversion emission of Er^{3+}:$LiYF_4$ [39]. The third much rarer type involves excited state absorption of the exciting photons followed by interionic cross-relaxation. This type is exemplified by Pr^{3+}:LaF_3 [40]. These three upconversion mechanisms can be readily distinguished by their temperature and concentration dynamical behaviours. In this section we will discuss the mechanism(s) of upconversion pertinent to Er^{3+} doped in YVO_4.

Upconversion was observed at different concentration of Er^{3+} in the range 0.1 to 10% and at three excitation wavelength 652.7, 799.1 and 979 nm. The intensity of the upconverted emission was found to be dependent on the excitation wavelength and the power of the excitation source.

4.6.1 Excitation into the $^4F_{9/2}$ level

Figure 4.6.1.1 shows the room temperature fluorescence spectra obtained using a continuous wave (CW) excitation (652.7 nm) of the $^4F_{9/2} \leftarrow {}^4I_{15/2}$ transition. Three emission bands centered at 524, 553 and 580 nm were observed corresponding to the transitions $^2H_{11/2}$, $^4S_{3/2} \rightarrow {}^4I_{15/2}$ and $^2H_{9/2} \rightarrow {}^4I_{13/2}$ respectively. An excitation power of 380 mW was used. A pronounced concentration

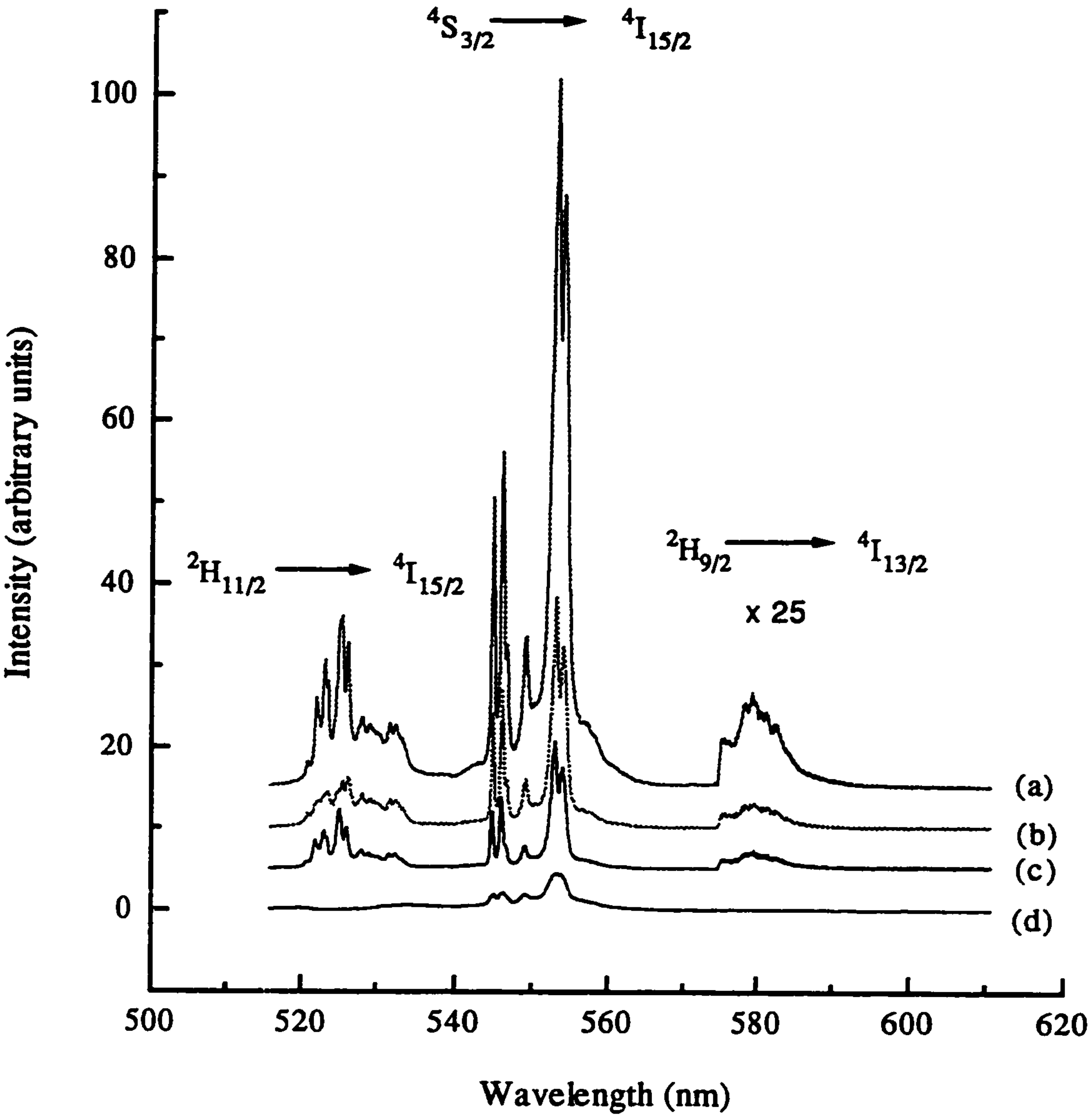

Figure 4.6.1.1 : Room temperature fluorescence spectra of Er^{3+}:YVO_4 crystals following 652.7 nm excitation (Excitation power = 380 mW); a) 2.5%, b) 1.0%, c) 0.1%, and d) 10% Er^{3+}.

dependence of the upconverted emission signal was observed. The maximum in the fluorescence signal was obtained for the 2.5% Er^{3+} doped crystal. The fluorescence signal decreased as the concentrations of the Er^{3+} ions decreased. However, the 10% Er^{3+} doped crystal did not follow this trend, this may be attributed to concentration quenching.

Fig 4.6.1.2 shows the room temperature upconverted emission spectrum upon 652.7 nm excitation and the fluorescence spectrum upon 488 nm excitation. An excitation power of 380 mW was used. The spectral band shapes and positions are identical, however the intensities are significantly different. This result is not unexpected considering the fact that although for both excitations the de-excitation pathways are the same, the mechanism of upconversion is not as efficient in populating the excited states. The emission occurs predominantly from the $^4S_{3/2}$ state however fluorescence from the $^2H_{11/2}$ is also observed. The $^2H_{11/2}$ state is situated 641 cm^{-1} above the $^4S_{3/2}$ and it is thermally populated (see Section 4.5). At room temperature the two states are in thermal equilibrium, and the energy gap is such that the population of $^2H_{11/2}$ is small (see Section 4.2.2.).

Chamarro and Cases [29] have shown that the intensity of the upconverted fluorescence, I_o, to be proportional to some power n of the excitation intensity I_i, that is

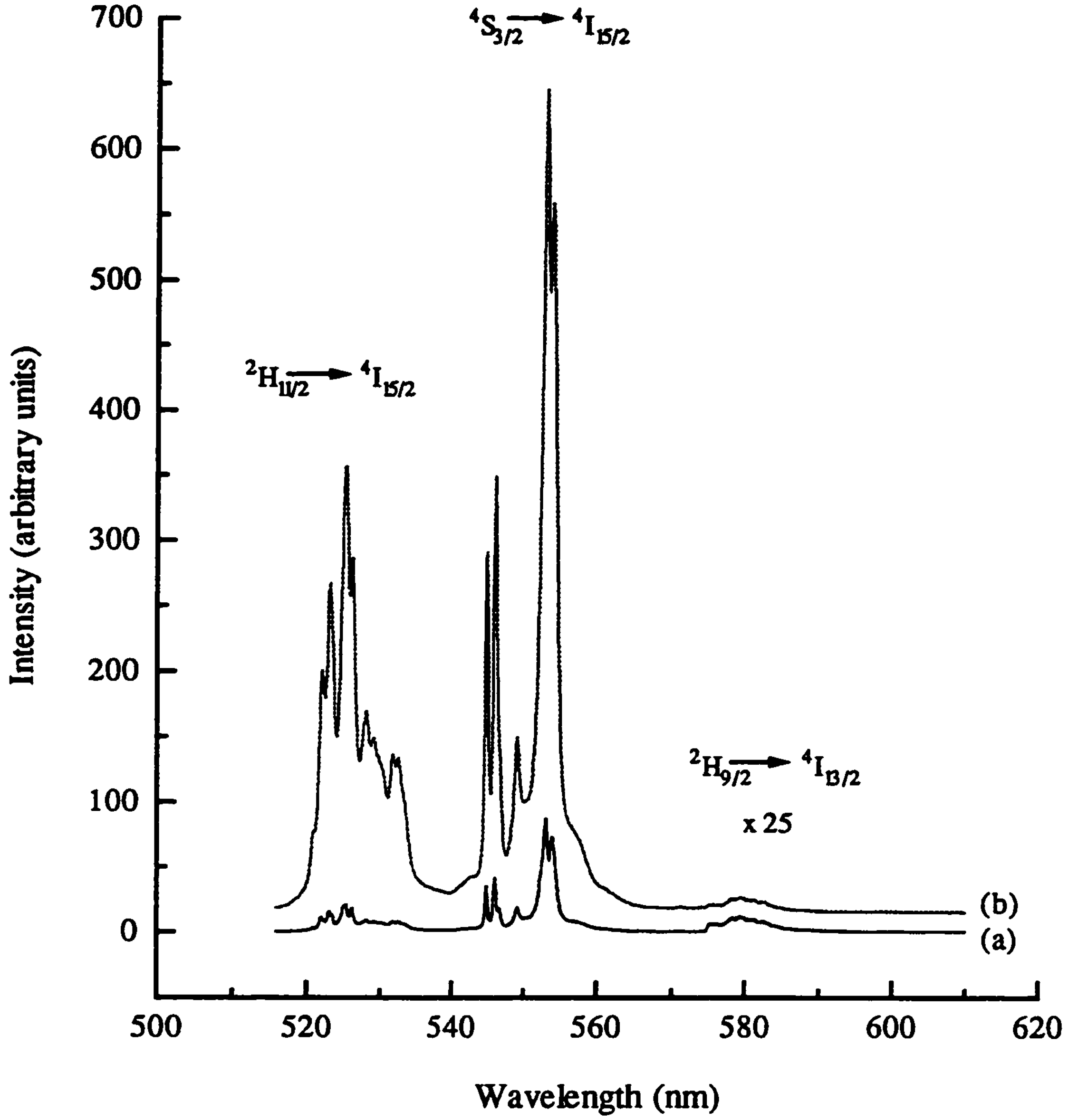

Figure 4.6.1.2 : Room temperature fluorescence spectra of a 2.5% Er^{3+} doped YVO_4 crystal following a) 652.7 nm and b) 488 nm excitation (Excitation power = 380 mW).

$$I_o \alpha I_i^n \quad \text{where } n = 2,3,.... \qquad 4.6.1.1$$

where n is the number of photons absorbed per upconverted photon emitted. The value of n may be determined from the slope of the line obtained by plotting ln (I_o) versus ln (I_i). Our results were fitted using equation 4.6.1.1, and a quadratic dependence on excitation intensity was obtained for the 524, 553, and 580 nm emissions, indicating that the absorption of two photons is necessary for upconversion to occur (Fig. 4.6.1.3).

The essential processes for upconversion emissions upon 652.7 nm excitation, may be explained by considering the energy-level diagram of Er^{3+}, shown in Figure 4.6.1.4 (route a) for two Er^{3+} ions. The mechanism involves the following steps [41] (i) the Er^{3+} ions are excited into their respective $^4F_{9/2}$ levels (ii) one of the excited ions may decay non-radiatively to the $^4I_{9/2}$ level (iii) the second Er^{3+} ion transfers its energy resulting in the excitation of the first ion to the $^2K_{15/2}$ state (iv) a sequence of multiphonon relaxation steps to the various metastable states ($^4G_{11/2}$, $^2H_{9/2}$, $^4F_{3/2,5/2,7/2}$, $^2H_{11/2}$, and $^4S_{3/2}$) occurs with the subsequent radiative emission from the $^2H_{9/2}$, $^4S_{3/2}$ and $^2H_{11/2}$ levels occurring.

On the other hand, the upper $^2K_{15/2}$ level may be populated via a sequential absorption of photons (Fig 4.6.1.4 route b),

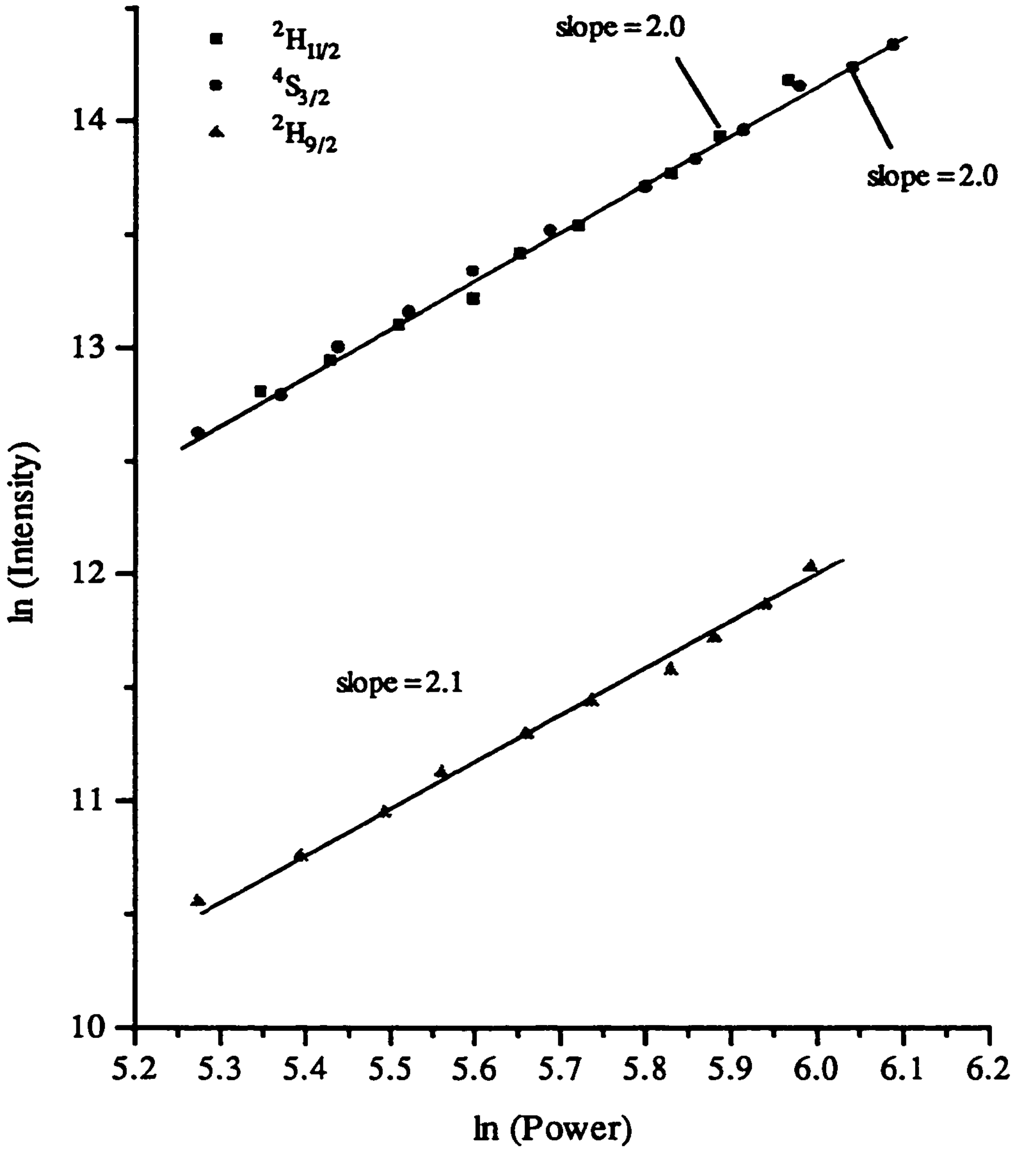

Figure 4.6.1.3 : Upconversion emission intensities versus excitation power in Er^{3+}:YVO_4 crystals upon 652.7 nm excitation.

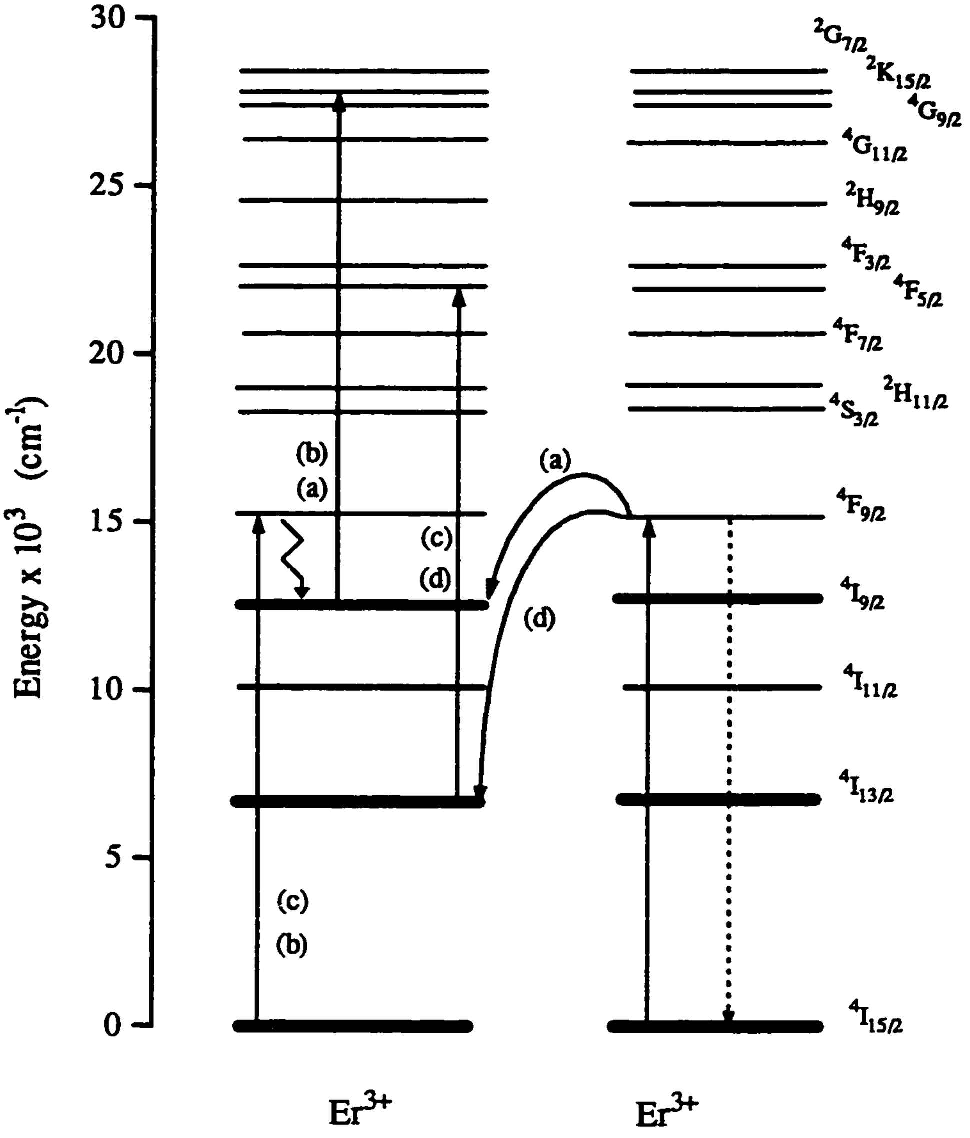

Figure 4.6.1.4 : Energy level diagram of Er^{3+} ions in YVO_4 showing a & d) energy transfer process , b & c) sequential absorption of two photons process. $\lambda_{Ex} = 652.7$ nm.

$$^4I_{9/2} + h\nu \rightarrow {}^2K_{15/2}$$

Both processes, energy transfer or the sequential absorption of photons, are resonant with a perfect match between the excitation energy (15321 cm^{-1}) and the energy gap between the lowest Stark level of the $^4I_{9/2}$ manifold and the second Stark level of the $^2K_{15/2}$ manifold (15323 cm^{-1}).

The ions in the $^4I_{9/2}$ level could radiatively or non-radiatively decay further to the $^4I_{13/2}$ manifold. The ions are then excited via two different mechanisms; an absorption of another photon by the same Er^{3+} ion (Fig 4.6.1.4 route c),

$$^4I_{13/2} + h\nu \rightarrow {}^4F_{5/2}$$

or an energy transfer from a neighbouring ion, of the type (Fig. 4.6.1.4 route d)

$$^4I_{13/2} + {}^4F_{9/2} \rightarrow {}^4F_{5/2} + {}^4I_{15/2}$$

Both of these processes require the absorption of phonons to compensate for the mismatch in energy (259 cm^{-1}) between the excitation energy (15321 cm^{-1}) and the energy gap between the lowest Stark levels of the $^4I_{13/2}$ and $^4F_{5/2}$ manifolds (15580 cm^{-1}).

Evidence supporting both sequential absorption of photons and energy transfer processes exist. Energy transfer is corroborated by the decrease in the fluorescence decay time with concentration and the observation of a rise time. Nevertheless in crystals with low dopant concentration, such as in the 0.1 % Er^{3+} doped crystal, energy transfer is not likely, yet upconverted green fluorescence was still observed. Such observations are explained by the sequential absorption of photons which is responsible for the upconversion process.

Blue emission from the $^4F_{3/2,5/2,7/2}$ states was not observed. This is due to efficient multiphonon relaxations from the ^4F states to the lower lying $^2H_{11/2}$ and $^4S_{3/2}$ levels, which is dependent on the energy gap between the levels involved and the phonon energy available to the lattice. The energy gaps between the $^4F_{3/2}$-$^4F_{5/2}$ (299 cm^{-1}), $^4F_{5/2}$-$^4F_{7/2}$ (1591 cm^{-1}) and $^4F_{7/2}$-$^2H_{11/2}$ (1236 cm^{-1}) states may be bridged by one, two and two phonons (highest phonon energy = 890 cm^{-1}), respectively. The energy gap between the $^2H_{9/2}$-$^4F_{3/2}$ states is 1930 cm^{-1} and can be bridged by three phonons. This gap is large enough to allow for both radiative and non-radiative decay from the $^2H_{9/2}$ state to the $^4I_{13/2}$ and ^4F levels, respectively. The validity of such processes was corroborated by the relatively weak fluorescence from the $^2H_{9/2}$ state. Radiative decay from the $^4F_{7/2}$ level was not observed neither at room or low temperature confirming the multiphonon relaxation to the $^2H_{11/2}$ and $^4S_{3/2}$ states. We point out that the presence of the $^2H_{9/2} \rightarrow {}^4I_{13/2}$ transition in the luminescence spectrum measured following 488 nm excitation, is due to an upconversion process, since the 488 nm radiation cannot directly populate the $^2H_{9/2}$ level. The mechanism responsible for this process will not be considered in this thesis.

4.6.2 Excitation into the $^4I_{9/2}$ level

Figure 4.6.2.1 shows the room temperature fluorescence spectra obtained using a continuous wave excitation (799.1 nm) tuned to the $^4I_{9/2} \leftarrow {}^4I_{15/2}$ absorption band. Green and red emission bands centered at 524, 553, 580 and 660 nm were observed, corresponding to the transitions $^2H_{11/2} \rightarrow {}^4I_{15/2}$, $^4S_{3/2} \rightarrow {}^4I_{15/2}$, $^2H_{9/2} \rightarrow {}^4I_{13/2}$, and $^4F_{9/2} \rightarrow {}^4I_{15/2}$ of Er^{3+} ions, respectively. An excitation power of 240 mW was used. A pronounced concentration dependence of the upconverted signal was observed. The fluorescence signal increased with Er^{3+} concentration and reached a maximum for the 2.5% Er^{3+} doped crystal, after which a noticeable drop in the signal intensity was observed in the 10% Er^{3+} doped crystal due to concentration quenching.

The spectra corresponding to the upconverted green and red emission following 799.1 nm excitation are the same (except for the intensity) as those

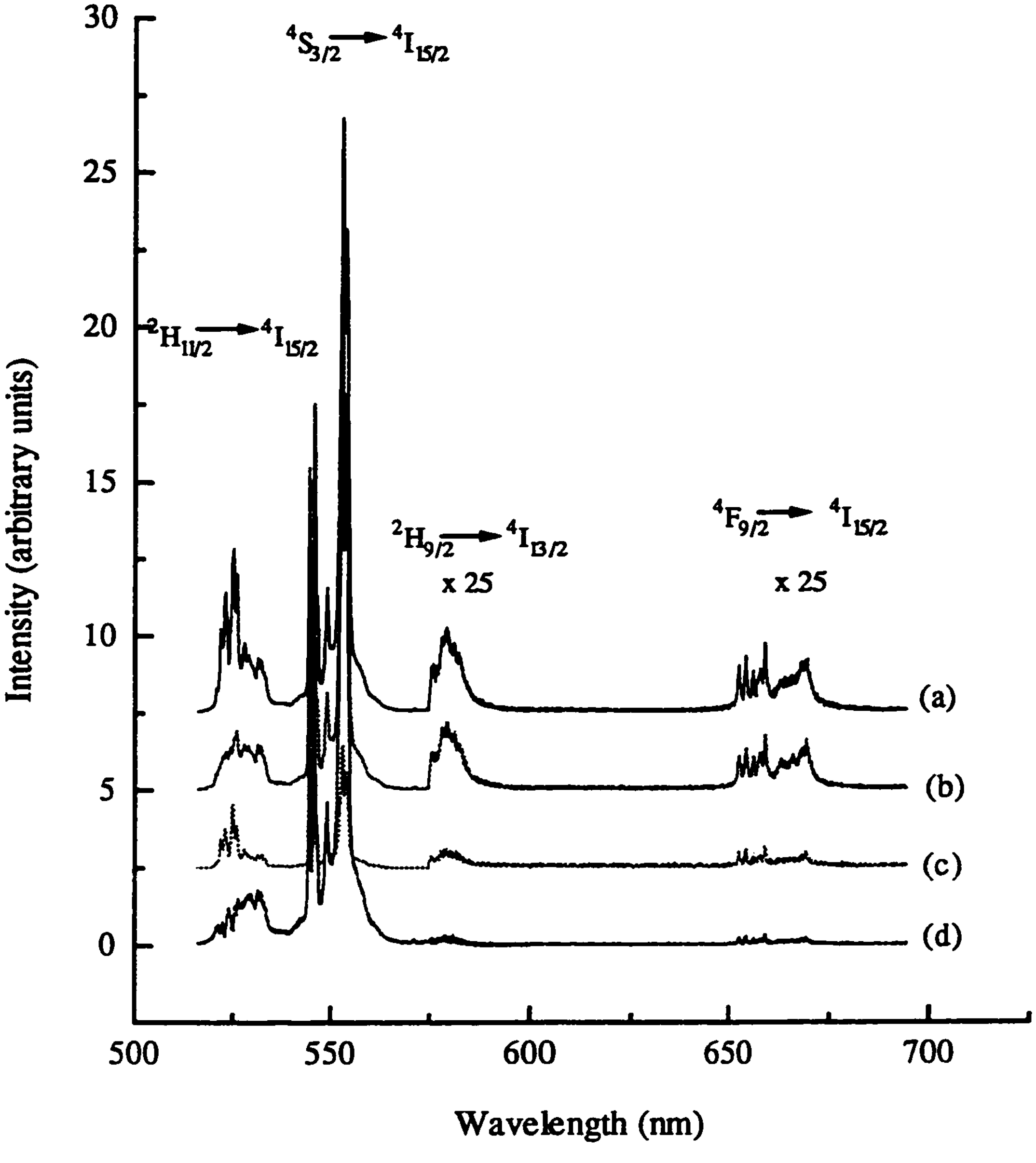

Figure 4.6.2.1 : Room temperature fluorescence spectra of Er^{3+} doped YVO_4 following 799.1 nm excitation (Excitation power = 240 mW); a) 2.5%, b) 1.0%, c) 0.1%, and d) 10% Er^{3+}.

obtained under direct 488 nm excitation for the same excitation power (240 mW). Figure 4.6.2.2 shows the spectra and we notice the similarity in spectral band shapes and positions. This result is expected, and it shows the efficiency in populating the excited states using the 488 nm excitation versus the upconversion process. Nevertheless, the relative intensities of the $^2H_{11/2}$, $^4S_{3/2} \rightarrow {}^4I_{15/2}$ and the $^4F_{9/2} \rightarrow {}^4I_{15/2}$ upconversion fluorescences are seen to be the same as those obtained under direct 488 nm excitation. The green upconverted fluorescence was found to be 200 times stronger than the red one.

The possible processes for upconversion of the $^4I_{9/2}$ excitation to $^2H_{9/2}$ are shown in Figure 4.6.2.3. In the first step, 799.1 nm excitation (12514 cm^{-1}) excites Er^{3+} ions into the $^4I_{9/2}$ (4th Stark level (3)), from which they non-radiatively decay to the lowest level of the $^4I_{9/2}$ manifold. The ions could now be excited via two different mechanisms, a sequential absorption of a second photon or energy transfer. These two mechanisms are shown in Figure 4.6.2.3. The energy transfer process may be written as

$$^4I_{9/2}\,(0) + {}^4I_{9/2}\,(0) \rightarrow {}^4I_{15/2}\,(5) + {}^2H_{9/2}\,(0)$$

and is almost resonant with $\Delta E = 6\ cm^{-1}$ (Fig. 4.6.2.3), while the sequential absorption of two photon process by the same ion

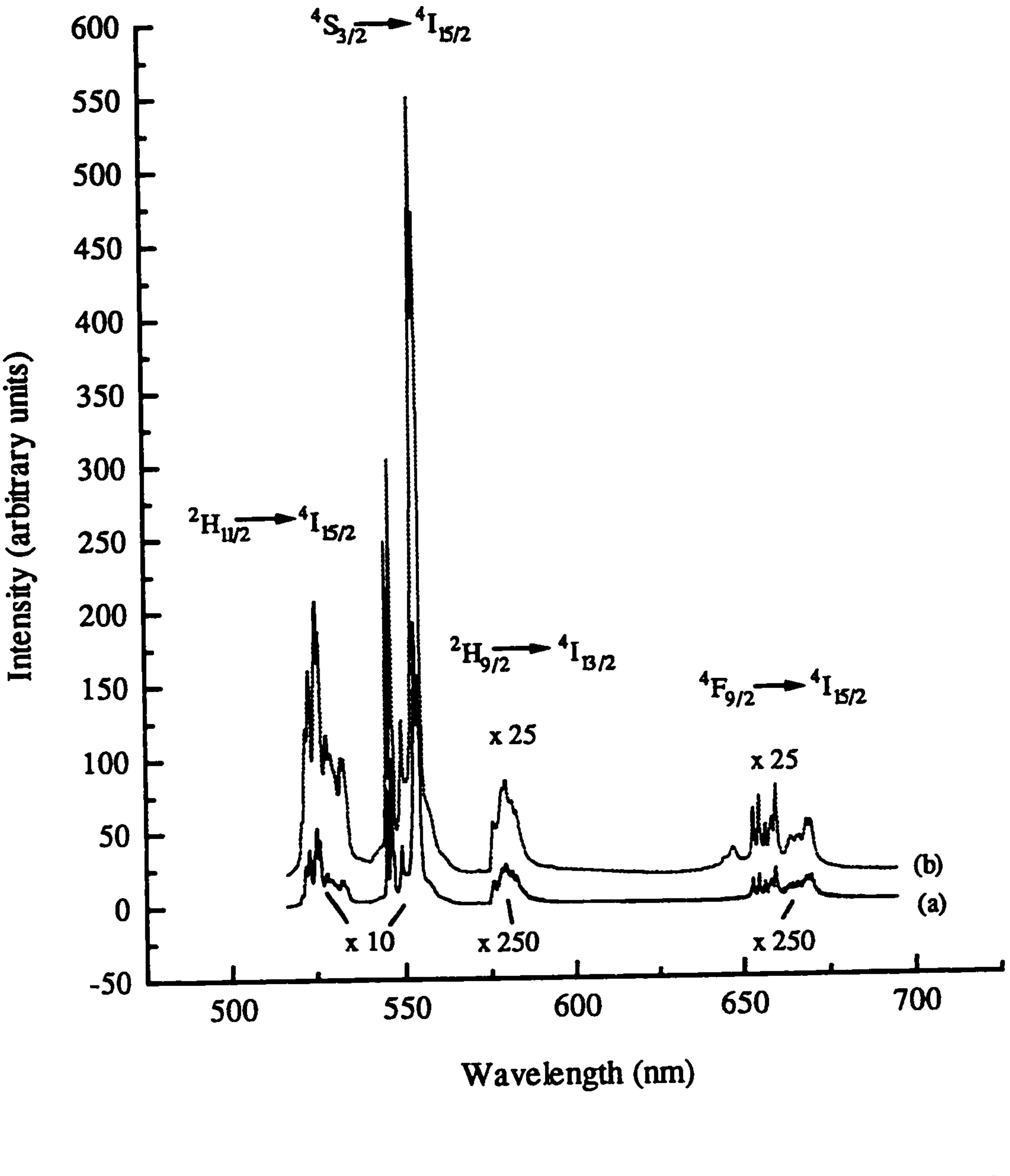

Figure 4.6.2.2 : Room temperature fluorescence spectra of a 2.5% Er^{3+} doped YVO_4 crystal following a) 799.1 nm and b) 488 nm excitation, (Excitation power = 240 mW).

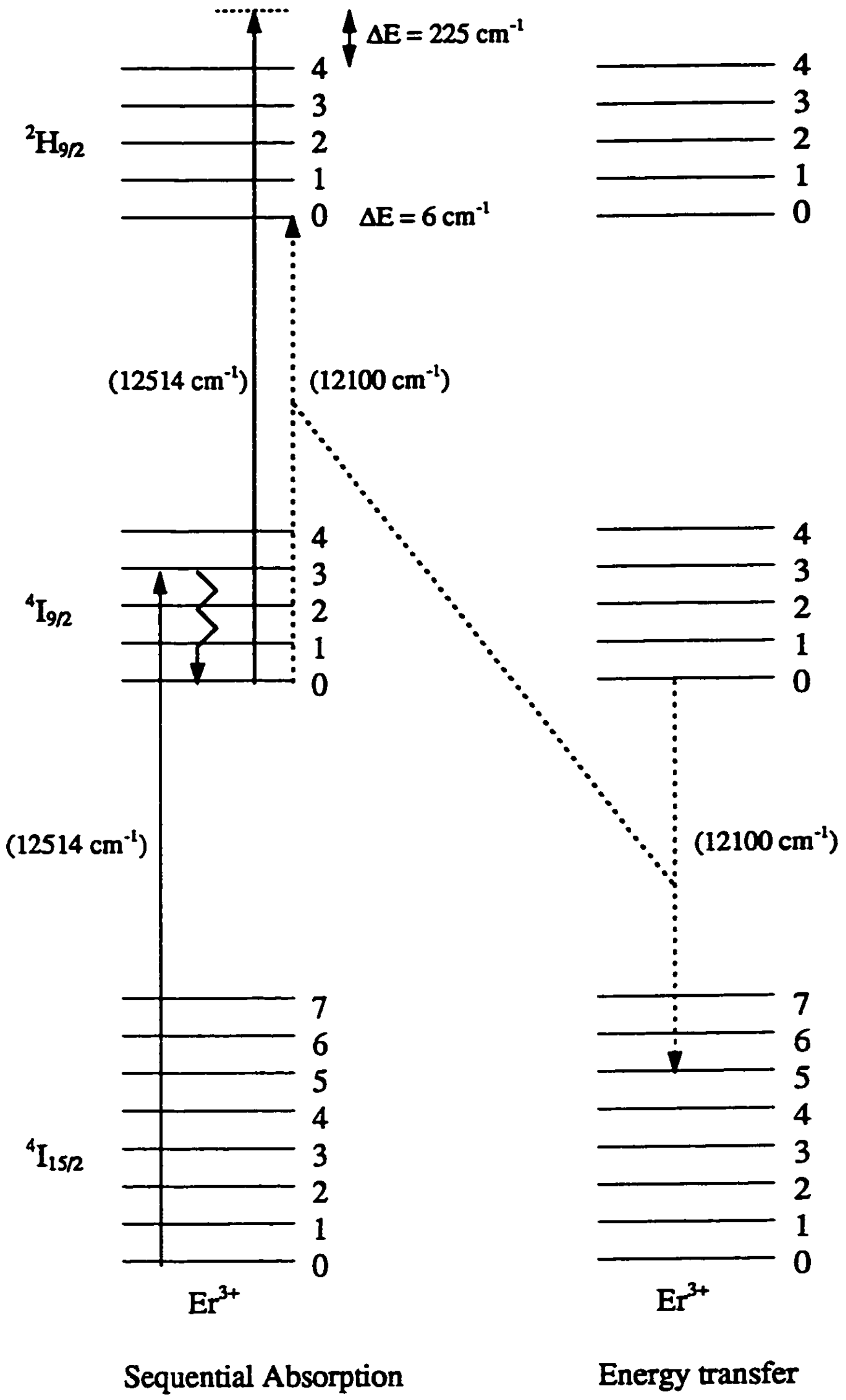

Figure 4.6.2.3 : Schematic representation of the sequential absorption of two photon process and an energy transfer process, in YVO_4:Er^{3+}. λ_{Ex} = 799.1 nm

$$^4I_{9/2}\,(0) + h\nu \rightarrow {}^2H_{9/2}\,(4)$$

is off-resonant by at least 225 cm^{-1} for the given excitation energy ($h\nu$ = 12514 cm^{-1}) (Fig. 4.6.2.3). Hence energy transfer upconversion is expected to be the dominant upconversion mechanism for $^4I_{9/2}$ excitation. Hehlen and co-workers [42] observed the same phenomenon in an Er^{3+} doped $Cs_3Lu_2Br_9$ single crystal. They concluded that the $^4I_{9/2}$ upconversion to $^2H_{9/2}$ cannot occur in an isolated Er^{3+} ion and at least two excited ions in close proximity are required to populate $^2H_{9/2}$ via an energy transfer upconversion process. However in our case evidence of both processes exist. The observation of a rise time in the decay curve of the $^4S_{3/2}$ level supports energy transfer, while the observation of upconversion at low dopant concentrations of Er^{3+} (0.1%), where energy transfer upconversion is not likely to occur, indicates the presence of a sequential two photon absorption process.

Once excited to the $^2H_{9/2}$ manifold, the ions can radiatively decay to the lower lying manifolds, with the observation of the $^2H_{9/2} \rightarrow {}^4I_{13/2}$ transition (580 nm), or may non-radiatively decay to the lower lying levels, mainly the $^4S_{3/2}$ level to produce green emission. Nonetheless, upconversion via the $^4I_{9/2}$ level is not the most probable, due to the short lifetime of this level (0.5 μs) [43,44], therefore other upconversion pathways must be considered.

The ions in the $^4I_{9/2}$ level may undergo multiphonon relaxation to the lower $^4I_{11/2}$ level with high efficiency [45]. Then they can sequentially absorb 799.1 nm photons which excite them to the $^4F_{3/2}$ level [46,47]. The ions in the $^4F_{3/2}$ level undergo multiphonon relaxation through the $^4F_{7/2}$ to the $^2H_{11/2}$ and the $^4S_{3/2}$ levels (Fig. 4.6.2.4a). This process requires the emission of phonons to compensate for the mismatch (175 cm^{-1}) between the pump energy (12514 cm^{-1}) and the separation between the lowest Stark level of the $^4I_{11/2}$ level and the highest of the $^4F_{3/2}$ level (12339 cm^{-1}).

The ions in the $^4I_{11/2}$ can further decay to the $^4I_{13/2}$ level [29] from which they can be excited to the $^2H_{11/2}$ level via a sequential absorption of a second pump photon (Fig. 4.6.2.4b). This process is resonant with no mismatch in energy between the pump energy (12514 cm^{-1}) and the separation between the lowest Stark level of the $^4I_{13/2}$ manifold and the lowest level of the $^2H_{11/2}$ manifold (12513 cm^{-1}).

The upconversion process may also occur by a cross-relaxation (Fig. 4.6.2.4c) between interacting Er^{3+} pairs as has been observed in Er^{3+} doped $LiNbO_3$ crystals [48] and other matrices [49-51]. The occurrence of interaction between Er^{3+} pairs at the concentration levels used in this work is demonstrated by the substantial reduction of the observed lifetime of the $^4S_{3/2}$ level. The decay time

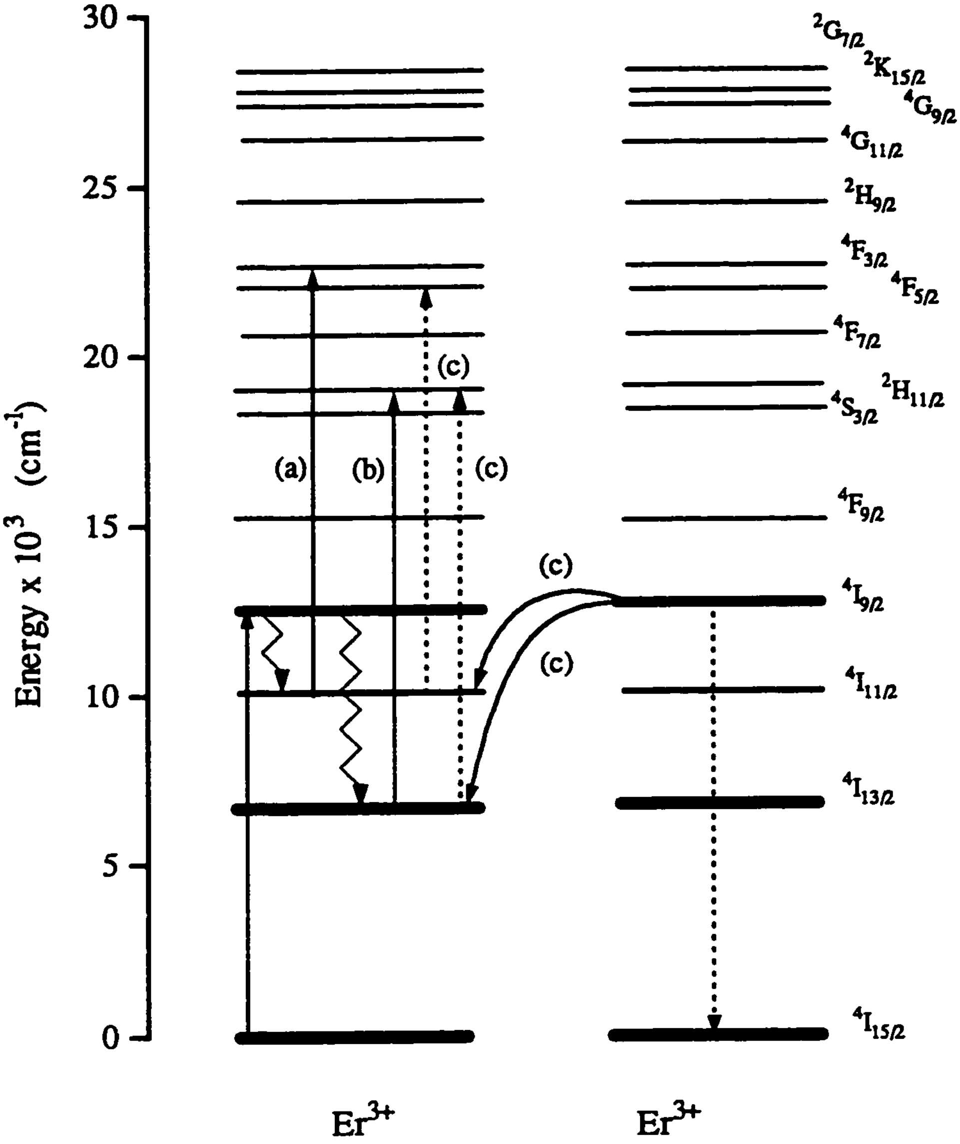

Figure 4.6.2.4 : Energy level diagram and schematic representations of the upconversion processes in YVO_4: Er^{3+}, a & b) sequential absorption of two photons and c) cross relaxation energy transfer. λ_{Ex} = 799.1 nm.

of the $^4S_{3/2}$ was found to be 6.7 μs in the 2.5% Er^{3+} doped crystal in comparison to 10 μs in the 0.1% Er^{3+} doped crystal.

The red emission is identified as the $^4F_{9/2} \rightarrow {}^4I_{15/2}$ transition from the energy level diagram. The $^4F_{9/2}$ level may be populated from the $^4S_{3/2}$ level via multiphonon relaxation. The energy gap between the two levels is 3013 cm^{-1} and the maximum phonon energy available is 890 cm^{-1}. Hence, four phonons are required for the process to occur. This process is more important at low Er^{3+} concentrations (0.1% Er^{3+}). However as the Er^{3+} concentration increases ($\geq$ 1.0 % Er^{3+}) energy transfer between excited ions becomes important. One ion decays from the $^4S_{3/2}$ level and the second is excited to the $^4F_{9/2}$ level via the following process,

$$^4S_{3/2} + {}^4I_{9/2} \rightarrow 2\,{}^4F_{9/2}$$

This process is very probable, since the energy mismatch between the $^4S_{3/2}$-$^4F_{9/2}$ levels (3013 cm^{-1}) and the $^4F_{9/2}$-$^4I_{9/2}$ (2995 cm^{-1}) is very small (18 cm^{-1}) [45].

The intensities of upconverted green emission at 524, 553, and 580 nm have been measured as a function of pump power at 799.1 nm, and the results are shown in Figure 4.6.2.5. The data shown in Figure 4.6.2.5 for each of the

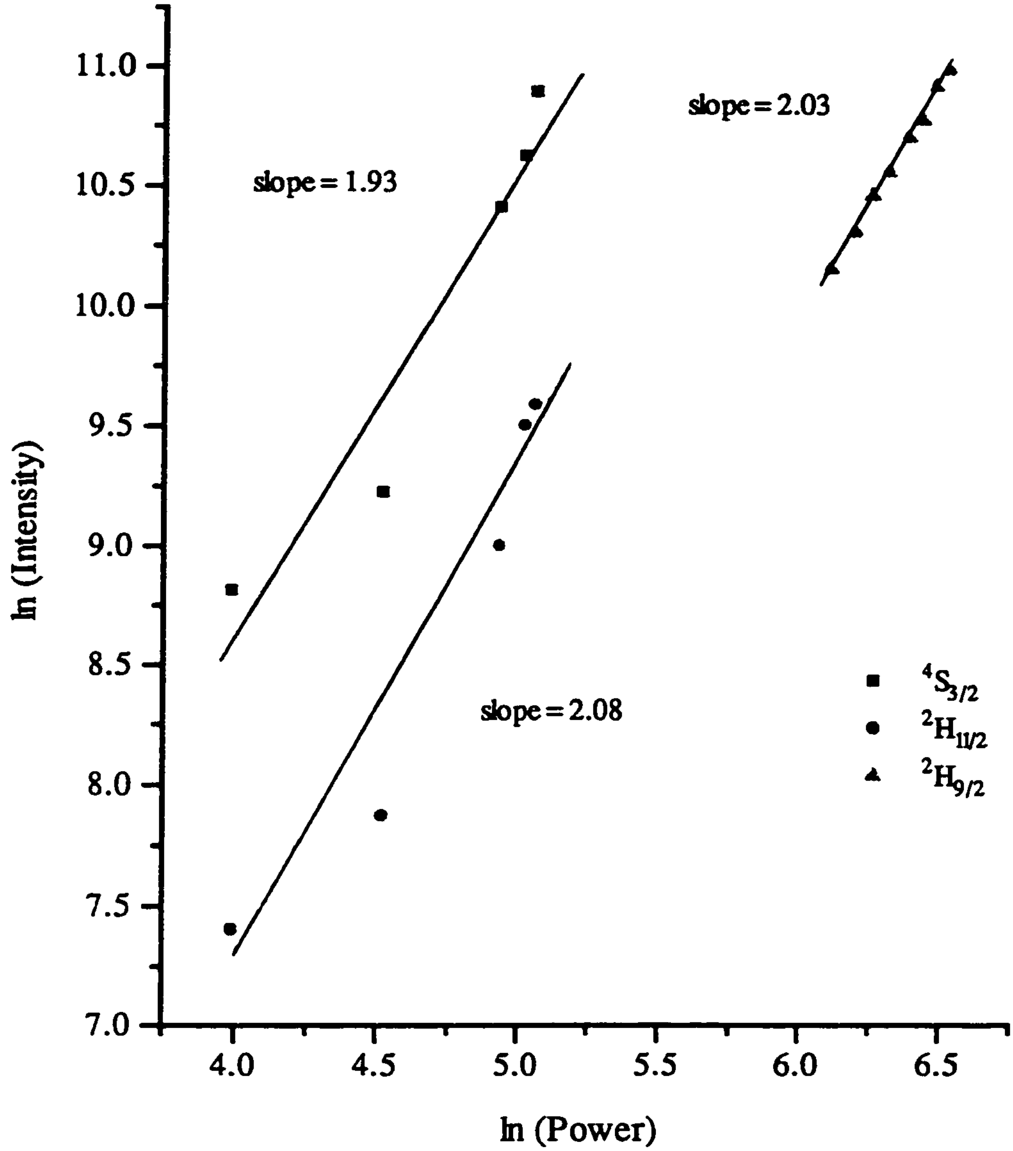

Figure 4.6.2.5 : Upconversion emission intensities versus excitation power in Er^{3+}:YVO_4 crystals upon 799.1 nm excitation.

following transitions, $^2H_{11/2} \rightarrow {}^4I_{15/2}$, $^4S_{3/2} \rightarrow {}^4I_{15/2}$, and $^2H_{9/2} \rightarrow {}^4I_{13/2}$, were fitted using linear regression and the slopes were calculated to be 2.1, 1.9, and 2.0, respectively, indicating that the absorption of two photons is necessary for upconversion to occur, which is in agreement with the pathways proposed above.

4.6.3 Excitation into the $^4I_{11/2}$ level

Continuous wave excitation (979 nm) into the $^4I_{11/2} \leftarrow {}^4I_{15/2}$ transition, using an excitation power of 300 mW, produced the fluorescence spectra shown in Figure 4.6.3.1. The observed bands were assigned to the following transitions; $^2H_{11/2} \rightarrow {}^4I_{15/2}$ transition centered at 524 nm, $^4S_{3/2} \rightarrow {}^4I_{15/2}$ transition centered at 553 nm, $^2H_{9/2} \rightarrow {}^4I_{13/2}$ transition centered at 580 nm, $^4F_{9/2} \rightarrow {}^4I_{15/2}$ transition centered at 660, and $^4I_{9/2} \rightarrow {}^4I_{15/2}$ transition centered at 800 nm. A concentration dependence of the upconverted emission signal was observed (Figure 4.6.3.1). The emission signal was maximum for the 2.5% Er^{3+} doped crystal, and decreased as the concentration decreased.

The spectral band shapes and positions observed for the upconverted fluorescence are identical to the ones observed in the fluorescence spectrum upon 488 nm excitation (Fig. 4.6.3.2), however the intensities are significantly different.

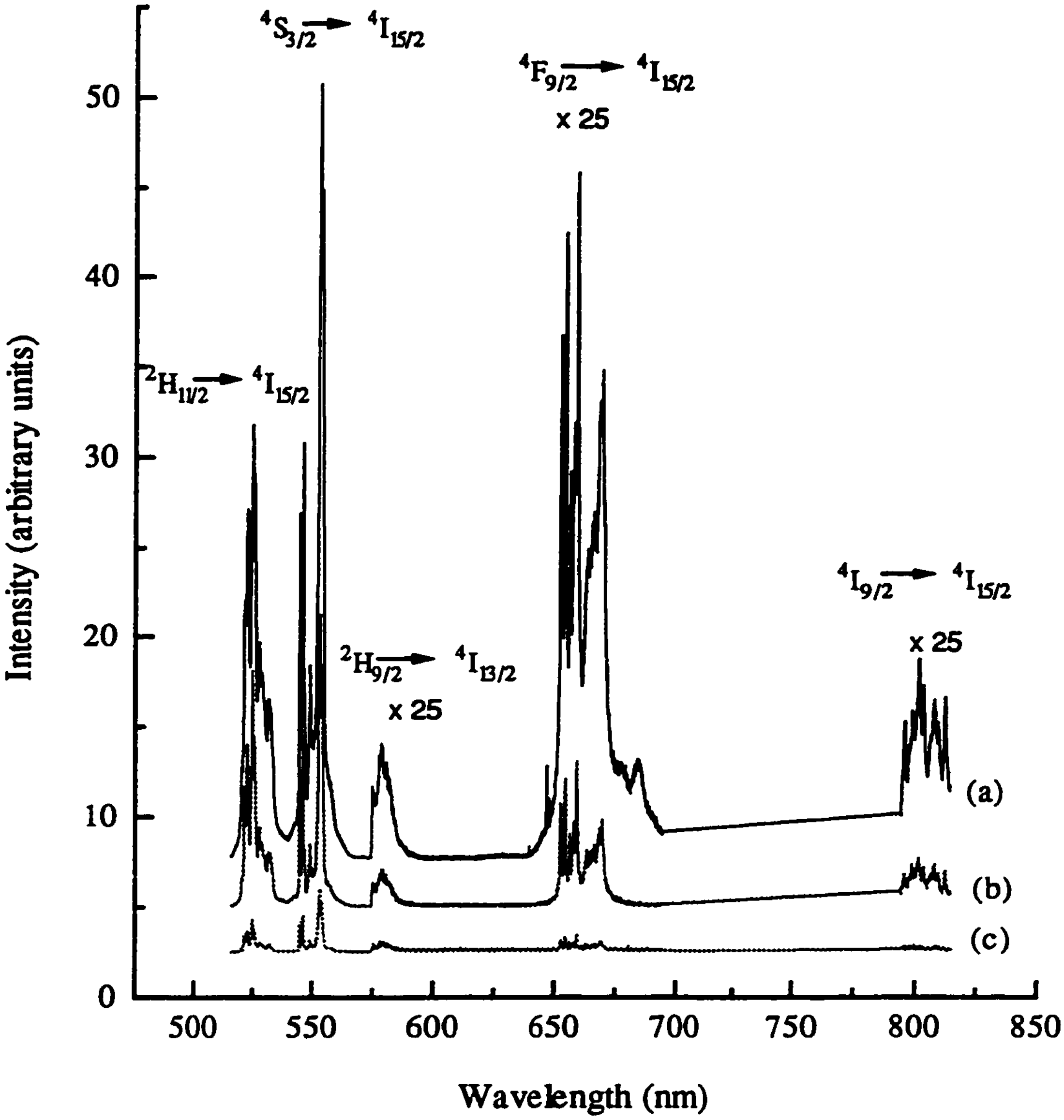

Figure 4.6.3.1 : Room temperature fluorescence spectra of a) 2.5%, b) 1.0%, and c) 0.1% Er^{3+}:YVO_4 crystals following 979 nm excitation (Excitation power = 300 mW).

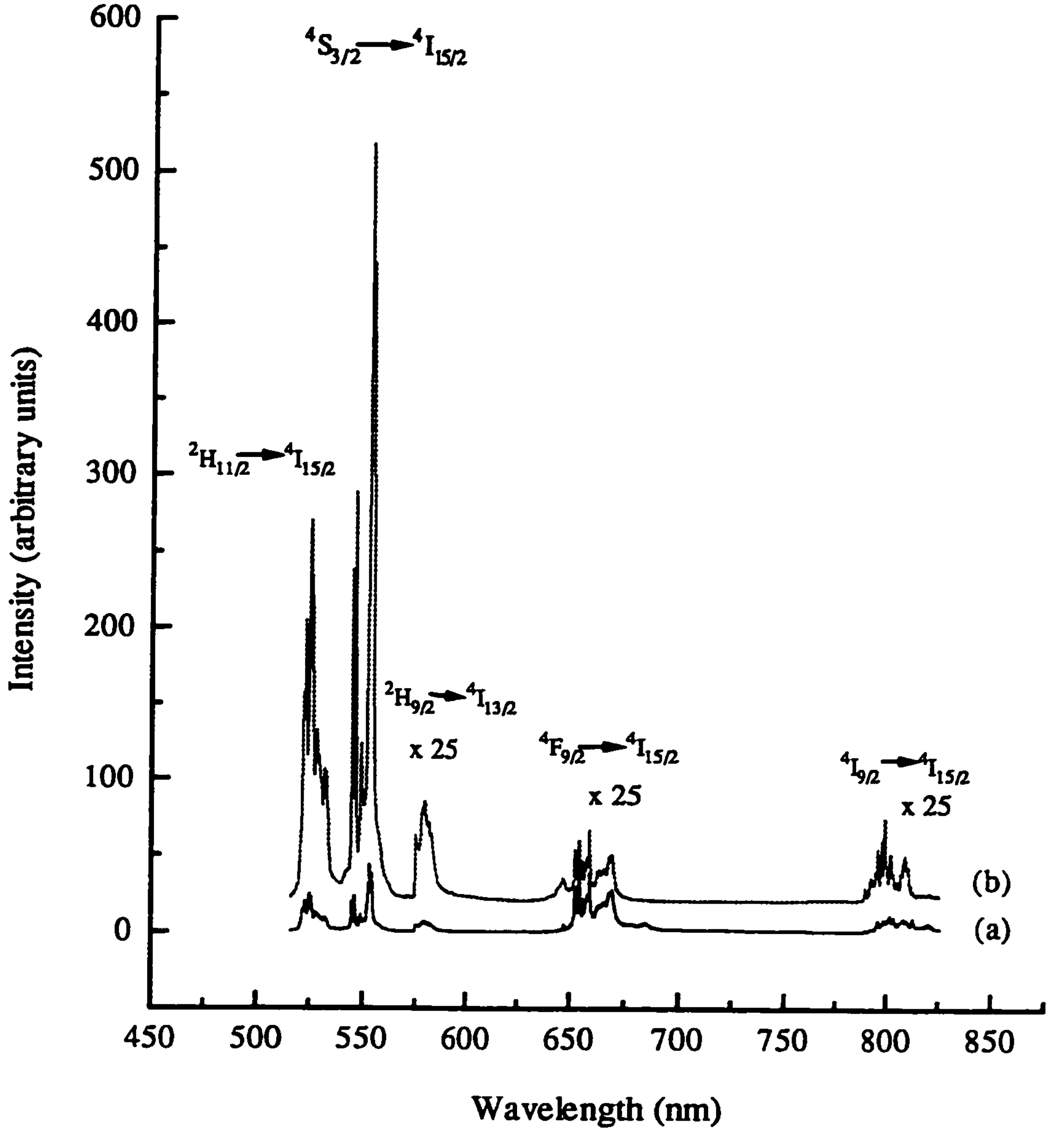

Figure 4.6.3.2 : Room temperature fluorescence spectra of a 2.5% Er^{3+} doped YVO_4 crystal following a) 979 nm and b) 488 nm excitation.

The de-excitation pathways are the same for both excitations, however the mechanism of upconversion is not as efficient in populating the excited states.

The upconversion process involves the absorption of infrared radiation at 979 nm by Er^{3+} ions,

$$^4I_{15/2} \rightarrow {}^4I_{11/2}$$

The Er^{3+} ions in the $^4I_{11/2}$ could radiatively and/or non-radiatively decay to the lower lying $^4I_{13/2}$ and $^4I_{15/2}$ states [52-55] , or they could be further excited into the upper levels via energy transfer from an adjacent Er^{3+} ion or by a sequential step-by-step absorption of photons. Evidence of the former processes was obtained by the observation of a rise time for the $^4S_{3/2}$ level. Upconversion was observed at low concentrations of Er^{3+} which indicates that it is a result of a sequential absorption of two or more photons. This allows us to conclude that the two processes are occuring. The relative fluorescence intensities of the emission green to red also change with concentration. The green fluorescence is 152 times more intense than the red fluorescence in the 0.1% Er^{3+} doped crystal in comparison to only 38 times in the 2.5% Er^{3+} doped crystal. This difference in the relative intensities, and the increase in green and red fluorescences must, therefore, result from energy transfer between excited ions [45].

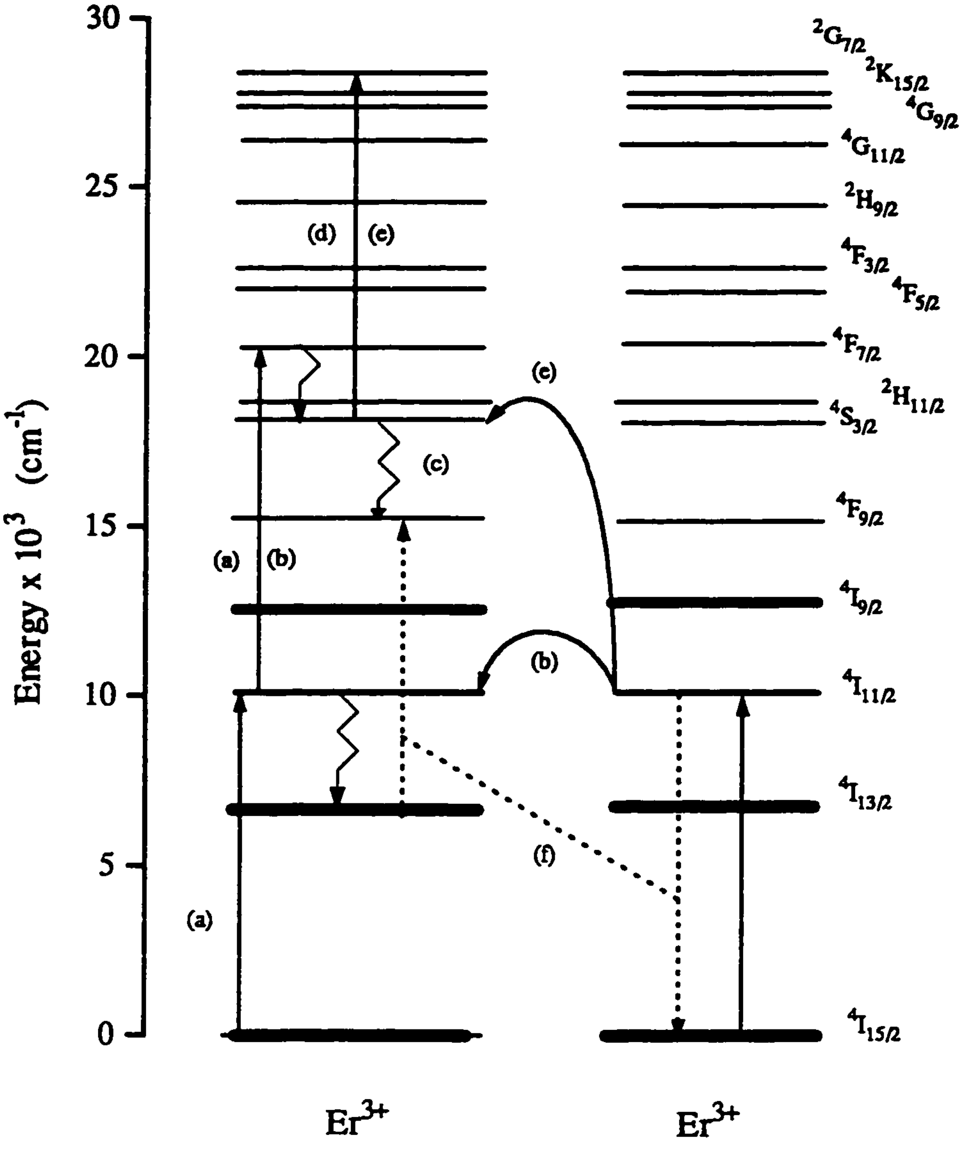

Figure 4.6.3.3 : Energy level diagram and schematic representations of the upconversion processes in YVO_4:Er^{3+}, a&d) Sequential absorption of photons, e,b&f) energy transfer, c) non-radiative decay

The mechanisms of excitation of the $^2H_{11/2}$ and the $^4S_{3/2}$ states may be explained as follows [31]: One process involves the population of the $^4F_{7/2}$ level via a sequential absorption of another photon by the same Er^{3+} (Fig. 4.6.3.3a) [39], of the type

$$^4I_{11/2} + h\nu \rightarrow {}^4F_{7/2}$$

where the resonant absorption from the ground state to the metastable $^4I_{11/2}$ state, is followed by an off-resonant absorption to the $^4F_{7/2}$ state. The mismatch between the excitation energy ($h\nu = 10214\ cm^{-1}$) and the separation between the lowest Stark levels of the $^4F_{7/2}$ and $^4I_{11/2}$ manifolds ($10250\ cm^{-1}$) is equal to $36\ cm^{-1}$. This mismatch can be compensated for by the absorption of phonons available to the lattice. Several other Stark-level combinations require even smaller phonon-energy dissipation for this upconversion process, where the mismatch is much smaller if we consider the other Stark components of the $^4I_{11/2}$ manifold.

The $^4F_{7/2}$ may be also populated via a resonant energy transfer from an adjacent Er^{3+} ion of the type (Fig 4.6.3.3b) [55-57],

$$^4I_{11/2} + {}^4I_{11/2} \rightarrow {}^4F_{7/2} + {}^4I_{15/2}$$

Both the energy transfer upconversion process and the sequential two photon absorption process are possible, due to the relatively long lifetime of the $^4I_{11/2}$ manifold (≈ 31 μs). This intermediate state acts as a reservoir for pump excitation and continues to feed the upper excited levels, such as the $^4F_{7/2}$ level. The same mechanism was shown to produce intense green fluorescence in Er:YLiF$_4$ [47, 58-59], and a less intense one in Er:YAG [55]. Once the ions are in the $^4F_{7/2}$ manifold they could cascade non-radiatively to the $^2H_{11/2}$ and the $^4S_{3/2}$ levels, to produce green emission.

The red emission band at 660 nm is attributed to the $^4F_{9/2} \rightarrow {}^4I_{15/2}$ transition, and can be populated via three main excitation routes [60-62].

i) This route corresponds to the deexcitation of the $^4S_{3/2}$ down to the $^4F_{9/2}$ level, through multiphonon interaction (Fig 4.6.3.3c).

ii) A sequential absorption of a third photon by the same Er^{3+} ion could further excite the ions in the $^4S_{3/2}$ level to the upper $^2G_{7/2}$ level (Fig 4.6.3.3d) [63],

$$^4S_{3/2} + h\nu \rightarrow {}^2G_{7/2}$$

or (iii) an energy transfer from an adjacent Er^{3+} ion (Fig 4.6.3.3e),

$$^4I_{11/2} + ^4S_{3/2} \rightarrow ^2G_{7/2} + ^4I_{15/2}$$

can populate the upper lying $^2G_{7/2}$ level. Both mechanisms, sequential absorption of a third photon or energy transfer, are non-resonant. The energy mismatch between the $^4S_{3/2}$-$^2G_{7/2}$ (9685 cm^{-1}) and the excitation wavelength (10214 cm^{-1}) is 529 cm^{-1} and may be compensated for by the emission of phonons. Ions in the $^2G_{7/2}$ state could non-radiatively decay to the lower lying levels, hence populating the $^4S_{3/2}$ and $^4F_{9/2}$ levels, from which green and red fluorescence is observed, respectively.

Previously, Van Uitert et al [64] proposed that in Y_3OCl_7 phosphors, the $^4F_{9/2}$ state is populated via the same mechanism that is proposed above. Their conclusion was based on the fact that the red emission intensity from the $^4F_{9/2}$ level tends to increase with a cubic power dependence, whereas the green emission from the $^2H_{11/2}$ and $^4S_{3/2}$ levels tends to show a quadratic dependence. In our case the red emission shows a quadratic power dependence, which renders route "i" the favorable one (Fig 4.6.3.3c). However, the observation of the green fluorescence centered at 580 nm due to the $^2H_{9/2} \rightarrow ^4I_{13/2}$ transition , enforces the presence of route "ii" ions (Fig 4.6.3.4 d&e) to populate the higher energy levels of the Er^{3+}.

The $^4F_{9/2}$ level may be also populated via cross relaxation involving one ion in the $^4I_{11/2}$ level and another in the $^4I_{13/2}$ level [39,57]

$^4I_{11/2} \rightarrow {}^4I_{13/2}$	non-radiative decay
$^4I_{11/2} + {}^4I_{13/2} \rightarrow {}^4F_{9/2} + {}^4I_{15/2}$	transfer from adjacent Er^{3+} ion

The energy transfer involves the simultaneous emission of phonons to compensate for the fairly large mismatch of energy (1383 cm^{-1}) (Fig 4.6.3.3f) which requires the emission of at least two phonons to bridge this gap.

The power dependence of the four upconverted fluorescence band intensities was investigated. It can be shown that the green fluorescence due to the $^2H_{11/2}$, $^4S_{3/2} \rightarrow {}^4I_{15/2}$ transitions and the red due to $^4F_{9/2} \rightarrow {}^4I_{15/2}$ transition, have a quadratic (slope; 2.1, 1.9, and 2.2, respectively) dependence on excitation intensity (Figure 4.6.3.4). Indicating that the upconversion process involves a two-photon mechanism. On the other hand, the green fluorescence due to the $^2H_{9/2} \rightarrow {}^4I_{13/2}$ transition has a cubic (slope 2.9) dependence on excitation power, showing the presence of a three- photon absorption mechanism [63], in agreement with the mechanisms proposed above.

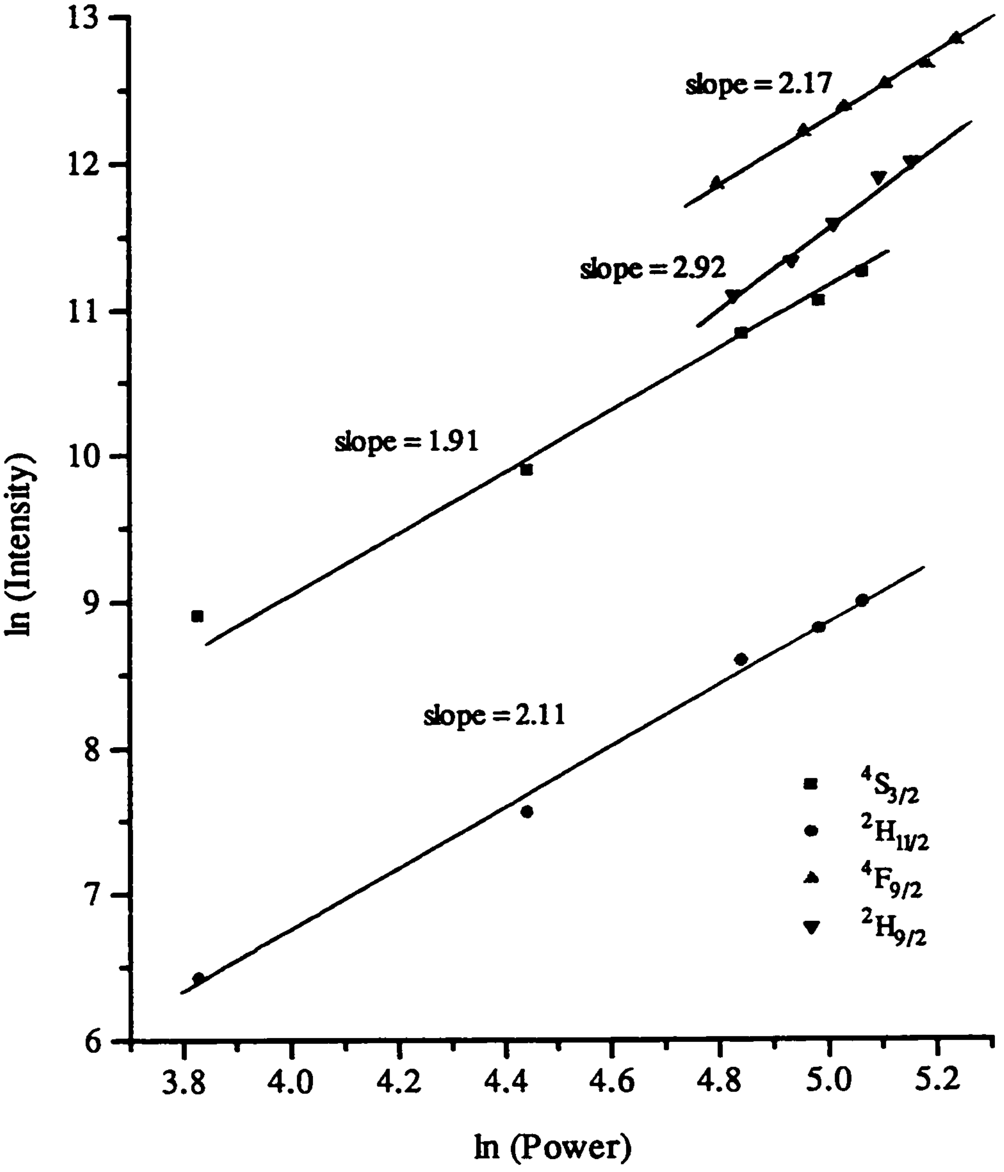

Figure 4.6.3.4 : Upconversion emission intensities versus excitation power in Er^{3+}:YVO_4 crystals upon 979 nm excitation.

4.7 FLUORESCENCE DYNAMICS OF YVO_4:Er^{3+}

In this section we will present the analysis of the time evolution of the optical transitions observed under different excitations. Room temperature measurements were performed on the YVO_4 crystals doped with 0.1, 1.0, 2.5 and 10% Er^{3+} ions. Data from the fluorescence of the various states, $^4G_{9/2}$, $^2H_{9/2}$, $^4S_{3/2}$, $^4F_{9/2}$, $^4I_{9/2}$, $^4I_{11/2}$, and $^4I_{13/2}$, yielded information about the dynamics of the system and, in particular about the optical deexcitation processes occurring between these energy levels. The samples were also excited directly into the $^2H_{11/2}$ level, which is in thermal equilibrium with the $^4S_{3/2}$ level, at 532 nm. The fluorescence decays were monitored at 1.24 μm ($^4S_{3/2} \rightarrow {}^4I_{11/2}$), 858 nm ($^4S_{3/2} \rightarrow {}^4I_{13/2}$), 1.35 μm ($^4G_{11/2} \rightarrow {}^2H_{11/2}$), 1.08 μm ($^2H_{9/2} \rightarrow {}^4F_{9/2}$), 1.14 μm ($^4F_{9/2} \rightarrow {}^4I_{13/2}$), 1.0 μm ($^4I_{11/2} \rightarrow {}^4I_{15/2}$), 800 nm ($^4I_{9/2} \rightarrow {}^4I_{15/2}$), and 1.53 μm ($^4I_{13/2} \rightarrow {}^4I_{15/2}$) (Table 4.7.1).

Normally an excited state of an isolated ion decays exponentially with a certain lifetime, τ, and the rate of decay, τ^{-1}, generally contains both the radiative and non-radiative components. At low dopant concentration the Er^{3+}-Er^{3+} interactions can be neglected, therefore the fluorescence decay curves will be exponential. Exponential decay curves were observed for the 0.1% Er^{3+} doped YVO_4 crystal. At higher concentrations of Er^{3+} ions, the interaction amongst them increases, and the interactions between dopant ions become more important. The

Table 4.7.1 : Experimental room temperature fluorescence time constants upon 532 nm excitation.

Transition		Er^{3+} ion concentration			
		0.1 %	1.0 %	2.5%	10 %
$^4S_{3/2} \to {}^4I_{11/2}$	τ	10.0 µs	9.8 µs	6.7 µs	1. 6 µs
(1.24 µm)	τ_{Rise}	0.17 µs	0.35 µs	0.39 µs	0.54 µs
$^4S_{3/2} \to {}^4I_{13/2}$	τ	10.5 µs	9.8 µs	6.4 µs	1.5 µs
(858 nm)	τ_{Rise}	0.51 µs	0.35 µs	0.39 µs	0.57 µs
$^4G_{11/2} \to {}^2H_{11/2}$	τ	5.7 µs	4.2 µs	7.2 µs	2.0 µs
(1.35 µm)	τ_{Rise}	0.38 µs	0.40 µs	0.42 µs	0.46 µs
$^2H_{9/2} \to {}^4F_{9/2}$	τ	60.0 µs	70.8 µs	53.5 µs	26.2 µs
(1.08 µm)	τ_{Rise}	0.34 µs	0.33 µs	0.35 µs	0.41 µs
$^4F_{9/2} \to {}^4I_{13/2}$	τ	6.8 µs	9.9 µs	7.8 µs	3.9 µs
(1.14 µm)	τ_{Rise}	0.34 µs	0.40 µs	0.52 µs	0.58 µs
$^4I_{11/2} \to {}^4I_{15/2}$	τ	26.6 µs	31.3 µs	31.7 µs	38.0 µs
(1.0 µm)	τ_{Rise}	12.05 µs	8.42 µs	5.61 µs	1.64 µs
$^4I_{9/2} \to {}^4I_{15/2}$	τ	----	9.5 µs	6.2 µs	1.5 µs
(800 nm)	τ_{Rise}	----	0.37 µs	0.29 µs	0.48 µs
$^4I_{13/2} \to {}^4I_{15/2}$	τ	2.29 ms	3.0 ms	2.40 ms	1.35 ms
(1.53 µm)	τ_{Rise}	35.7 µs	32.0 µs	27.7 µs	19.4 µs

theory which takes this into account has been developed by several authors [65-68]. Donor-donor interactions cause a deviation from exponentiality in the fluorescence decay curves. The degree of non-exponentiality increases with increasing concentration of the dopant. In-depth analysis of the experimental results, allows us to make several remarks with respect to crystals containing Er^{3+} $\geq 1\%$; i) all the decay curves are non-exponential, and ii) the decay times are considerably shorter in comparison to the weakly doped sample. Hence, the dynamics are now influenced by energy transfer processes and the decay times represent the decay time constants of the fluorescence curves, and not the real lifetimes of the levels. The primary deexcitation processes as well as the energy transfer probabilities and the decay constants of the emitting levels are determined by fitting the curves to the appropriate model.

Multiple phonons of only one frequency are assumed to be involved in the relaxation, that is the highest frequency for which the phonon density of states is significant. Weber [10] and Riseberg and Moos [69] showed experimentally that the probability of the relaxation transition between J-manifolds depends exponentially on the energy gap to the lower level. Theoretical treatment of various multiphonon processes such as relaxation transiton and phonon assisted energy transfer for the rare earth ions in crystals have been performed by Miyakawa and Dexter [70]. They showed that at low temperatures, the lowest-order process, involving the smallest number of phonons to span the energy gap, is the most probable.

The rate for non-radiative relaxation between two states separated by an energy gap, ΔE, which is considerably greater than the energy of a single phonon is given by [10,30,69-71]

$$W_{NR} = C\,e^{-\alpha \Delta E} \qquad 4.7.1$$

where W_{NR} is the multiphonon emission rate, and C and α are constants characteristic of a given material at low temperature [71]. The constant C increases with increasing ion-lattice coupling, and α decreases with increasing effective-phonon energy. This law has been found to hold under most conditions for non-radiative relaxations of rare earth ions, and fails when the energy gap is less than double the effective single phonon energy.

The calculated radiative rates, τ_R, given in Table 4.3.5 may be used in conjunction with the experimental fluorescence lifetimes of the different excited levels, τ_i, at low temperatures (Table 4.7.2), to examine the effect of nonradiative multiphonon processes. By assuming negligible energy transfer, it can be shown that

Table 4.7.2 : Fluorescence lifetimes measured in YVO_4: 1.0% Er^{3+} direct excitation into the upper emitting levels.

	Lifetimes	
Emitting level	77 K	300 K
$^4S_{3/2}$	17. 7 μs	9.8 μs
$^4F_{9/2}$	11.0 μs	≤ 0.5 μs
$^4I_{9/2}$	--------	≤ 0.5 μs
$^4I_{11/2}$	41. 7 μs	27 μs

$$\frac{1}{\tau_i} = \frac{1}{\tau_R} + W_{NR} \qquad 4.7.2$$

From the calculated values of the radiative lifetimes τ_R and the effective experimental τ_i, the W_{NR} values were calculated for the levels ${}^4F_{9/2}$, ${}^4S_{3/2}$ and ${}^4I_{11/2}$. The energy gaps, ΔE, between the levels involved and their corresponding next lower level are, 3090 cm^{-1} (${}^4S_{3/2}$ - ${}^4F_{9/2}$), 2750 cm^{-1} (${}^4F_{9/2}$ - ${}^4I_{9/2}$) and 3570 cm^{-1} (${}^4I_{11/2}$ - ${}^4I_{13/2}$). In Figure 4.7.1 W_{NR} is plotted as a function of the gap ΔE for YVO_4, Y_2SiO_5 [13], and $YAlO_3$ [27]. A linear fit of ln W_{NR} against ΔE yields for YVO_4

$$C = 5.61 \times 10^6 \ s^{-1}$$

and

$$\alpha = 1.52 \times 10^{-3} \ cm$$

The multiphonon transition rates in YVO_4 were found to be comparable to those that have been reported for Y_2SiO_5, however they were much larger than found for $YAlO_3$. We also observed that they were the least sensitive to the energy gap variation (Fig. 4.7.1). The data for very small and large energy gaps produce significant uncertainties, in the value of W_{NR}. Although not quantitatively useful, these values may be used to demonstrate the overall trend.

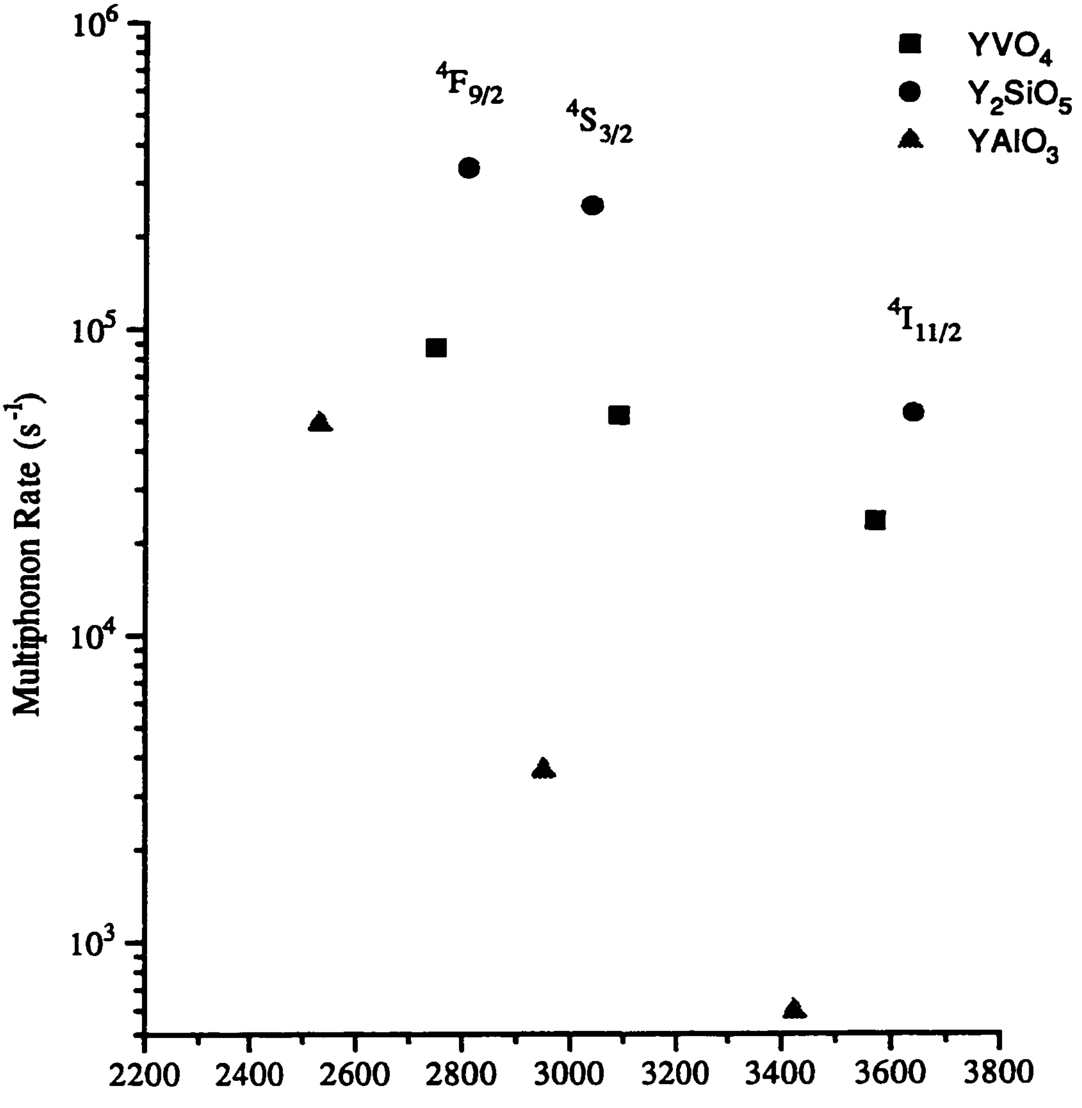

Figure 4.7.1 : Dependence of the rate of multiphonon emission on the energy gap, ΔE, to the next lower level for excited states of Er^{3+} ions in YVO_4 , Y_2SiO_5 [13], and $YAlO_3$ [27].

The multiphonon rates of the $^4S_{3/2}$ state for 1.0% Er^{3+} in YVO_4 are shown in Figure 4.7.2 as a function of temperature. Our results agree with those reported by Reed and Moos [72], where a small increase in W_{NR} appears in the temperature range 4K to 75K. This increase may be attributed to the thermal population of the higher $^4S_{3/2}$ Stark level. The rapid rise in W_{NR} as the temperature increases between 100 and 300 K may be attributed to the low-energy phonons. This is a reasonable conclusion considering the fact that the splitting of the $^4S_{3/2}$ level is 5 cm^{-1}, therefore the increase in W_{NR} above 100 K cannot be attributed to thermal population.

4.7.1 $^4I_{13/2}$ Fluorescent Decay

The fluorescence lifetime of the $^4I_{13/2}$ level has been found to be dependent on the Er^{3+} concentration. On the other hand the Judd-Ofelt analysis suggests that the radiative transition probabilities from the $^4I_{13/2}$ level are independent of concentration and equal to 2.3 ms (Table 4.3.5). The calculated value compares extremely well with the experimental value of 2.35 ms obtained for the 0.1% Er^{3+} doped YVO_4 crystal following 653 nm excitation at room temperature. This leads to the conclusion that the de-excitation of the $^4I_{13/2}$ level at low activator concentration is essentially radiative ($W_r \approx 1/\ \tau_{(^4I_{13/2})}$) (Figure 4.7.1.1 route a). As

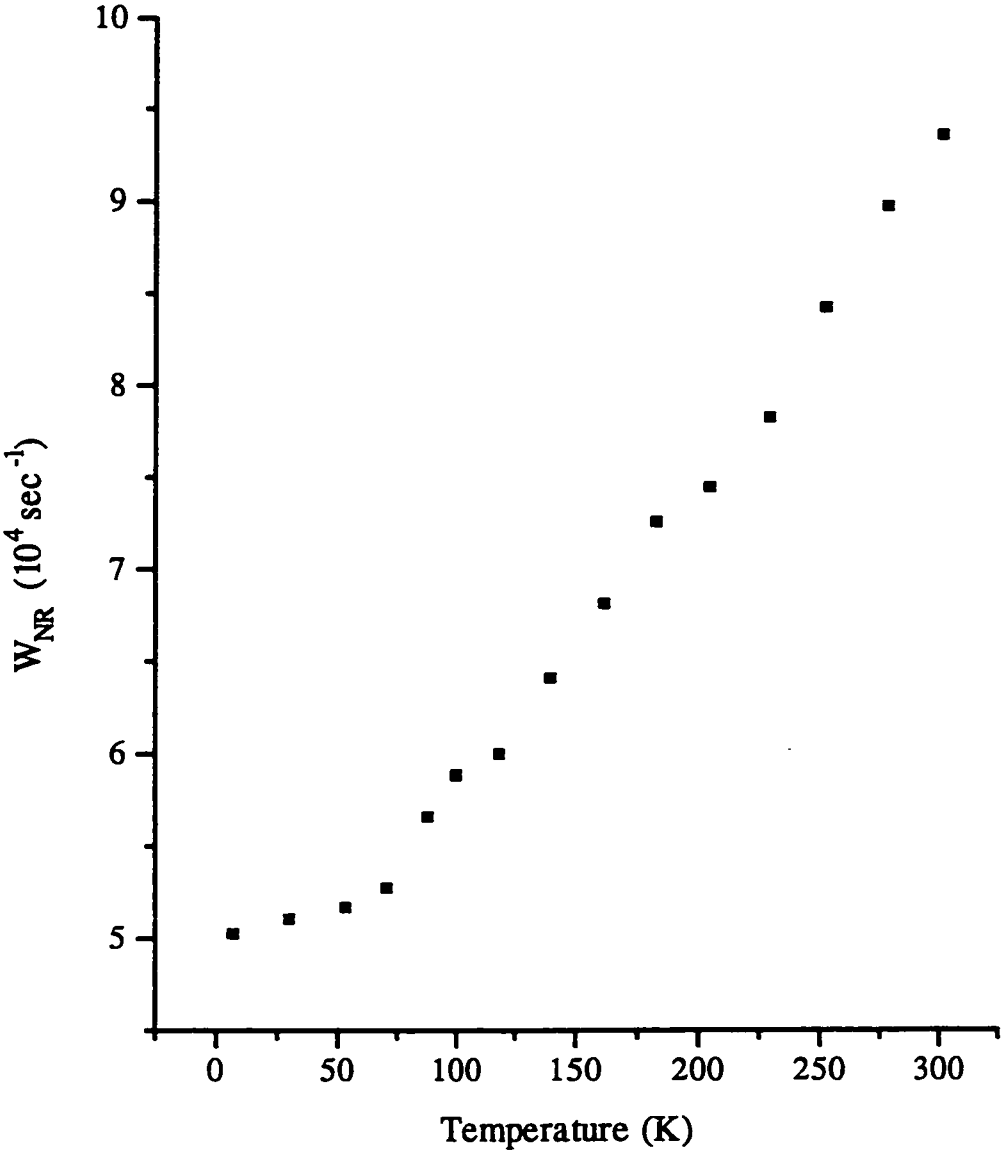

Figure 4.7.2 : Temperature dependence of the multiphonon transition-rate of the $^4S_{3/2}$ state for 1.0% Er^{3+} in YVO_4.

the concentration of Er^{3+} is increased to 1.0% and 2.5% Er^{3+}, the fluorescence lifetimes of the $^4I_{13/2}$ level increases (Table 4.7.1). Similar behavior was observed in other systems such as $YAlO_3$:Er^{3+}[27], and LaF_3:Er^{3+}[10] and was attributed to experimental errors. However Rubin et al [73] attributed this behavior to radiative energy transfer or trapping. The authors expressed the total fluorescence lifetime as follows;

$$\tau_F^{-1} = \tau_R^{-1} + W_{NR} + W_{UP} - E_{TR} \qquad 4.7.1.1$$

where τ_R^{-1} is the radiative transition probability, W_{NR} the nonradiative emission rate, W_{UP} the up-conversion energy transfer rate which always interferes in the highly doped Er^{3+} systems, and W_{TR} represents the radiative energy transfer rate which is described by a negative sign to account for the lengthening of the apparent fluorescence lifetime due to the trapping of the emitted photon. In the case of higher concentrations of Er^{3+} (1.0 and 2.5%), both radiative trapping and up-conversion energy transfer are strong and the net result is an increase in the apparent lifetime (Figure 4.7.1.1 route b). The fluorescence lifetime of the same level begins to decrease as the concentration is increased further to 10% Er^{3+}, where it was measured to be 1.43 ms. This is attributed to luminescence quenching due to energy migration followed by transfer to impurities or defects (Figure 4.7.1.1 route c).

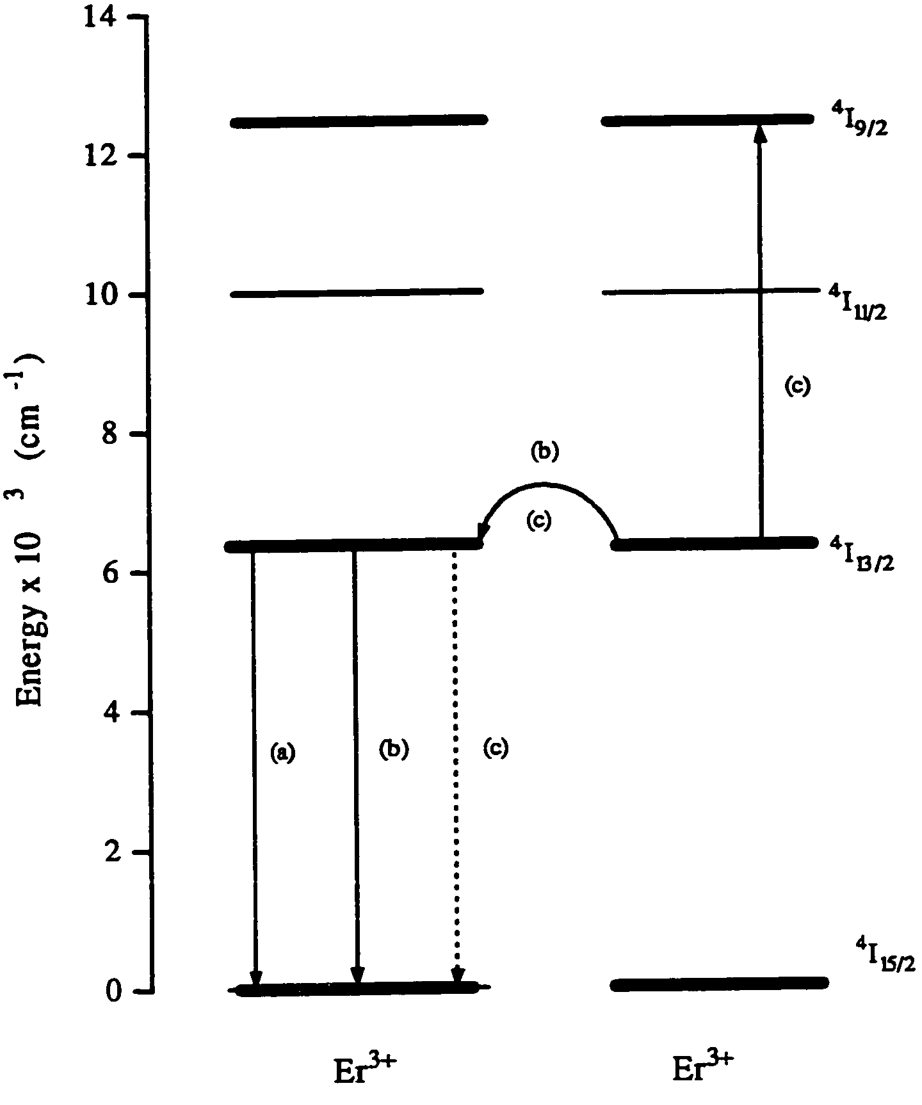

Figure 4.7.1.1 : Principal population and depopulation schemes of the $^4I_{13/2}$ level in $YVO_4:Er^{3+}$; a) Radiative decay at low erbium concentrations, b) combination of radiative decay and energy transfer at moderate erbium concentrations, c) concentration quenching.

At high Er concentrations, the Er-Er interaction probability increases. Therefore the probability of an excitation jumping to a neighbouring Er increases which in turn increases the rate of migration for an excitation through the Er sublattice. This process of migration terminates when the excitation interacts with an impurity or defect and decays back to ground state [66]. The decay curves under both excitations (532 and 653 nm) were exponential for the 0.1% Er^{3+}, indicating that energy transfer is not occurring at low dopant concentration. The decay curves start to deviate from exponentiality as the concentration of erbium is increased in the YVO_4 crystals (Fig. 4.7.1.2).

The decay curves shown in Figure 4.7.1.2 demonstrate the presence of rise times for the 1.53 μm emissions ($^4I_{13/2} \rightarrow {}^4I_{15/2}$) for the different concentrations of Er^{3+}. The rise times were measured to be 35.7, 32, 27.7, and 19.4 μs for the 0.1%, 1%, 2.5%, and 10% Er^{3+} doped YVO_4 crystals, respectively. These rise times reflect the lifetime of the $^4I_{11/2}$ level (see Table 4.7.1), which implies that the $^4I_{11/2}$ level is the principal feeding level for the $^4I_{13/2}$ state. The $^4I_{13/2}$ level is also fed radiatively from higher levels such as the $^2H_{9/2}$ and the $^4S_{3/2}$ levels, which were shown to be populated via different mechanisms including energy transfer upconversion and other cross relaxation processes (see section 4.6). Hence, an increase in erbium concentration results in an increase in the probability of the cross relaxation processes of the previously mentioned levels. This leads to an

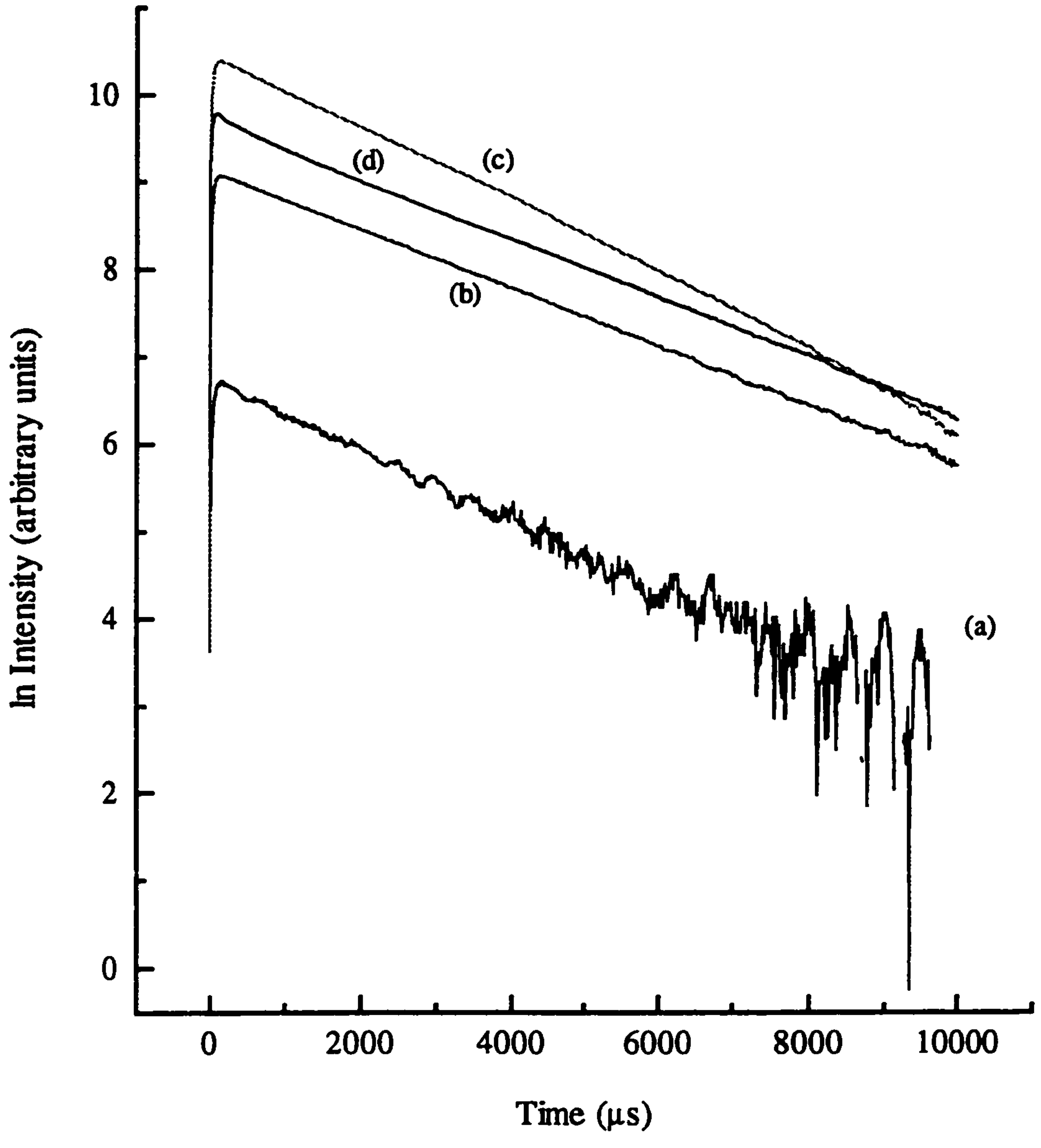

Figure 4.7.1.2 : Room temperature $^4I_{13/2}$ fluorescent decay of the various concentrations of Er^{3+} doped YVO_4 crystals a) 0.1%, b) 1.0%, c) 2.5% , and d) 10% Er^{3+} ions. λ_{Ex} = 532 nm.

increase in the number of ions reaching the $^4I_{13/2}$ without passing through the $^4I_{11/2}$ level [71], which explains the decrease in the rise time of the $^4I_{13/2}$ level with an increase in concentration (Table 4.7.1).

4.7.2 $^4I_{11/2}$ Fluorescent Decay

The behaviour of the $^4I_{11/2}$ level is slightly different than that of the $^4I_{13/2}$ level. The room temperature fluorescent decay constants were measured, following 653 nm excitation, to be 26.4, 27.1, 26.9, 28.0 µs for the 0.1%, 1%, 2.5% and 10% Er^{3+} doped YVO_4 crystal, respectively. The rise times of the $^4I_{11/2}$ level were also measured and found te be equal to 0.6, 0.5, 0.6, and 1.6 µs, respectively. These rise times were of the same order as the decay time of the $^4I_{9/2}$ level, except for the 10% sample where the rise time was much longer than the decay time of the $^4I_{9/2}$ level (≤ 0.5 µs). The aforementioned results leads to the conclusion that the $^4I_{11/2}$ level is mainly fed by the $^4I_{9/2}$ level, while at higher concentrations energy transfer upconversion processes, such as

$$^4I_{9/2} + {}^4I_{9/2} \rightarrow {}^4I_{13/2} + {}^4S_{3/2}$$

dominate, which makes the $^4S_{3/2}$ level as the main feeding level. As a result, the rise time of 1.6 μs for the $^4I_{11/2}$ level is exactly the same as the decay time of the $^4S_{3/2}$ level (1.6 μs) following 653 nm excitation at room temperature, in the 10% Er^{3+} doped YVO_4 crystal.

The fluorescence lifetimes for the $^4I_{11/2}$ level in Er^{3+} doped YVO_4 do not vary significantly with a change in the Er^{3+} concentration. This suggests that the radiative energy transfer processes involving the $^4I_{11/2}$ level are not efficient and the non-radiative multiphonon relaxations dominate. The same observation has been reported for Er^{3+} doped Y_2SiO_5 [13], but not for Er^{3+} doped YAG or YLF [74].

4.7.3 $^4I_{9/2}$ Fluorescent Decay

The $^4I_{9/2}$ level exhibits a very short lifetime due to rapid depopulation to the nearby $^4I_{11/2}$ level lying at 2332 cm^{-1} below the $^4I_{9/2}$ level. To bridge this energy gap a minimum of three high energy phonons (890 cm^{-1}) must be emitted. The fluorescent decay constants for this level varied slightly with concentration, and were measured to be ≈ 0.6, 0.5, 0.5, and 0.4 μs for the 0.1%, 1%, 2.5%, and 10% Er^{3+} doped YVO_4 crystals, respectively, following 653 nm excitation at room temperature. Analysis of the fluorescence decay curves showed an exponential decay for the 0.1% Er^{3+} sample, and a non-exponential decay for higher concentrations.

A rise time of the order of 0.4 μs was also observed for all of the samples, which is longer than the duration of the excitation pulse (15 ns). If the fluorescence were excited via a stepwise absorption process, there would be no reason for fluorescence intensity to continue rising after disappearance of the pump pulse. On the other hand, the rise time of the $^4I_{9/2}$ level is of the same order as the decay time of the $^4F_{9/2}$ level (Table 4.7.4.1 page 195). Hence, the small variation in the decay times with erbium concentration, and the fast rise times, does not provide enough evidence to distinguish between a sequential photon absorption process and an energy transfer process which affect the main feeding $^4F_{9/2}$ level. Also the fast fluorescence decay of the $^4I_{9/2}$ level limits the transfer process and other interaction processes between adjacent erbium ions. However this interaction is not negligible and a cross-relaxation process of the following type may take place,

$$^4I_{9/2} + {}^4I_{15/2} \rightarrow 2\ {}^4I_{13/2}$$

or/and an upconversion process of the type

$$2\ {}^4I_{9/2} \rightarrow {}^4I_{13/2} + {}^4S_{3/2}$$

These processes become dominant at higher concentrations of erbium, leading to non-exponential decay curves.

4.7.4 ${}^4F_{9/2}$ Fluorescent Decay

The fluorescence decay constants of the ${}^4F_{9/2}$ level were measured to be ≈ 0.5 μs for the different Er^{3+} ion concentrations, upon direct excitation (653 nm) at room temperature. This implies that the ${}^4F_{9/2}$ state in Er^{3+} doped YVO_4 is not subject to concentration quenching. The fluorescence decay, however, was much longer upon 532 nm excitation (Table 4.7.4.1), in the order of a few micro seconds, which is the same as that of the ${}^4S_{3/2}$ level for a specific concentration (Table 4.7.1). Therefore, the ${}^4S_{3/2}$ level may be considered to be the main feeding level, through radiative, non-radiative, and cross relaxation processes (Fig 4.7.4.1).

Analysis of the fluorescence decay curves showed an exponential decay curve for the 0.1% Er^{3+} sample, while crystals doped with higher concentrations of Er^{3+} ions deviated from this exponentiality. A rise time in the order of 0.4 μs was observed in the YVO_4 crystals with the different concentrations of Er^{3+}, following resonant excitation into the $^4F_{9/2}$ level. The rise time, which is longer than the duration of the excitation pulse, indicates that an energy transfer process is taking place [75]. However, the efficiency of such an energy transfer process could be limited by the fast decay of this level.

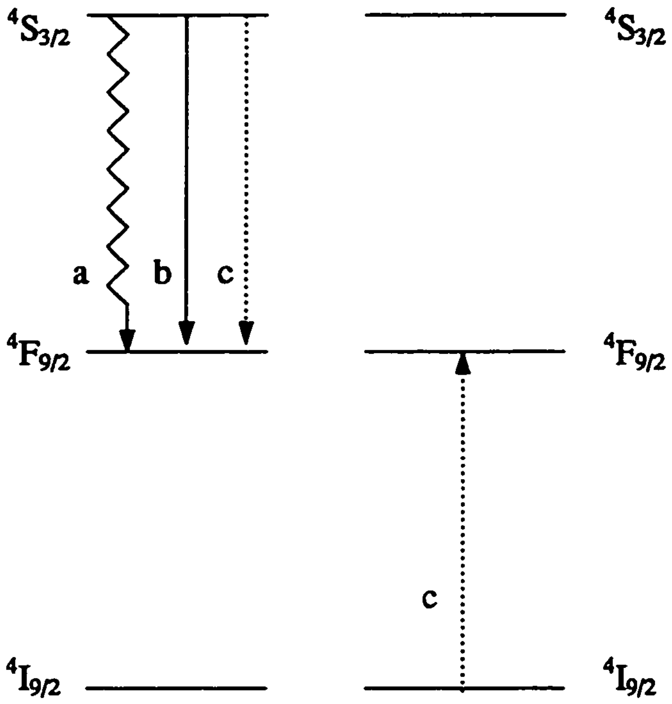

Figure 4.7.4.1 : Scheme of the different feeding mechanisms of the $^4F_{9/2}$ level via the $^4S_{3/2}$ level, a) non-radiative, b) radiative, and c) cross-relaxation.

Table 4.7.4.1 : Fluorescence decay constants of the $^4F_{9/2}$ level upon 532 nm and 653 nm excitation at room temperature of YVO_4 crystals doped with different concentrations of Er^{3+} ions.

Concentration % Er^{3+}	Decay time constant (μs) λ_{EX} = 532 nm	Decay time constant (μs) λ_{EX} = 653 nm
0.1	6.8	0.5
1.0	9.9	0.5
2.5	7.8	0.5
10	3.9	0.5

4.7.5 $^4S_{3/2}$ Fluorescent Decay

The fluorescence decay constants of the $^4S_{3/2}$ level were measured to be 10.0, 9.8, 6.7, and 1. 6 μs, for the 0.1%, 1%, 2.5%, and 10% Er^{3+} doped YVO_4 crystals upon 532 nm excitation at room temperature. Strong cross-relaxation is observed from the $^4S_{3/2}$ level, which plays an important factor in the dynamics and feeding mechanisms of the other levels of Er^{3+} in YVO_4 [76-78]. This strong relaxation explains the rapid decrease of the lifetime of this level with increasing erbium concentration. The $^4S_{3/2}$ level can be depopulated via different mechanisms such as radiative and non-radiative decay to the lower lying levels, or energy transfer to a neighbouring Er^{3+} ion. The fluorescent decay for the different concentrations of erbium, the 0.1% Er^{3+}:YVO_4 crystal exhibits non-exponential decay with an exponential tail. These findings support the theory that energy is being transferred into neighbouring ions via cross-relaxation processes. This non-exponentiality increases with an increase in concentration and will be discussed later (Fig. 4.7.5.1). The cross-relaxation processes involved are

$$^2H_{11/2} + {}^4I_{15/2} \rightarrow {}^4I_{9/2} + {}^4I_{13/2} \quad \text{(Fig. 4.7.5.2a)}$$

and

$$^2H_{11/2} + {}^4I_{15/2} \rightarrow {}^4I_{13/2} + {}^4I_{9/2} \quad \text{(Fig. 4.7.5.2b)}$$

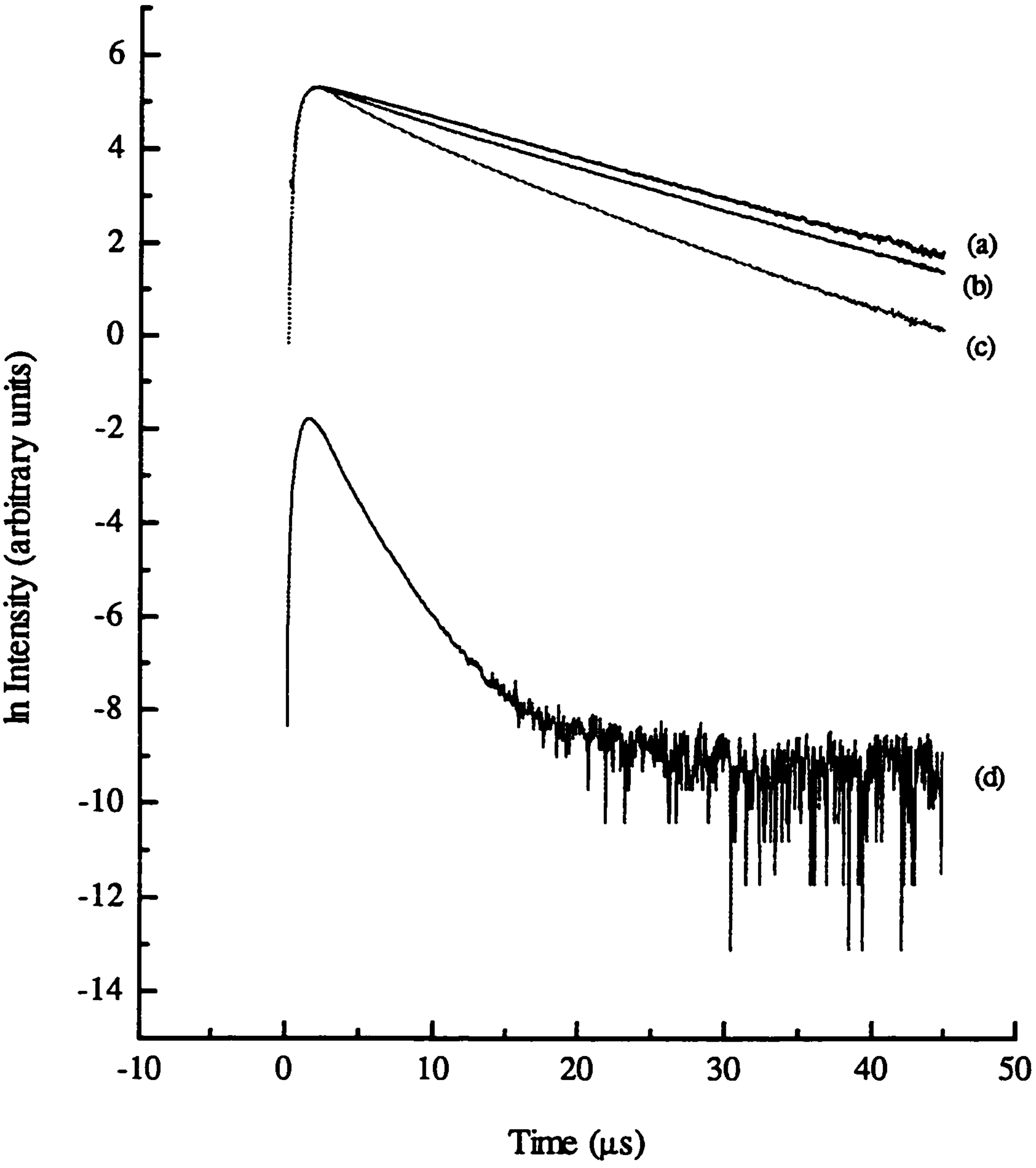

Figure 4.7.5.1 : Room temperature $^4S_{3/2}$ fluorescent decay of the various concentrations of Er^{3+} doped YVO_4 crystals a) 0.1%, b) 1.0%, c) 2.5% , and d) 10% Er^{3+} ions. λ_{Ex} = 532 nm.

The energy mismatch for each of the above mentioned processes is 70 cm^{-1}, and requires the emission of phonon energy (Figure 4.7.5.2).

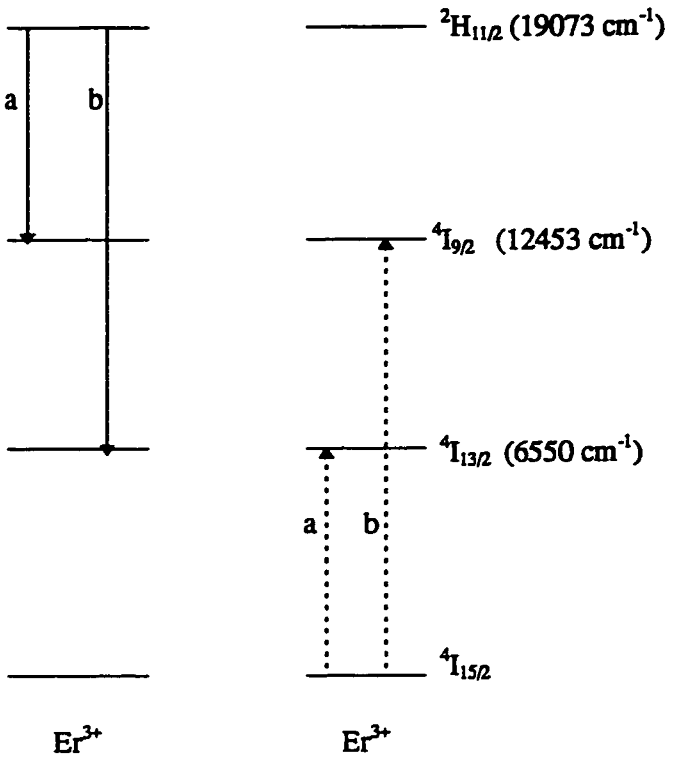

Figure 4.7.5.2 : Cross relaxation processes from the $^2H_{11/2}$ level of Er^{3+} doped YVO_4 crystals.

4.7.6 Time Dependence of the Donor Fluorescence

Ion-ion interactions which occur as the dopant concentration is increased, may lead to another type of dynamics involving the excited state of ions in a crystal. This would result in energy transfer within the active system. In the $YVO_4:Er^{3+}$ matrix both resonant and nonresonant energy transfers can occur. Nonresonant energy transfer occurs between an optically excited "donor" (D) and an unexcited "acceptor" (A), to which excitation will be transferred, with some energy mismatch. The acceptor ion may itself be an optically excited ion, in this case the energy transfer will lead to upconversion processes [31]. Transfer occurring between the same excited ions of neighbouring donors, and not leading to relaxation, is termed migration.

The likely mode of excitation transfer is a multipolar electrostatic or an exchange ion-ion relaxation process coupled to the emission or absorption of single or multiple phonons [32]. The phenomenological theory behind these transfers has been developed by Förster [65] and Dexter [66], and further refined by Inokuti and Hirayama [67]. The model proposed by Inokuti and Hirayama is used to explain the observed fluorescence behaviour in the case the transfer between the donor and acceptor is faster than the migration in the donor subset. In this model, a relationship between the macroscopic fluorescence properties and the microscopic transfer interactions is established. Therefore, detailed knowledge of the parametric dependence of the D-A transfer on interionic separation is required. The transfer rates are then averaged over the spatial distributions of the various possible donors and acceptors. The model predicts that donor luminescence decay will not be single exponential in the presence of excitation transfer from donors to acceptors. Furthermore, the shape of the decay curve will be determined by the concentration of acceptors and the way in which the donors and acceptors interact. In such calculations most quantities are treated as variables and are adjusted to provide a best fit to the experimental data.

The decay curves from the $^4S_{3/2}$ level were analyzed for the different concentrations of Er^{3+} doped YVO_4 crystals. For the 0.1% Er^{3+} crystal the decay curve was found to be exponential, and yielded a decay time of 10.5 μs. Thus, it can be concluded that there is no energy transfer at such a low concentration of dopant.

For the 1.0% Er^{3+} crystal, the decay curve is not exponential, although it approaches an exponential shape (Fig. 4.7.6.1). The decay curve can be fitted using the Inokuti-Hirayama model. The following expression is used for the electric multipolar interaction

$$\phi(t) = A \exp [-kt - \alpha(kt)^{3/s}] + B \qquad 4.7.6.1$$

where $\phi(t)$ is the emission intensity after pulsed excitation, k is the intrinsic decay constant of the donor ion involved in the energy transfer process, in the absence of the acceptor, s = 6 for dipole-dipole (D-D), 8 for dipole-quadrupole (D-Q) and 10 for quadrupole-quadrupole (Q-Q) interaction, and α contains the energy transfer probability, whilst A and B are constants. For the crystal under investigation, a good fit can be obtained for s = 6, 8 and 10, but the uncertainty on the fitting parameters becomes unacceptable for the dipole-quadrupole interactions. Moreover, none of the transitions involved in the cross relaxation mechanism

$$^2H_{11/2} + {}^4I_{15/2} \rightarrow {}^4I_{9/2} + {}^4I_{13/2}$$

occur with the quadrupolar selection rule $|\Delta J| = 2$, and therefore it is unlikely that the D-Q and Q-Q interactions dominate the transfer [79]. The fit in the case of s = 6 is shown in Figure 4.7.6.1. For the 1.0 % Er^{3+} crystal, the cross relaxation was therefore assigned to an electric dipole-electric dipole interaction, in the absence of energy migration in the thermalized ($^2H_{11/2}$, $^4S_{3/2}$) states of the donors.

From the fit, the values $\alpha = 0.176$ (±20%) and $k = 0.084\ \mu s^{-1}$ were obtained, corresponding to a lifetime of the isolated donor of 12 μs. This value is in

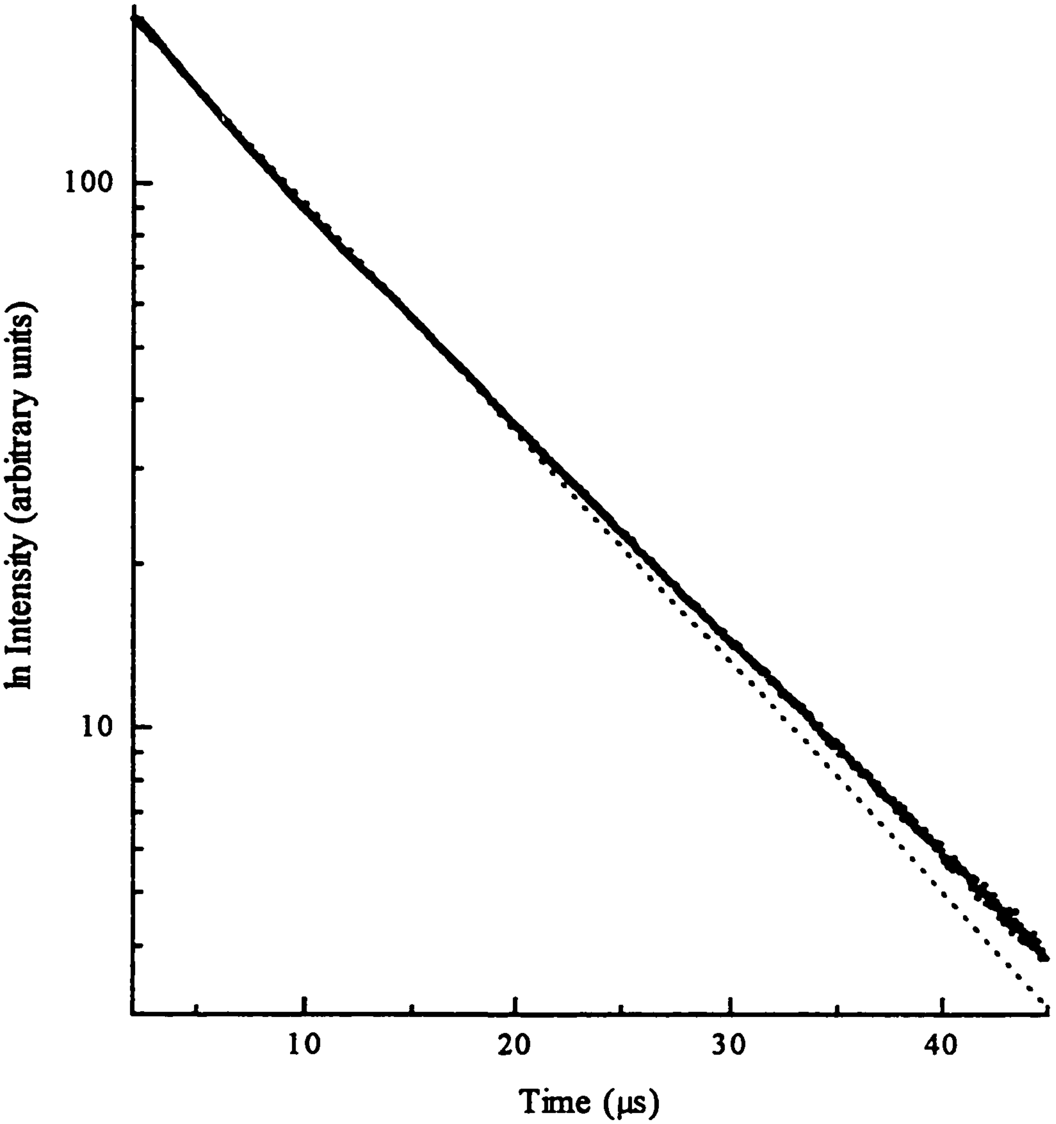

Figure 4.7.6.1 : Decay curve of the luminescence from the $^4S_{3/2}$ state in the 1.0% Er^{3+} doped YVO_4 crystal. Dotted line: exponential decay; straight line : Inokuti-Hirayama model for s = 6.

excellent agreement with the experimental value obtained at room temperature for the ($^2H_{11/2}$, $^4S_{3/2}$) states in the 0.10 % doped crystals, confirming the correctness of the Inokuti-Hirayama model. It is also corroborated by the fact that the long time tail of the decay curve is exponential giving a lifetime very close to the isolated donor ($\tau = 11\ \mu s$), as the theory predicts [80].

The parameter α can provide information on the probability of the energy transfer process, given by [80]:

$$\alpha = 4/3\ \pi\ \Gamma\,(1 - 3/s)\ N_a\ R_0^3 \qquad (4.7.6.2)$$

where s = 6 for dipole-dipole interaction, Γ is the gamma function [$\Gamma(1/2) = 1.7725$]. N_a is the concentration of the acceptor (Er^{3+}) in ions cm^{-3}, and R_0 is the critical distance defined such that for a donor-acceptor pair with separation R_0, the probability of transfer to the acceptor equals the probability of internal decay of the donor. In practice, R_0 expresses the strength of the donor-acceptor interaction. From the crystal structure and the Er^{3+} concentration, for the 1.0 % doped crystal $N_a = 1.253\times10^{20}$ ions cm^{-3}, hence $R_0 = 5.7$ Å, a value typical for energy transfer processes involving trivalent lanthanide ions [79]. From this value, the dipole-dipole coupling parameter C can be calculated, using [80]:

$$C = R_0^6\, k \qquad (4.7.6.3)$$

In the present case, $C = 2.9\times10^{-51}\ m^6s^{-1}$. This value is of the same order of magnitude as that calculated ($C = 8.3\times10^{-52}\ m^6s^{-1}$) by Watts [81] for the transfer

$$^2F_{5/2}\,(Yb^{3+}) + {}^4I_{15/2}\,(Er^{3+}) \rightarrow {}^2F_{7/2}\,(Yb^{3+}) + {}^4I_{11/2}\,(Er^{3+})$$

in LaF_3, and slightly higher than the range $C = (2\text{-}6)\times10^{-52}\ m^6s^{-1}$ obtained for the cross relaxation process of the $^5D_1$ state of Eu^{3+} in $Cs_2NaY_{1-x}Eu_xCl_6$ [82], where the cross relaxation is weaker, due to the fact that the Eu^{3+} ions lie on a center of inversion.

In the case of the 2.5 % crystal, the decay curve deviates rather strongly from an exponential shape; it can be numerically fitted to the Inokuti-Hirayama model, but the obtained parameters have no physical significance. Moreover, the long time tail does not give the decay of the isolated donor, as the Inokuti-Hirayama theory would predict. Therefore, it is possible to conclude that for this concentration the energy transfer process occurs in the presence of migration among the donors, which starts to affect the decay mechanism. This is not surprising and agrees with what has been observed for other systems [82].

For the 10 % crystal, the decay is very complex and short, and cannot be fitted using any model. This behavior is typical of systems in which the energy transfer process occurs in the so called “intermediate regime”, in which the transfer and the migration occur approximately with the same rate [81].

4.8 REFERENCES

1. S.A. Miller, H.H. Caspers, H.E. Rast, Phys. Rev., 168 (3), 964 (1968).
2. N.T. McDevitt, A.D. Davidson, J. Opt. Soc. Am., 56, 636 (1966).
3. M.M. Elcombe, A.W. Pryor, J. Phys., C3, 492 (1970).
4. C. W. Tomblin, G.D. Jones, R.W.G. Syme, J. Phys., C17, 4345 (1984).
5. J.D. Gruber, W.F. Krupke, J.M. Poindexter, J. Chem. Phys., 41, 3363 (1964).
6. C.A. Freeth, G.D. Jones, R.W.G. Syme, J. Phys., C15, 5667 (1982).
7. N.J. Cockroft, G.D. Jones, R.W.G. Syme, J. Lumin., 43, 275 (1989).
8. M.J. Weber, Phys. Rev., 171, 283 (1968).
9. B.M. Tissue, N.J. Cockroft, L. Lu, D.C. Nguyen, W.M. Yen, J. Lumin. 48-49, 477 (1991).
10. M.J. Weber, Phys. Rev., 157, 262 (1967).
11. A.A. Kaminskii, A.G. Petrosyan, G.A. Denisenko, T.I. Butaeva, V.V. Fedorov, S.E. Sarkisov, Phys. Stat. Sol. A, 71, 291 (1982).
12. J.C. Souriau, C. Borel, C. Wyon, C. Li, R. Moncorgé, J. Lumin., 59, 349 (1994).
13. C. Li, C. Wyon, R. Moncorgé, IEEE J. Quant. Elect., 28 (4), 1209 (1992).
14. W. Krupke, Phys. Rev., 145, 325 (1966).
15. M. J. Weber, T.E. Varitimos, B.H. Matsinger, Phys. Rev. B, 8, 47 (1973).

16. W.T. Carnall, P.R. Field, K. Rajnak, J.Chem. Phys., 49, 4424 (1968).

17. W.B. Fowler, D.L. Dexter, Phys. Rev., 128, 2154 (1962).

18. R. Peacock, "The Intensities of Lanthanide f↔f Transitions", in Structure and Bonding, Springer-Verlag Berlin, 22, 83 (1975).

19. C.K. Jørgensen, R.B. Judd, Mol. Phys., 8, 281 (1964).

20. D.C. Yeh, R.R. Petrin, W.A. Sibley, V. Madigou, J.L. Adam, M.J. Suscavage, Phys. Rev. B, 39 (1), 80 (1989).

21. Mc Knight, H.G. and L.R. Rothrock, U.S. Army ECOM Technical Report ECOM0022F (NTIS 761 094) (1973).

22. C.A. Morrison, R.P. Leavitt, J. Chem. Phys., 71 (6), 2366 (1979).

23. N. Karayianis, D.E. Wortman, C.A. Morrison, Harry Diamond Laboratories Report TR-1775, NTIS 040 905 (1976).

24. D. Kuse, Z. Phys., 203, 49 (1967).

25. C. Brecher, H. Samelson, A. Lempicki, R. Riley, T. Peters, Phys. Rev., 155, 178 (1966).

26. H.G. Khale, L. Klein, Phys. Stat. Sol., 42, 479 (1970).

27. M. J. Weber; Phys. Rev. B, 8 (1), 54 (1973).

28. D. C. Yeh, W. A. Sibley, M. Suscavage, M. G. Drexhage, J. Appl. Phys., 62 (1), 266 (1987).

29. M. A. Chammarro, R. Cases, J. Lumin., 46, 59 (1990).

30. M.D. Shinn, W.A. Sibley, M.G. Drexhage, R.N. Brown, Phys. Rev. B, 27, 6635 (1983).

31. F. Auzel, Proc. IEEE, 61, 758 (1973).

32. J.C. Wright, "Radiationless Processes in Molecules and Condensed Phases", edited by F.K. Fong, Topics in Applied Physics V.15, Springer-Verlag, Berlin (1976).

33. S. Tanabe, S. Yoshii, K. Hirao, N. Soga, Phys. Rev. B, 45, 4620 (1992).

34. D.C. Yeh, W.A. Sibley, I. Schneider, R.S. Afzal, I. Aggarwal, J. Appl. Phys., 69, 1648 (1990).

35. R.A. McFarlane, J. Opt. Soc. Am. B, 11, 871 (1994).

36. B.R. Reddy, P. Venkateswarlu, Appl. Phys. Lett., 64, 1327, (1993).

37. S. Tanabe, K. Hirao, N. Soga, J. Non-Cryst. Solids, 122, 79 (1990).

38. A.J. Silversmith, W. Lenth, R.M. Macfarlane, Appl. Phys. Lett., 51 (24), 1977 (1987).

39. T. Hebert, R. Wannemacher, W. Lenth, R.M. Macfarlane, Appl. Phys. Lett., 57, 1727 (1990).

40. J.S. Chivian, W.E. Case, D.D. Eden, Appl. Phys. Lett., 35 (2), 124 (1979).

41. X. Wu, J.p. Denis, G. Özen, P. Goldner, F. Pellé, J. Phys. Chem. Solids, 53 (6), 717 (1993).

42. M.P. Hehlen, G. Frei, H.U. Güdel, Phys. Rev. B, 50 (22), 16264 (1994).

43. T. Weber, W. Lüthy, H.P. Weber, Appl. Phys. B, 55, 144 (1992).

44. A.A. Kaminskii, Sov. Phys. Dokl., 27 (12), 1039 (1982).

45. Z. Pan, S.H. Morgan, A. Loper, V. King, B.H. Long, W.E. Collins, J. Appl. Phys., 77, 4688 (1995).

46. W. Lenth, R.M. Macfarlane, J. Lumin., 45, 346 (1990).

47. W. Lenth, A.J. Silversmith, R.M. Macfarlane, "Advances in Laser Science II", eds. A.C. Tam, J.L. Gole, W.C. Swalley, Am. Inst. of Phys., New York (1988).

48. L. Núñez, B. Herreros, R. Duchowicz, G. Lifante, J.O. Tocho, F. Cusso, J. Lumin., 60 & 61, 81 (1994).

49. F. Auzel, J. Lumin., 31 & 32, 759 (1984).

50. F. Tong, W.P. Risk, R.M. Macfarlane, W. Lenth, Electron. Lett., 25, 1389 (1989).

51. P. Xie, S.C. Rand, Opt. Lett., 15, 848 (1990).

52. S. Georgescu, V. Lupei, A. Lupei, V.I. Zhekov, T.M. Murina, M.I. Studenikin, Opt. Commun., 81 (3&4), 186, (1991).

53. S.A. Pollack, D.B. Chang, J. Appl. Phys., 64, 2885 (1988).

54. S.A. Pollack, D.B. Chang, R.A. McFarlane, H. Jenssen, J. Appl. Phys., 67, 648 (1990).

55. A. Silversmith, J. Lumin., 60 & 61, 636 (1994).

56. J. Nilsson, P. Blixt, B. Jaskorzynska, J. Babonas, J. Lightwave Technol., 13 (3), 341 (1995).

57. J.L. Sommerdijk, W.L. Wanmaker, J.G. Verriet, J. Lumin., 4, 404 (1971).

58. R.A. McFarlane, Appl. Phys. Lett., 54, 2301 (1989).

59. P. Xie, S.C. Rand, Opt. Lett., 17, 1198 (1992).

60. T. Kushida, M. Tamatani, J. Japan. Soc. Appl. Phys. (suppl.), 39, 241, (1969).

61. J.P. Van der Ziel, L.G. Van Uitert, W.H. Grodkiewicz, J. Appl. Phys., 41, 3308 (1970).

62. L.G. Van Uitert, H.J. Levinstein, W.H. Grodkiewicz, Mat. Res. Bull., 4, 381 (1969).

63. Y.M. Hua, Q. Li, Y.L. Chen, Y.X. Chen, Opt. Commun., 88, 441 (1992).

64. F.W. Ostermeyer, Jr. and L.G. Van Uitert, Phys. Rev. B, 1, 4208 (1970).

65. Th. Förster, Ann. Physik, 2, 55 (1948).

66. D.L. Dexter, J. Chem. Phys., 21, 836 (1953).

67. M. Inokuti, F. Hirayama, J. Chem. Phys., 43, 1978 (1965).

68. R. Orbach, "Optical Properties of Ions in Crystals", eds. H.M. Crosswhite, H.W. Moos, Interscience, New York, 445 (1967).

69. L.A. Riseberg, H.W. Moos, Phys. Rev., 174, 429 (1968).

70. T. Miyakawa, D.L. Dexter, Phys. Rev. B, 1, 2961 (1970).

71. H. Kuroda, S. Shionoya, T. Kushida, J. Phys. Soc. Jap., 33 (1), 125 (1972).

72. E. Reed, H.W. Moos, Phys. Rev. B, 8, 980 (1973).

73. J. Rubin, A. Brenier, R. Moncorge, C. Pedrini, J. Lumin., 36, 39 (1986).

74. C. Li, J.C. Souriau, R. Moncorgé, J. Phys IV, C7, 371 (1991).

75. V. Lupei, J. of Lumin., 48 & 49, 157 (1991).

76. R. Scheps, IEEE J. Quant. Elect., 31 (2), 309 (1995).

77. E.W.J.L. Oomen, P.M.T. Le Gall, A.M.A. van Dongen, J. Lumin., 46, 353 (1990).

78. X. Zou, A. Shikida, H. Yanagita, H. Toratani, J. Non-Cryst. Solids, 181, 100 (1995).

79. M. Bettinelli, G. Ingletto, J. Lumin., 43, 115 (1989).

80. R.K. Watts, H.J. Richter, Phys. Rev. B., 6, 1584 (1972).

81. R.K. Watts, in "Optical Properties of Ions in Solids", ed. B. Di Bartolo, Plenum, New York, 307 (1975).

82. M. Bettinelli, C.D. Flint, J. Phys. Cond. Matter, 3, 4433 (1991).

CHAPTER 5

5.1 CONCLUSIONS

Energy levels for the $4f^{11}$ configuration of Er^{3+} in YVO_4 were established from high resolution absorption and fluorescence spectra. Energy-level assignments were made using electric dipole transition selection rules for D_{2d} symmetry. From the measurements 59 energy levels were established. Crystal field parameters were determined by fitting 59 of the levels with an rms deviation of 6.8 cm^{-1}. These parameters were then used to obtain the remaining levels, yielding a complete energy level scheme for the $4f^{11}$ configuration of Er^{3+}.

The intensities of all the electric dipole transitions of Er^{3+} in YVO_4 have been measured and theoretically accounted for in terms of the three phenomenological parameters: $\Omega_2 = 13.45 \times 10^{-20}$ cm^2, $\Omega_4 = 2.23 \times 10^{-20}$ cm^2, and $\Omega_6 = 1.67 \times 10^{-20}$ cm^2, defined by the Judd-Ofelt theory. The high value of Ω_2 obtained indicates the existence of a strong covalent bond between Er and oxygen, while the values of Ω_4 and Ω_6 indicate that the YVO_4 is a hard crystal with a higher degree of disorder in comparison to other hosts. The Judd-Ofelt formalism was used to calculate the emission probabilities of transitions from the different states to the lower lying J manifolds and their corresponding branching ratios and radiative lifetimes.

Thermalization of the $^2H_{11/2}$ state from the $^4S_{3/2}$ state was studied and it was found that it may be analyzed using a simple two-level thermalization process. An energy gap of 641 cm^{-1} between the $^4S_{3/2}$ and $^2H_{11/2}$ states was calculated which is in excellent agreement with the value ($\Delta E = 644$ cm^{-1}) determined from the spectra.

A series of measurements on upconversion in Er^{3+}:YVO_4 were also described. We observed upconversion of red and near infrared radiation to green. The green emission corresponding to the $^2H_{11/2}$, $^4S_{3/2} \rightarrow {}^4I_{15/2}$ transitions was dominant, and increased with an increase in erbium concentration. This trend was valid up to a concentration of 2.5% Er^{3+}. The upconverted emission intensities decreased as the Er^{3+} concentration was increased to 10% and this was attributed to quenching and migration. The "pumping" power dependence of the upconversion output clearly illustrated the number of photons required for the process. Such power dependence studies in conjunction with the fluorescence dynamics studies, were used to establish the different pathways responsible for the population of the higher energy levels of Er^{3+}. Sequential absorption of photons, energy transfer, and cross-relaxation energy transfer processes were found to be responsible for such a phenomenon.

The luminescence decay profiles from the ${}^4S_{3/2}$ state of Er^{3+} in $Y_{1-x}Er_xVO_4$ (with x = 0.001, 0.01, 0.025, and 0.1) were measured over the temperature range 6-293K. For x = 0.01 and 0.025 both energy migration and cross-relaxation occur. For x = 0.1 the energy transfer from the donors to the nearest neighbour acceptors become dominant and the emission is strongly quenched. The decay profiles of the luminescence of the ${}^4S_{3/2}$ level of Er^{3+} (1.0%) obey the Inokuti-Hirayama model for energy transfer for an electric dipole - electric dipole interaction, in the absence of diffusion among the donors. The dipole-dipole coupling parameter was estimated to be 2.9×10^{-51} m^6s^{-1} and compared well to other well known systems.

5.2 FUTURE WORK

The results and conclusions from this thesis open many avenues for research. Experiments should be performed in order to determine the quantum efficiency of the fluorescing levels in YVO_4:Er^{3+} which is essential in the design and performance of an efficient laser system. In the case where there is no upconversion, this could be done if excited states were populated by either absorption from the ${}^4I_{15/2}$ ground state manifold or by nonradiative decay processes from higher excited states. However this is not the case in the $YVO_4:Er^{3+}$ system, where upconversion does exist giving rise to anti-Stokes emission, and hence the higher levels are populated via different intermediate levels other than the ground state. A solution to this problem, is to perform dual excitation beam fluorescence experiments. In such an experiment, an excitation frequency is used to populate the excited state, and a second laser would probe transitions from this state.

Assuming that laser action is achieved in such hosts, a new set of questions need to be answered, such as; the laser threshold, the laser pulse characteristics of the laser system to be built, and the excited-state dynamics which are at the origin of these results.

Experiments should also be performed to investigate the optical properties of co-doped systems (such as Er^{3+}-Yb^{3+}, Eu^{3+}-Tb^{3+}, and Er^{3+}-Ho^{3+}) which are in general very complex. Such studies involves the determination of the optimum concentrations of the dopants.

Computational techniques such as molecular dynamics and Monte Carlo, should be used to investigate the energy transfer processes.

IMAGE EVALUATION
TEST TARGET (QA-3)

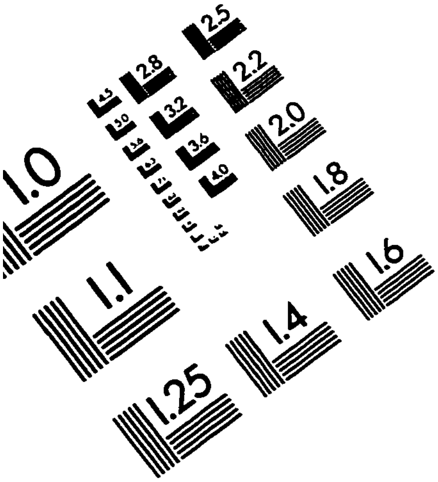

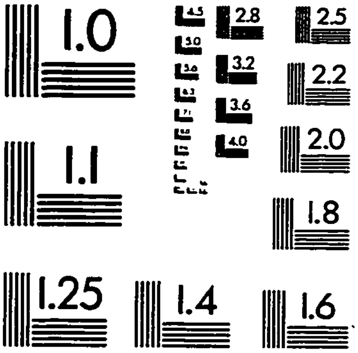

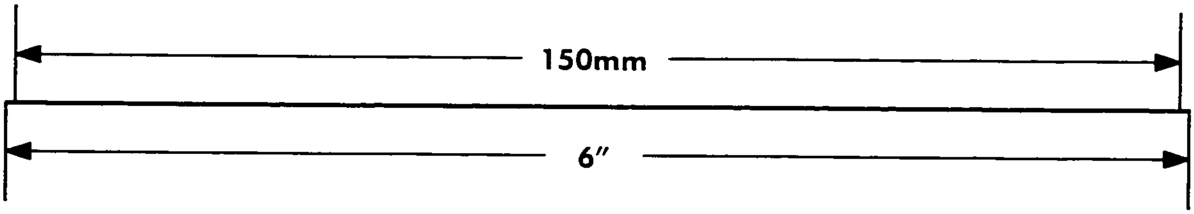

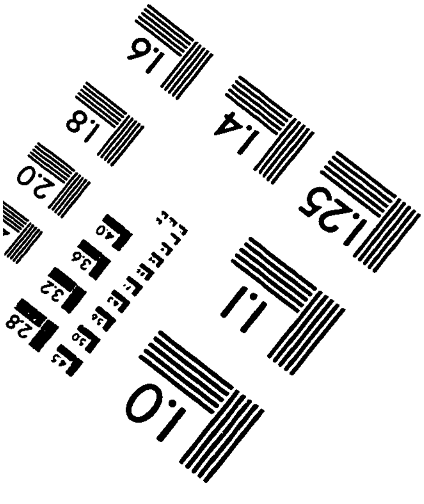

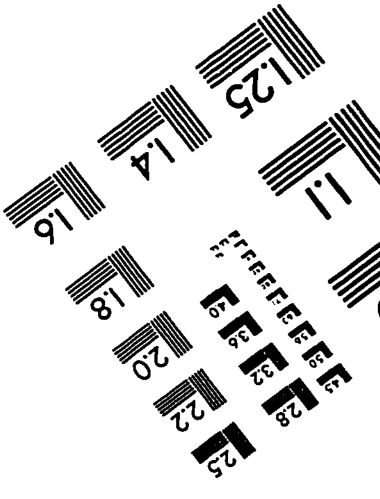

APPLIED IMAGE, Inc
1653 East Main Street
Rochester, NY 14609 USA
Phone: 716/482-0300
Fax: 716/288-5989